Master's thesis

NTNU
Norwegian University of Science and Technology
Faculty of Engineering
Department of Mechanical and Industrial Engineering

Ole Emil Herrmann
Alexander Norum Meløysund

Leveraging Surface Tension and Capillary Flow

Design Optimization for Exhaled Breath Condensate Transport in Inflammacheck Breathalyzers

Master's thesis in Mechanical Engineering
Supervisor: Chao Gao
June 2023

NTNU
Norwegian University of
Science and Technology

Ole Emil Herrmann
Alexander Norum Meløysund

Leveraging Surface Tension and Capillary Flow

Design Optimization for Exhaled Breath Condensate Transport in Inflammacheck Breathalyzers

Master's thesis in Mechanical Engineering
Supervisor: Chao Gao
June 2023

Norwegian University of Science and Technology
Faculty of Engineering
Department of Mechanical and Industrial Engineering

NTNU
Norwegian University of
Science and Technology

Abstract

In this master's thesis, the challenge of efficiently and exactly collecting and transporting exhaled breath condensate (EBC) in the sensor cartridge of the Inflammacheck® breathalyzer is studied. The Inflammacheck® breathalyzer is a device developed by Zimmer and Peacock for non-invasive monitoring of respiratory conditions through the analysis of EBC. In a preliminary study, an initial exploration of various forces and phenomena is performed to discern feasible mechanisms for the retention and release of liquid. Through this preliminary study, it becomes evident that understanding the balance between gravitational and surface tension forces in the sensor cartridge is pivotal, and the study converges to analyzing how geometric parameters and material properties influence these forces.

An 'Hourglass Concept' is conceived with this focus, utilizing capillary action within converging and diverging channels. Analytical calculations, numerical simulations, and practical experiments provide a foundational understanding of the interplay between the surface tension of the condensate, channel geometries, and channel surface properties. It is demonstrated that manipulating these variables imparts a degree of control over the equilibrium position of the liquid within the channel, which gives guiding principles for the design of systems harnessing capillary forces.

Additionally, the study identifies surface roughness as a substantial constraint in achieving ideal capillary flow. There is a deviation between theoretical predictions and experimental results, attributed mainly to surface roughness, emphasizing the necessity for judicious material selection and manufacturing methods, preferably aiming at smooth surfaces.

In summary, this thesis constitutes an initial exploration into balancing gravitational and surface tension forces for EBC retention and release in breathalyzers like the Inflammacheck®. The investigation lays the groundwork by presenting preliminary insights into the role of surface tension and geometric parameters within capillary flow while cautioning against the constraints posed by surface roughness. The findings call for further investigation and refinement in subsequent studies to increase practical applications.

Sammendrag

I denne masteroppgaven brukes en utforskende metode for å adressere utfordringen med å samle og transportere kondensert pust (EBC) effektivt i Inflammacheck® pust-analysatoren. Denne enheten, som er utviklet av Zimmer og Peacock, benyttes til noninvasiv overvåking av luftveisforhold gjennom analyse av EBC. I starten av oppgaven gjennomgås ulike krefter og fenomener for å finne hensiktsmessige mekanismer for oppbevaring og frigjøring av væske. Gjennom denne prosessen blir det tydelig at det er kritisk å forstå balansen mellom gravitasjon og overflatespenning, og oppgaven konsentrerer seg om hvordan geometriske parametere og materialeegenskaper påvirker disse kreftene.

Et "Timeglass-konsept" er skapt med dette fokuset, som drar nytte av kapillærkrefter i kanaler med både innsnevrende og utvidende geometri. Gjennom teoretiske modeller, numeriske simuleringer og praktiske forsøk, oppnås en grunnleggende forståelse av hvordan kontaktvinkler, kanalgeometri og kanalens overflateeegenskaper spiller sammen. Det blir demonstrert at ved å justere disse variablene kan man oppnå en viss kontroll over væskens posisjon i kanalen, noe som kan peke mot grunnleggende designprinsipper for utforming av systemer som utnytter kapillærkrefter.

Oppgaven identifiserer også overflateruhet som en betydelig hindring for ideell kapillærstrøm. Det er et tydelig avvik mellom teoretiske antakelser og de eksperimentelle resultatene, hovedsakelig på grunn av overflateruhet. Dette understreker viktigheten av å velge materialer of produksjonsmetoder med omhu, og at glatte overflater bør priotiteres.

Oppsummert representerer denne masteroppgaven en begynnelse for utforskning av balansen mellom gravitasjon og overflatespenning i forbindelse med oppsamling og frigjøring av EBC i puste-analysatorer som Inflammacheck®. Undersøkelsen danner et fundament ved å gi en første innsikt i hvordan overflatespenning og geometriske parametere spiller inn, samtidig som den påpeker begrensningene som overflateruhet medfører. Resultatene antyder at det er behov for mer omfattende undersøkelser og videreutvikling i fremtidige studier for å kunne anvende dette i praksis.

Contents

List of Figures

List of Tables

List of Abbreviations

EBC	Exhaled Breath Condensate
PMMA	Polymethyl methacrylate

List of Symbols

A	Area
d	Depth
F, F_{cap}	Capillary force
F_g	Gravity force
$\boldsymbol{F_{sv}}$	Volume force from surface tension
g	Gravity
h	Height
p	Pressure
R	Principal radius of surface curvature
r	Radius
$\boldsymbol{u}$	Velocity field
V	Volume
W	Width
W_a	Work of adhesion forces
W_{min}	Width at transition point of hourglass channel
x	Half of channel width
α, β	Converging/diverging channel slope angles
χ	Phase field mobility parameter
ϵ	Interface thickness parameter
γ	Level set reinitialization parameter
κ	Surface curvature
μ	Viscosity
μ_{ch}	Chemical potential
∇	Nabla operator
Φ	Level set/Phase field variable
φ	Cassie roughness factor
ρ	Density
σ	Surface tension
σ_{LG}	Surface tension liquid - gas
σ_{SG}	Surface tension solid - gas
σ_{SL}	Surface tension solid - liquid
θ	Contact angle
θ_a	Apparent contact angle
θ_{CS}	Cassie contact angle
θ_d	Contact angle for out-of-plane curvature in rectangular channels
θ_W	Contact angle for in-plane curvature in rectangular channels
θ_w	Wenzel contact angle
ξ	Wenzel roughness factor

1 Introduction

1.1 Background and Motivation

The non-invasive procedure is a term broadly used in the medical field [1, 2, 3]. It is a medical procedure that does not require inserting an instrument through the skin or into a body opening. The non-invasive technology of x-ray revolutionized the medical field more than 100 years ago [4], and today many non-invasive procedures play a vital role in modern medicine, as they offer safer, more comfortable, and cost-effective alternatives to invasive interventions. They are crucial for diagnostics, ongoing monitoring, and personalized treatment, improving patient outcomes and quality of life.

Respiratory diseases represent a significant global health concern and are responsible for 4 million annual deaths [5]. The most common respiratory diseases include asthma, chronic obstructive pulmonary disease, acute respiratory infections, and tuberculosis [6]. Continuous health monitoring and early detection can be crucial to reduce both the number of fatal outcomes of these diseases as well as healthcare costs.

Zimmer and Peacock Ltd is an engineering company located in Horten, Norway. They specialize in the design, production, and utilization of electrochemical biosensors, focusing on wearable biosensors, rapid testing in the food and beverage industry, and In-vitro Point-of-Care Diagnostics. The services they offer include both physical products and engineering consultancy. This master's thesis is completed in cooperation with Zimmer and Peacock.

Exhalation Technology™ has, in cooperation with Zimmer and Peacock, developed a device called Inflammacheck® [7, 8], which allows for non-invasive continuous monitoring of respiratory conditions. The device functions as a breathalyzer, where the breath vapor of patients is condensed, and subsequently, the exhaled breath condensate (EBC) is analyzed.

In private communications, Zimmer and Peacock have acknowledged that their device holds significant potential for future advancements. However, they have also raised concerns about the reliability of the mechanism responsible for delivering the exhaled breath condensate to the sensor for analysis. The device's effectiveness hinges on its ability to collect a sufficient and quantifiable amount of condensate and introduce it as quickly and reliably as possible. This is crucial to ensure both the validity of the diagnosis results and the ease of use for the patient. This challenge serves as the starting point for this thesis.

1.2 Research Objectives

The challenge of collecting and deploying EBC can be approached in several different ways. In order to choose the approach with the highest potential, a preliminary study comparing different approaches was conducted, and a set of criteria were evaluated. Based on a preliminary study of forces and phenomena, the focus was narrowed down to surface tension and capillary forces.

The main objective of this thesis is to understand how the equilibrium between gravitational forces and surface tension forces is affected by geometric parameters and material properties specifically wall adhesion and surface roughness. To achieve this, three distinct yet interconnected objectives are pursued.

1. Analytical models are developed to identify core parameters affecting the gravitational and surface tension forces in question. These models will serve as theoretical foundations for design evaluation and for validating experimental and numerical results.

2. Numerical simulation strategies for two-phase flow involving water and air are explored to optimize simulation parameters and boundary conditions with high accuracy compared to analytical solutions, within reasonable computation times.

3. Experiments are conducted to simulate real-world conditions. These experiments will be designed to be feasible within the study's constraints and focus on volumes of liquid similar to existing Inflammacheck® designs. Control over potential inaccuracies in geometric and material properties is crucial.

By synthesizing insights from analytical models, numerical simulations, and experiments, the study aims to build a robust understanding of the physics at play, thus fulfilling the main objective. Finally, new knowledge can be used to suggest a foundation for future Inflammacheck® channel designs and highlight the critical parameters that dictate performance.

1.3 Approach

The approach employed in this thesis is a methodical blend of exploratory research and focused investigation. The goal is to balance breadth and depth of understanding, starting with a deep dive into the workings of various underlying principles, followed by an extensive literature review. This in-depth examination of specific principles is essential for providing context and helping to effectively interpret and analyze the literature.

The next phase involves narrowing the focus to the most promising areas identified from the literature. This converging step is critical in allocating resources efficiently by concentrating on areas with the highest potential for innovation and practical applications.

During the in-depth investigation, the approach is iterative, involving repeated cycles of experimentation and analysis. Sometimes this leads to a dead-end or reveals incorrect assumptions, requiring revisiting previous steps. The iterative nature of this approach is particularly vital in the experimental and numerical chapters, allowing for quick adaptations and learning from each cycle.

A crucial aspect of the study involves deciding between isolating variables for a clearer understanding of their individual impacts and simulating real-world conditions for practical insights. Achieving a balance between these approaches is both vital and challenging.

The last challenge is coherently organizing the information and findings for this thesis. To address this, the thesis is structured to logically represent the steps taken, with content arranged thematically to reflect the systematic progression from broad research to focused investigation.

In summary, the approach is methodical and adaptive, combining broad research with focused, iterative investigation. This is designed to achieve an in-depth understanding while staying aligned with practical relevance and application.

1.4 Project Outline

This thesis starts with a preliminary study, detailing the workings of Inflammacheck® and exploring different strategies for the introduction of EBC. These methods are compared and assessed. Next, the paper presents an exploration of the history and important equations associated with surface tension, capillary action, and numerical two-phase flow. A unique approach for EBC collection and introduction, using surface tension forces and gravity, is then introduced, explained, and evaluated. The impact of various material and geometric factors on this approach is explored through a parametric study in the numerical study chapter, with the findings discussed and assessed. The validity of the simulation models is checked by comparing them with the analytical solutions for static problems. A physical experiment to validate the theoretical approach is described, conducted, and discussed. This is followed by a discussion comparing the numerical simulations and experiments with each other and the theoretical approach. The paper concludes with recommendations for further work and a final conclusion summarising the findings of the thesis.

2 Preliminary Study

To narrow the scope of this thesis, a preliminary study is conducted. First, the Inflammacheck® is introduced, and the major components and functions are explained. Subsequently, the essential design criteria are outlined, which are important for the performance of the sample collection and introduction mechanism, ensuring that the Inflammacheck® operates with high precision and reliability. Zimmer and Peacock's current design solution for the collection and introduction of EBC is then presented, showcasing both the advantages and faults of the design. Thereafter, various concepts are explored that could help in managing the retention and release of EBC by considering forces and phenomena. After evaluating these, one concept stands out as most promising and is chosen for detailed analysis in the rest of the study.

2.1 Inflammacheck®

In recent years, non-invasive diagnostics have risen in popularity across many medical fields [1, 2, 3]. Novel technologies, such as advances in sensors and machine learning, have increased the possibilities significantly. The Inflammacheck®, designed and produced by Exhalation Technology™ in cooperation with Zimmer and Peacock, represents this trend quite well. It is a device that employs electrochemical sensors combined with machine learning algorithms to diagnose respiratory diseases, using the same concepts as conventional breathalyzers. It gathers breath condensate and enables the measuring and logging of five different biomarkers [9]:

- Hydrogen peroxide H_2O_2
- Carbon dioxide CO_2
- Exhaled breath flow
- Exhaled breath temperature
- Exhaled breath relative humidity

The Inflammacheck® device can be split into three main components. The first is reusable and contains all parts that are not in direct contact with the patient's breath vapor. This includes, among other things, a polymeric chassis, electronics for powering and controlling the device, a user interface screen, sensors for measuring temperature, pressure, and humidity, as well as a Peltier element with a heat sink and a fan, used for breath condensation. The Peltier element is cooled down with a voltage and increases the condensation rate. The other two components are for one-time use and must be disposed of and replaced for every sample.

Figure 2.1: Inflammacheck®

The components designed for one-time use consist of the parts in direct contact with the patient's saliva, either in the form of spit or unfiltered exhaled breath vapor. The reasoning behind these parts being for one-time use naturally stems from the contamination risks they present. The first component for one-time use is a flow chamber that the patient breathes into, which directs the breath flow in the desired direction and contains particle filters to ensure that the patient's potentially contagious breath vapor does not spread through the air. The second one-time use component is the sensor cartridge which can be viewed in detail in figure 2.2.

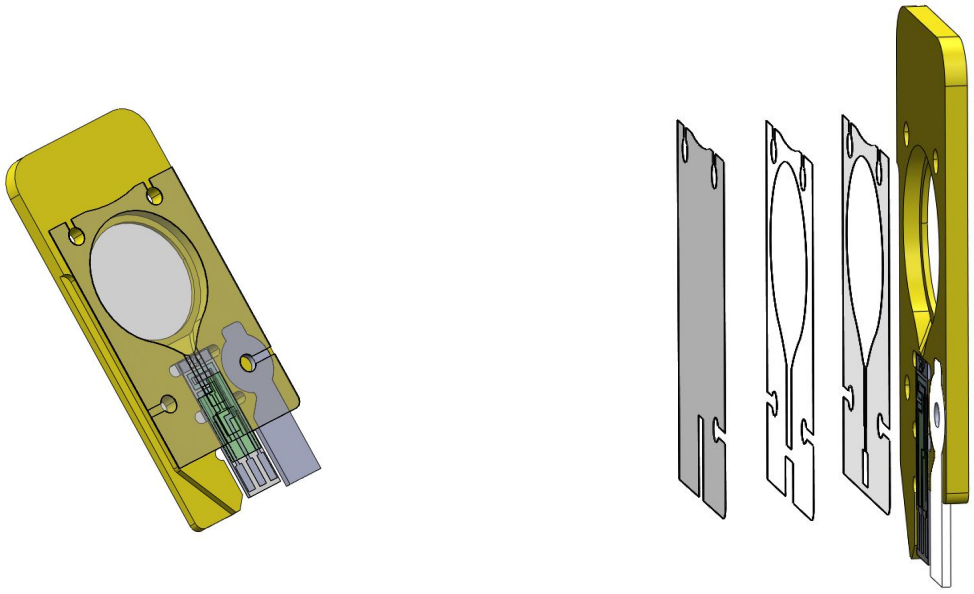

(a) Assembled view (b) Exploded view

Figure 2.2: CAD model of sensor cartridge

The sensor cartridge is the area of interest for this thesis. It is connected both to the reusable component of the device as well as to the flow chamber. The cartridge consists of several parts; a polymeric container, a biosensor, three layers of polymeric film with different surface properties, and an RFID chip. When the Inflammacheck® is used, exhaled breath vapor from the patient is directed onto the hydrophilic film of the cartridge, which is cooled by the Peltier element. The low temperature of the surface leads to vapor condensing, thus creating EBC. Due to the hydrophilic nature of the film, the EBC spreads out across the surface. Once the EBC reaches a sufficient mass, gravity pulls it toward the biosensor at the bottom of the cartridge. The biosensor requires 10 µL of EBC to conduct a consistent and valid measurement.

The biosensor is a so-called screen-printed electrode sensor. It consists of three main components; a working electrode, a counter electrode, and a reference electrode. When the EBC makes contact with the working electrode, the hydrogen peroxide (H_2O_2) in the EBC undergoes a reduction reaction, releasing electrons. These electrons create a current from the working electrode to the counter electrode. Therefore, measuring the potential difference to the reference electrodes provides information on how much H_2O_2 the EBC contains.

2.2 Design Criteria

Ensuring the biosensor's consistency and reliability necessitates the controlled introduction of the EBC sample onto the working electrode. A comprehensive set of criteria is developed for effective evaluation and comparison of different concepts. These criteria and brief explanations of their inclusion are presented from most significant to least significant for this thesis. Afterward, the subcriteria that might be considered will be listed.

1. **High Precision** For the biosensor to produce consistent results, the EBC sample introduction must be as precise as possible. It is vital that the whole working electrode has contact with the sample while the sensor measurements are registered. This can only be ensured if the introduction happens consistently every time, with the right volume of condensate, to ensure a consistent salt concentration. To achieve consistent measurement, the introduction onto the sensor should transpire so quickly that the electrode is not only partially in contact with the sample for a significant amount of measurement time steps.

2. **High robustness** Since the Inflammaceck® is a hand-held device held by the patient, it is not guaranteed that the cartridge is positioned correctly (i.e., vertically) at all times. The sample introduction mechanism has to be sufficiently robust to ensure consistent measurements despite these outside variables. It should also be resilient to variations in breadth pressure, humidity, and temperature.

3. **Low collection time** For patients with respiratory diseases, the lung capacity is typically reduced by a significant amount. Due to this, breathing into a breathalyzer for an extended amount of time can be pretty exhausting for them. In order to ease the effort for the patient as much as possible, it is therefore essential that the testing time is not too long. Ideally, the patient should only have to breathe into the device for a minute or less. To achieve this, the condensing process has to be optimized, and the sample should be introduced to the biosensor as soon as the minimum amount of EBC needed to cover the working electrode is collected.

4. **Low theoretical and Experimental Complexity (R&D)** The device should be possible to develop within the scope and budget of this thesis. A device should use a concept that is possible to analyze analytically, simulate numerically, and perform experiments with prototypes.

5. **Low manufacturing costs and Scalability of production** Due to the cartridge being designed for one-time use, the introduction mechanism should be designed in a way that is well-suited for mass production. This requires the design to be simplified as much as possible to keep production costs low. Other expenses linked to quality control, transport, environmental impact, storage, and longevity should also be as low as possible.

6. **Flexibility** The design should be compatible with a range of biosensors measuring different biomarkers. This may require making minor adjustments in the geometry

of the sensor cartridge. To be able to make these adjustments, a theoretical understanding of how different parameters impact the sample introduction mechanism is necessary.

7. **Low health risks** The design should comply with relevant health regulations to ensure the health of the administrators and patients. Any EBC should be contained within the one-time and cleanable parts to reduce the risk of infections.

Subcriteria that might be considered are listed below.

1. High precision
   (a) Low variance volume of fluid introduced
   (b) Appropriate mean volume of fluid introduced
   (c) Sudden sample introduction - Mean and variance of sample rush time
2. High robustness
   (a) Robust to variables (angle, breath pressure, humidity, temperature)
   (b) Fail-safe mechanisms for incorrect usage
3. Low collection time
4. Low theoretical and Experimental Complexity
   (a) Low theory complexity
      i. Based on well-known theory and concepts
      ii. Analytical solution
      iii. Limited physical phenomena
   (b) Low simulation complexity
      i. Well-known concepts and solvers
      ii. Low simulation time
      iii. Can be simplified to 2D and have symmetries
      iv. High convergence rate
   (c) Low experiment complexity
      i. Parameters are measurable
      ii. Easy to isolate known factors
      iii. Low prototype complexity
5. Low manufacturing cost and Scalability of production
   (a) Low mass production cost (Estimated cost per sample at scale)
   (b) Low cost of the reusable part
   (c) Scaleability of production
   (d) Easy quality control
   (e) Low environmental impact
   (f) Easily stored and transported (no required temperature, cleanliness standard, small size)
   (g) No/little requirements for external energy source
   (h) High longevity (Expiration time)
6. Flexible design

(a) Easily inserted
(b) Ease of compatibility
(c) Easy change of individual dimensions

7. Health
   (a) Compliance with regulatory rules
   (b) Hygiene and infection control (Closed loop, leakproof)

2.3 Rush Mechanism

In order to meet the requirements for the EBC sample introduction mechanism that are mentioned above, engineers at Zimmer and Peacock have investigated a number of different approaches. Among the concepts that are tested the most, and that is in fact utilized today, is the so-called rush mechanism. A sensor cartridge where this concept is applied can be viewed in figure 2.3.

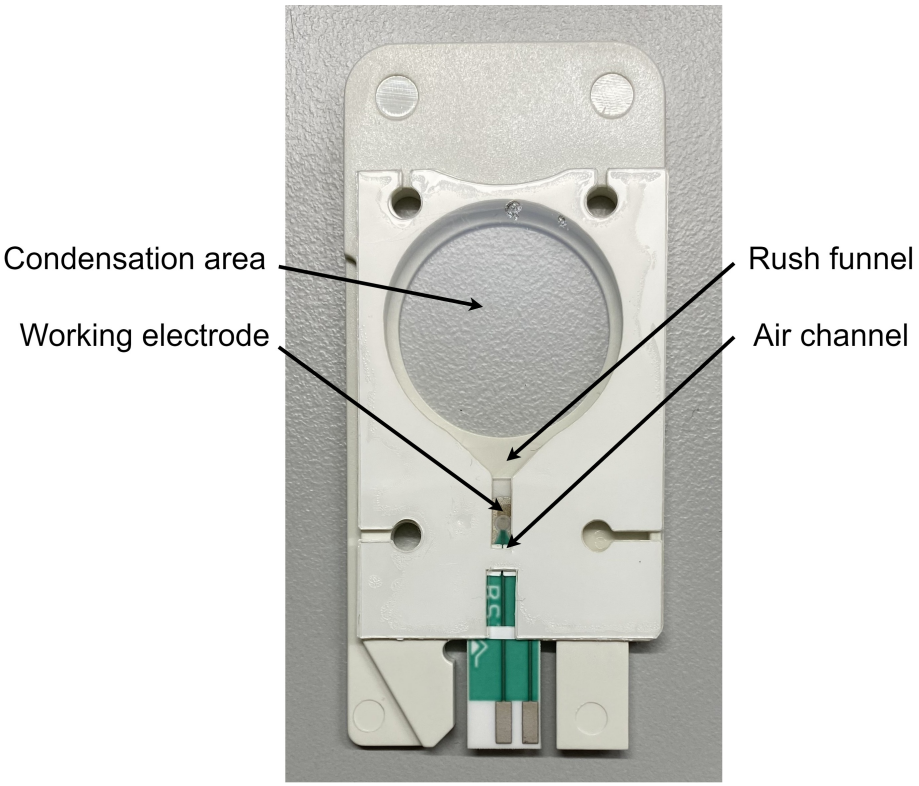

Figure 2.3: Sensor cartridge with implemented rush mechanism

The rush mechanism design includes a funnel that is positioned directly beneath the large circular condensation area. Under the funnel, there is a vertical flow channel with a narrow opening at its bottom. Inside the channel, the working electrode is positioned, as well as a spot of salt, which is placed directly above the electrode. When in use, the EBC is collected in the funnel, moving downwards until it reaches the vertical channel. This process is hereafter referred to as the collector. In the funnel, the intention is that the EBC reaches a force equilibrium between its own weight and the pressure from the air trapped in the channel beneath. Once a critical volume of EBC is collected, the mass

of the EBC is able to press the air through the narrow opening at the bottom. The mechanism for retaining the liquid and releasing it at a specific volume of condensate will subsequently be referred to as the volume-control valve. After the release, the liquid rushes down towards the salt spot and dissolves it, before it reaches the working electrode. The working procedure is presented in four steps in figure 2.4.

The performance of the current rush design can be evaluated in terms of the criteria required for consistent results presented in section 2.2. The design achieves both a quick sample introduction mechanism, as well as a relatively low amount of EBC needed in order to complete the measurement. This makes it score quite high in terms of overall speed and low collection time. Regarding the criterion of ease of production, the rush design also has clear strengths, due to exhibiting a relatively simple geometry.

Although the rush design has its clear strengths and advantages, it also has its areas where improvement is required. For instance, Zimmer and Peacock have privately reported considerable reliability issues. Both instances where the EBC has been introduced to the sensor prematurely and did not cover the whole electrode, as well as instances where far too much EBC was collected before introduction have occurred. The fact that the design, according to Zimmer and Peacock, is a product of large amounts of trial and error represents another challenge. While trial and error have proved to be an effective method in order to obtain a working concept in a short period of time, it has resulted in an incomplete analytical understanding of the physics of the mechanism.

(a) Dry, un-used cartridge

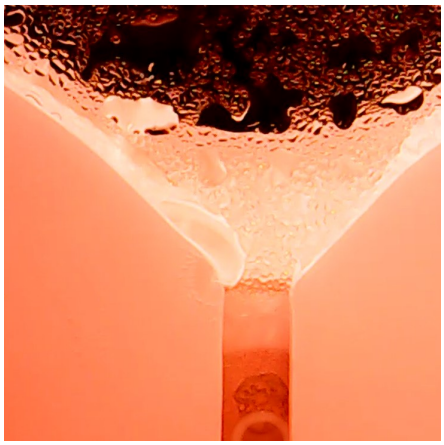

(b) Wetted hydrophilic film

(c) EBC is stationary due to force equilibrium

(d) EBC is introduced to biosensor

Figure 2.4: Rush mechanism presented in four steps

2.4 Exploring Principles and Concepts

2.4.1 Forces and phenomena

In exploring potential new concepts for sample introduction, it was identified that the transport of EBC from the Peltier element to the sensor needs acting forces. The exploration encompasses an array of forces and principles, such as gravity, electromagnetism, pressure differentials, surface tension, and centripetal forces. A successful concept would likely employ a combination of these forces.

Gravitational force is ubiquitous and affects all designs. A well-crafted design should leverage gravity. However, to ensure device robustness, it should not be overly dependent on gravitational forces, especially as the device orientation may change during use. Gravity will manifest itself through hydrostatic pressure. When considering device robustness as a design criterion, the device must maintain functionality with a wide range of physical orientations.

Pressure, which is inherent in the respiratory process, is a critical force to be considered

in the design of the device. There are several sources of pressure differences that can be exploited in this context, including breathing, pre-stored sources, and mechanical pumps.

The static pressure generated through breathing depends on the patient and the lung volume involved in the breathing cycle. For adolescents, the maximum static pressure is approximately 100 cmH2O, or 10 kPa [10]. Notably, this pressure exhibits an approximately linear relationship with the volume of air breathed in or out [11]. However, the static pressure can vary widely among individuals, especially those with respiratory diseases.

Since respiratory diseases might affect an individual's ability to generate sufficient static pressure, it is imperative to understand these variations. To ensure the reliability and usability of the device across a diverse population, a comprehensive literature review and consultation with medical professionals specializing in respiratory health are essential.

To potentially compensate for the reduced ability to generate static pressure, especially in patients with respiratory diseases, the device can employ the Venturi effect. This principle utilizes the velocity of exhaled or inhaled air to create a pressure difference, as depicted in figure 2.5.

In employing the Venturi effect, the design could include a constricted passage within the flow channel, causing the velocity of the exhaled air to increase and the pressure to decrease as it passes through the constriction. This pressure difference can be harnessed to drive the transport of EBC.

Additionally, the device can integrate pre-stored pressure sources or mechanical pumps as supplementary mechanisms to generate pressure differences. Pre-stored pressure sources, such as springs or pressurized reservoirs, can ensure a constant driving force for EBC transport.

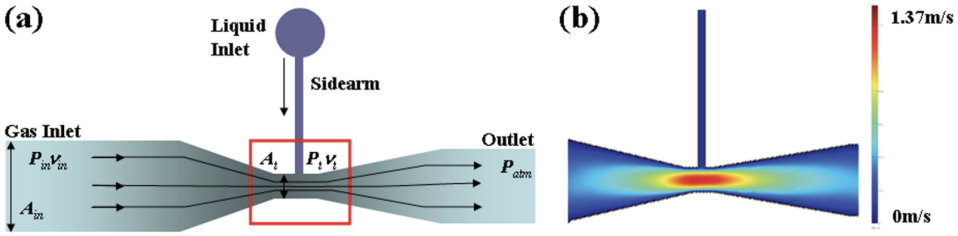

Figure 2.5: Illustration of the Venturi effect. When the channel narrows, the fluid accelerates, and the higher velocity reduces the pressure

Source: Hettiarachchi and Lee [11]

Pumps are widely used in microfluidics and would allow control of pressure and, therefore also the movement of the fluid. Among the various types, Elveflow provides peristaltic pumps, which utilize recurring tube compression, and syringe pumps, which rely on piston movements for fluid displacement. Bartels Mikrotechnik offers piezoelectric diaphragm pumps [12], [13]. There are also compact variants, such as the piezo disc pump, which employs rapid piezoelectric disc deformation and check valves as depicted in figure 2.6.

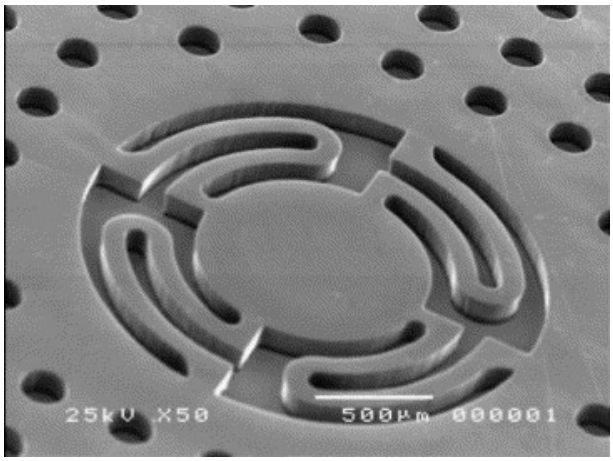

Figure 2.6: Check valve proposed for piezo disc pump

Source: Nguyen and Truong [14]

When considering pumps for integration into the device, evaluating their robustness is crucial, as pumps introduce mechanical components that may result in additional failure modes. Piezoelectric diaphragm pumps, with fewer moving parts, might be more robust compared to peristaltic pumps. Precision is another critical aspect; syringe pumps, for example, usually offer high precision but need consideration for calibration and maintenance. Cost and size are also critical factors; the selection should favor compact and cost-effective pumps, especially for portable applications. Additionally, it's essential to choose pumps with low power requirements to ensure the longevity of the device's battery life.

Limited examples of microfluidic systems utilizing electromagnetic forces are available, but the most promising principle is electroosmotic flow [15, 16]. Electroosmotic flow propels an electrolyte using an electric field, as illustrated in Figure 2.7. However, uncertainties remain regarding how EBC would behave under such an electric field and whether it would alter the concentration of desired molecules and salts. Implementing electroosmotic flow requires a voltage source, but fortunately, Inflammacheck® possesses a low-voltage network for its electronics. Takamura et al. [17] demonstrated an electroosmosis pump that achieves 800 Pa static pressure and a flow of 415 nL/min at 10 V, but to transport 10 µL a more powerful pump would be required.

At the microscale, with droplets under 1 mm, surface tension becomes significantly impactful, especially concerning hydrophilic (water-attracting) and hydrophobic (water-repelling) surfaces. Surface tension becomes even more dominant in thin channels, a phenomenon harnessed in microfluidics through the use of capillary "pumps" and "valves" as shown in Figures 2.8.

Surface tension is also exploited to enhance condensation. The conventional film-wise condensation method often employs hydrophilic surfaces to reduce the energy required for condensation, as the interface between water and such surfaces has higher bonding energy [20]. Though effective initially, as the water eventually forms a film over the cold material, it insulates it from the cold, causing condensation solely on the water's surface.

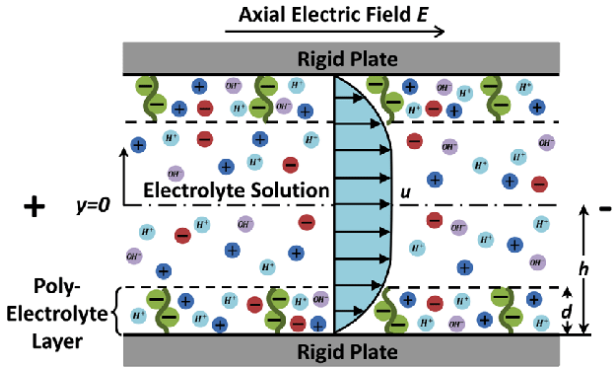

Figure 2.7: Illustration of electroosmotic flow

Source: Chen and Das [18]

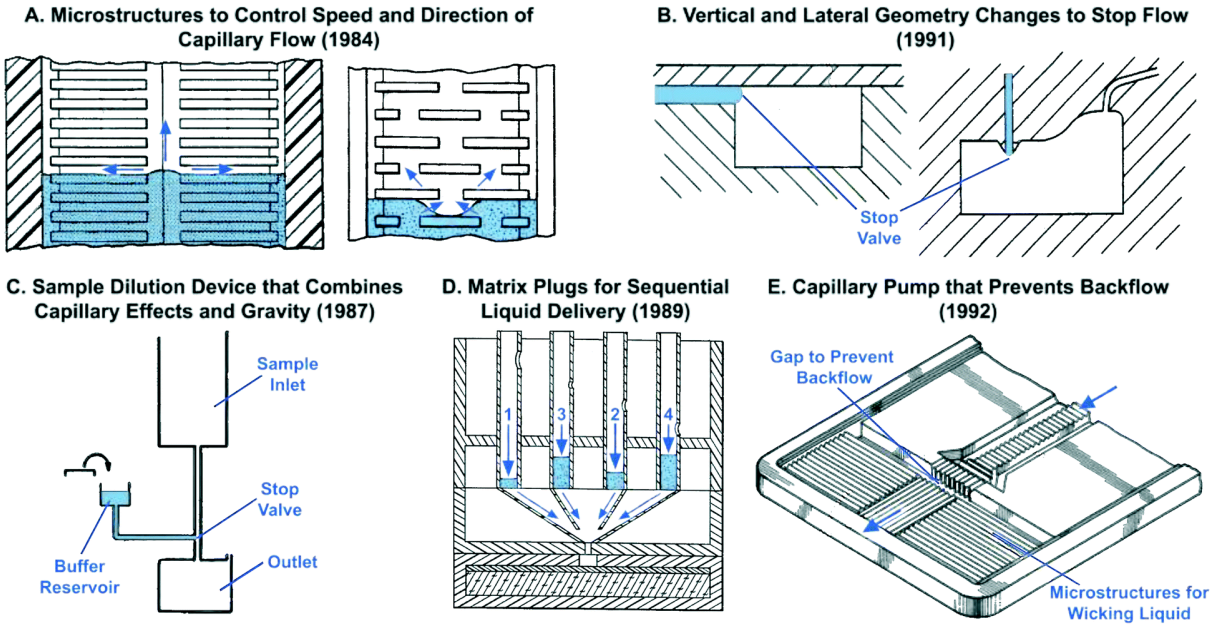

Figure 2.8: Utilization of surface tension forces and capillary effects

Source: Olanrewaju et al. [19]

This is the technique currently utilized by Zimmer and Peacock.

Alternatively, dropwise condensation on hydrophobic surfaces can yield substantially higher heat transfer coefficients - up to 5-7 times higher compared to film-wise condensation [21]. Even though hydrophobic surfaces require more energy for condensation, the droplets formed eventually fall due to gravity when they reach a specific size. This leaves portions of the surface free of water, allowing new droplets to form continuously with direct contact with the cold surface. Figure 2.9 illustrates a tube where film-wise condensation occurs at the bottom and dropwise condensation occurs at the top.

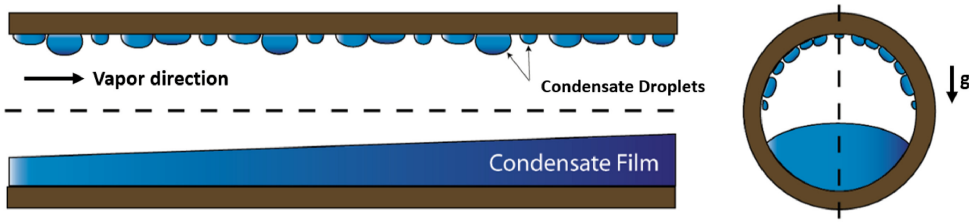

Figure 2.9: Illustration of dropwise and filmwise condensation

Source: El Fil et al. [21]

However, employing hydrophobic surfaces typically requires the application of a coating that can degrade over time. Fil et al. [21] estimate that such coatings can last approximately 100 hours to over 4 years. Hydrophilic and hydrophobic surfaces can also be produced with specific microstructure geometries [22]. Ems and Ndao [23] show that making an inherently hydrophilic material like silicon hydrophobic is possible just by adding microstructures.

Electrowetting, a technique involving the application of voltage to hydrophobic surfaces to increase their bonding energy, is a viable alternative for controlling fluid behavior on surfaces. As depicted in figure 2.10, this process can effectively change a hydrophobic surface to hydrophilic, and through precise patterning of voltage application, can facilitate the high-precision transport of droplets, as demonstrated by Grassin et al. [24]. The disadvantage of electrowetting is the requirement of electrical components and control systems, which must be integrated with one-time-use parts.

Controlled vibration of surfaces is a method used to manipulate the interaction between water droplets and surfaces, which works by reducing the bond energy of water. As shown in figure 2.11, vibrating the surface expedites droplet shedding, freeing the surface for further condensation. Moradi et al. [25] demonstrated the efficacy of this method by achieving a 120% increase in droplet shedding events and a 15% boost in condensation, utilizing a DC motor to apply a cyclical variable frequency peaking at 132 Hz on a hydrophobic surface. Moreover, Oh et al. [26] reported an eightfold increase in droplet departure speeds using a dielectric elastomer actuator for vibrations. Alternative actuation methods, such as piezoelectric actuators or mechanical pendulums, could provide a more cost-effective and compact solution for implementing controlled vibration in microfluidic applications. However, implementing controlled vibration also brings challenges, such as mechanical fatigue and the need for fine-tuning to achieve the desired

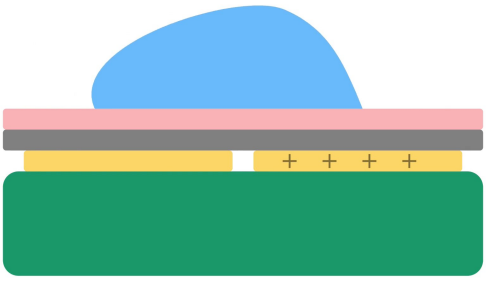

Figure 2.10: Illustration of electrowetting. The pink layer is hydrophobic; the grey layer is a dielectric film, the yellow layer is electrodes, and the green block is a printed circuit board (PCB). The PCB controls the charging of the electrodes to attract the dielectric water at a specific area.

Source: Grassin [24]

droplet behavior, which can add complexity and costs to the system.

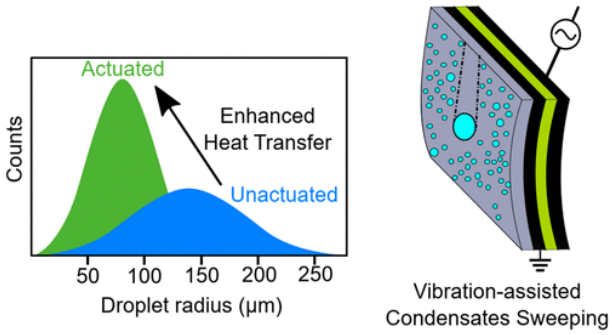

Figure 2.11: Concept of vibration under dropwise condensation

Source: Oh et al. [26]

Utilizing shape-morphing kirigami/origami structures, as depicted in figure 2.12, offers a novel approach for fluid manipulation in microfluidic applications. Kirigami structures have the unique property of altering their geometry in response to applied tension [27]. This characteristic can be leveraged to modulate surface wettability, reconfigure capillary channels, or facilitate the merging of droplets. While the field of kirigami is relatively nascent, and there is a lack of literature on the integration of kirigami structures in microfluidic fluid transport, the inherent flexibility and adaptability of these structures suggest a promising potential for innovative applications in fluid management as the field evolves.

Centrifugal force, which arises from rotating a device, can be harnessed for fluid manipulation in microfluidics, as illustrated in figure 2.13. This force propels the liquid outward and is employed in "lab-on-a-disc" systems for separation, mixing, and fluid transport. Centrifugal microfluidics is well-suited for handling small liquid volumes, with benefits including fast processing, reduced cross-contamination, and parallel analyses. However, ensuring mechanical stability and precise control of rotational speeds is critical for the reliability of such systems.

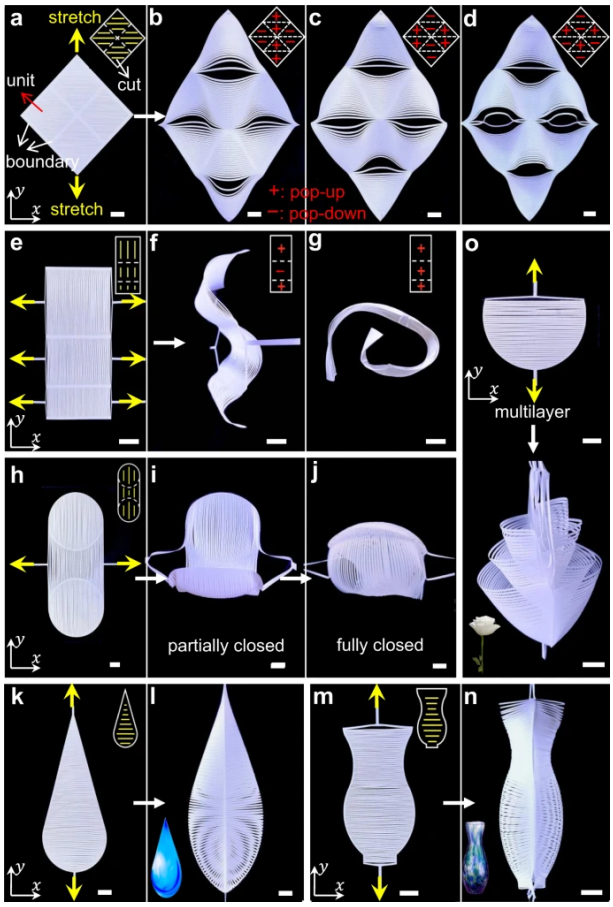

Figure 2.12: Ribbon kirigami shapes. The kirigami structures change topology under a load.

Source: Hong [27]

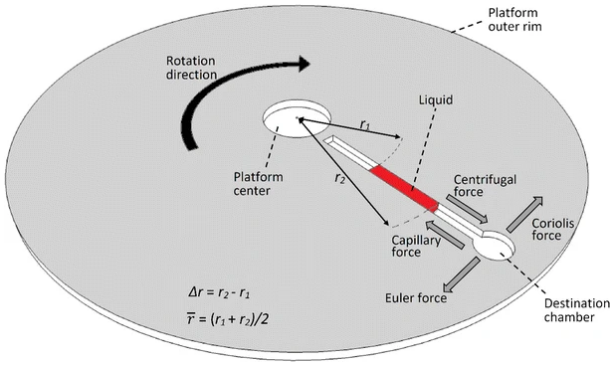

Figure 2.13: Lab-on-a-disc concept using centrifugal force to transport liquid

Source: Al Faqheri et al. [28]

2.4.2 Concepts and Evaluation

Identifying the optimal concept for controlling sample introduction entails examining two fundamental stages: the collector and the volume-control valve. The collector collects the EBC from the Peltier element into a single concentrated area. The collector in the rush mechanism has a hydrophilic film that utilizes gravity to move droplets and a funnel shape to concentrate the EBC. The second stage is the volume-control valve which holds the EBC until a specific volume is reached.

1. Collector
Evaluating the collection and volume control stages requires careful consideration of the design criteria outlined in section 2.2. The collector's efficiency primarily influences the collection time, while the volume-control valve mechanism determines the precision of the sample volume delivered to the sensor. Since precision and robustness are the critical criteria, this preliminary study focuses on examining and assessing various concepts for the volume-control valve, utilizing the forces discussed earlier. Importantly, these concepts are not rigid and can be combined to enhance performance. Additionally, it's vital to understand that the research and development (R&D) assessment is based on the capabilities of the current study, and feasibility may differ for researchers with different expertise.

2. Capillary balance
The second concept entails the development of a capillary force balance system, where the liquid is held at specified volumes but cannot exceed a certain threshold. Essentially, this system would function akin to the rush mechanism. However, through a more profound understanding and optimization of the geometry involved, the system can be developed to achieve higher precision and reliability. The capillary force balance system has several advantages, including simplicity and passiveness. Additionally, it is conducive to calculations and simulations, which can facilitate optimization. Interestingly, this concept might not necessitate the inclusion of hydrophobic or hydrophilic surfaces, as capillary forces can still play a significant role even with minimal wettability.

3. Hydrophobic barrier
The third concept is incorporating a hydrophobic barrier the fluid must surpass, assisted by either gravity or capillary forces. In this setup, the hydrophobic barrier serves as a gatekeeper, regulating fluid flow. However, it might necessitate carefully calibrating the forces at play to ensure the barrier can be reliably overcome.

4. Electrowetting
The fourth concept is utilizing electrowetting. Applying an electric field to a surface can modulate the wettability. This phenomenon can be leveraged to control fluid flow, like the capillary force balance or the hydrophobic barrier. What sets electrowetting apart is its capacity for greater complexity and fine-tuned control. By adjusting the applied voltage, it is possible to achieve precise control over the fluid's movement and interaction with surfaces. However, this increased complexity can also be viewed as a double-edged sword, as it might introduce additional challenges in terms of calibration and reliability.

5. Reservoir
Zimmer and Peacock have researched a concept involving a reservoir that gradually fills up from beneath the sensor as the liquid condenses, causing the water level to rise until it envelops the sensor. A challenge with this concept is that the sensor is exposed to the EBC gradually, and this has the potential to cause inconsistent measurement.

6. Mechanical Valve
Another concept involves utilizing pressure to actuate a mechanical valve. This concept is well-established on larger scales, but miniaturizing it for microfluidic applications presents significant challenges. Manufacturing a mechanical valve with the necessary precision and reliability at a small scale may require advanced fabrication techniques and materials.

7. Active Pump
As mentioned before, microfluidics pumps are well known for several off-the-shelf solutions. Moreover, they require an external control system and power source, which can complicate the setup and introduce additional potential sources of error.

8. Timed release and 9. Manual release
Lastly, timed and manual release methods offer simpler alternatives but are less fail-safe and consistent. In a timed release system, the EBC would be automatically released after the patient has breathed into the device for a specified duration. Conversely, the manual release entails an administrator releasing the EBC through a triggering mechanism, such as a button. These methods can be combined with the previously mentioned concepts but are more straightforward as they do not necessitate sensors or automatic triggering mechanisms.

Table 2.1 summarizes the evaluation of crucial design criteria for different volume-control valve concepts.

Table 2.1: Evaluation of different concepts based on the aforementioned design criteria in section 2.2. "+" and "++" signify a potential improvement, while "-" and "–" signify challenges or deterioration regarding the design criteria.

Concepts	Precision	Robustness	Time	R&D	Manufacturing
1. Collector			++	-	-
2. Capillary balance	++	++		++	++
3. Hydrophobic barrier	-			-	-
4. Electrowetting	++	-	+	- -	-
5. Reservoir	-	+	- -	++	++
6. Mechanical valve	+	-	-	-	-
7. Active pump	++	+	+	- -	- -
8. Timed release	- -	- -	-		-
9. Manual release	-	-	-	+	

In conclusion, within the context of this thesis, the capillary force balance emerges as the most promising concept owing to its inherent simplicity, which renders research and

development and manufacturing more feasible. Additionally, the fine-tuning of the capillary structures holds the potential for attaining both the precision and robustness sought in the design criteria, making it a compelling choice for further exploration.

3 Theory

This chapter features the theoretical foundation utilized throughout the thesis. First, the theory of surface tension is presented in-depth, introducing droplet physics, hydrophilicity, and capillary action. Subsequently, two-phase flow simulation theory is disclosed, including the mathematical foundation for the level set, as well as the phase field method.

3.1 Surface Tension Theory

Surface tension is defined as the cohesive force that acts at the surface of a liquid, causing it to behave like a stretched elastic sheet [29]. This force allows small insects to walk on water and gives droplets their spherical shape [30]. The surface tension forces will always motivate a given volume of liquid to take on a shape that minimizes its surface area. For a volume of liquid surrounded by air and where no other forces are applied, the volume geometry that minimizes the surface area is a sphere. Surface tension, σ_{LG}, has the unit [N/m].

3.1.1 Sessile droplet physics

On the other hand, if a volume of liquid is in contact with a solid surface in addition to its shared surface with air, the geometry of the volume becomes a product of both the cohesive surface tension forces and inter-molecular adhesive energy between the liquid and the solid surface. In other words, the geometry of the volume is a result of the interfacial energies per area σ_{ij} between liquid-gas (σ_{LG}), solid-liquid (σ_{SL}), and solid-gas (σ_{SG}), in addition to external forces, like gravity. Dupré's equation relates the adhesion energy W_a between the liquid and the solid surface and the characteristic surface energies [31]:

$$W_a = \sigma_{SG} + \sigma_{LG} - \sigma_{SL} \tag{3.1}$$

Combined with Young's equation

$$\cos\theta = \frac{\sigma_{SG} - \sigma_{SL}}{\sigma_{LG}}, \tag{3.2}$$

θ represents the contact angle between the solid surface and the tangent of the liquid-gas surface at the boundary where all three phases meet, as shown in figure 3.1, the Young-Dupré equation can be derived:

$$\cos\theta = \frac{W_a}{\sigma_{LG}} - 1 \tag{3.3}$$

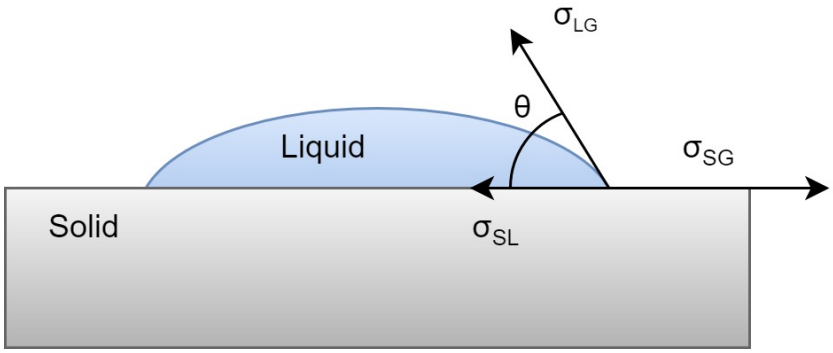

Figure 3.1: Schematic of interfacial energies acting on sessile droplet

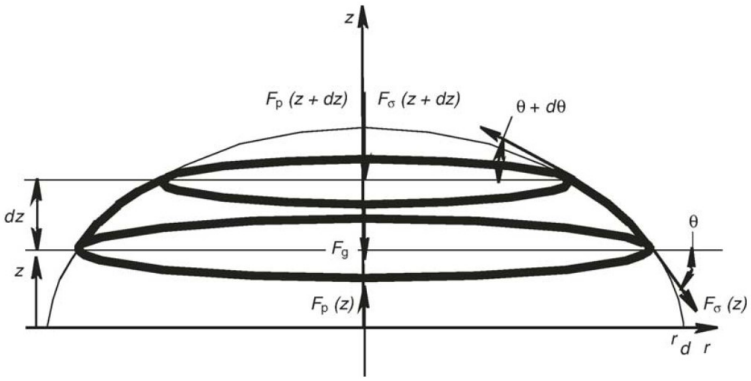

Figure 3.2: Schematic of axisymmetric sessile droplet

Source: Vafei and Podowski [32]

As mentioned, the surface tension seeks to minimize the surface area of the air, leading to a convex shape for a sessile droplet. Due to this, the surface tension increases the pressure inside the droplet. Bashforth and Adams [33] have developed a theoretical approach for determining the curvature of an axisymmetric droplet subjected to gravitational forces, given experimentally determined boundary conditions. Vafaei and Podowski [32] show how an equation that describes the curvature of an axisymmetric droplet can be derived from the force equilibrium in the z-direction in cylindrical coordinates.

$$\sum F_z = 0 = -dF_g(z) - F_p(z+dz) + F_p(z) - F_\sigma(z) sin(\theta) + F_\sigma(z+dz) sin(\theta+d\theta) - p_g 2\pi r dr \tag{3.4}$$

Here, $dF_g(z)$ is the incremental gravity force, $F_p(z)$ the pressure force, and $F_\sigma(z)$ the surface tension force onto a slice of the droplet between z and $z + dz$. p_g is the atmospheric pressure. p_0 is the pressure at the top of the droplet.

$$dF_g(z) = \rho g \pi r^2(z) \tag{3.5}$$

$$F_p(z) = \rho g z \pi r^2(z) \tag{3.6}$$

$$F_\sigma = \sigma_{LG} 2\pi r(z) \tag{3.7}$$

$$p_g = \rho_g g z + p_0 \tag{3.8}$$

Equation (3.4) can be rearranged to obtain the Young-Laplace equation in differential form as shown in appendix A.1.

$$p_0 + \rho g(z(0) - z(r)) = -\sigma_{LG} \left(\frac{\frac{dz}{dr}}{r\sqrt{1 + (\frac{dz}{dr})^2}} + \frac{\frac{d^2z}{dr^2}}{\left[1 + (\frac{dz}{dr})^2\right]^{\frac{3}{2}}} \right). \tag{3.9}$$

ρ and g are the density and gravity. This non-linear second-order differential equation for the shape of a droplet can be solved using a suitable numerical algorithm, for example, the fourth-order Runge-Kutta method. To obtain a unique solution, three boundary conditions must be given. These are listed in equations (3.10)-(3.12).

$$z'(0) = 0 \tag{3.10}$$

$$z(r_{droplet}) = 0 \tag{3.11}$$

$$z'(r_{droplet}) = -\tan\theta \tag{3.12}$$

Here, $z'(r)$ is the derivative of z with respect to r, $\frac{dz(r)}{dr}$. The circumferential radius of the droplet $r_{droplet}$ (r_d in figure 3.2) and the contact angle θ can be measured experimentally. The Young-Laplace equation can be simplified to equation (3.13) [34].

$$\Delta p = -\sigma_{LG} \left(\frac{1}{R_1} + \frac{1}{R_2} \right) \tag{3.13}$$

R_1 and R_2 represent the principal radii for the curvature of any given boundary between liquid and gas. The equation is true for every single point of the curvature, and the curvature will change depending on the pressure. If there is no gravity, Δp will be constant,

and the curvature will be the same for the whole droplet. In the case of the axisymmetric droplet, there is only one principal radius (i.e., $R_1 = R_2$). Thus, the Young-Laplace equation can be further simplified to

$$\Delta p = -\frac{2\sigma_{LG}}{R}. \tag{3.14}$$

The combination of the principal radii is called mean curvature and is denoted by κ or sometimes H. It can also be defined from the unit normal vector $\hat{\boldsymbol{n}}$ of the surface [35]. This version of the Young-Laplace equation is exact for any 3D curvature with an arbitrary shape.

$$\Delta p = -\sigma_{LG}\left(\frac{1}{R_1} + \frac{1}{R_2}\right) = -2\sigma_{LG}\kappa = -2\sigma_{LG}\nabla \cdot \hat{\boldsymbol{n}} \tag{3.15}$$

3.1.2 Hydrophilic and hydrophobic surfaces

All materials differ in how strong their adhesion forces to liquids are. This adhesion force can be quantified experimentally by measuring the contact angles of sessile droplets on flat surfaces [36]. The sessile droplets spread and flatten for low contact angles, seeking to achieve a large contact area to the surface. For high contact angles, the opposite happens. In this case, the droplets strive towards minimizing their contact area with the solid surface, giving them a more sphere-like shape.

One way to categorize materials based on interfacial energy is to separate them into hydrophilic and hydrophobic materials. Hydrophilic materials have high adhesion forces to liquids; thus, liquids spread and flow easily on the surfaces of these materials. For hydrophobic materials, the opposite is the case. A common way to separate hydrophilic from hydrophobic is by determining whether their contact angle is above or below 90°. According to this definition, materials with a contact angle below 90° are considered hydrophilic, while materials with a contact angle higher than 90° are considered hydrophobic. Nevertheless, the scientific community has an ongoing debate regarding the validity and adequacy of this threshold-based categorization [37].

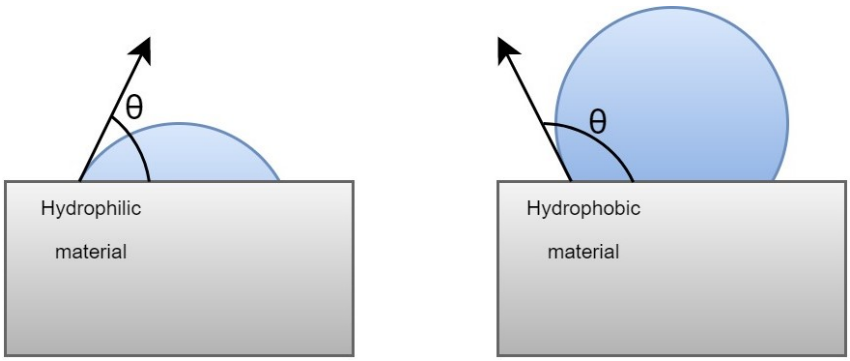

Figure 3.3: Droplet shape and contact angle for hydrophilic and hydrophobic surfaces

In addition to the adhesive forces, droplet geometry is significantly influenced by the surface roughness [21]. The microscopic irregularities and roughness of the surface profoundly affect the contact angle exhibited by a droplet. Consequently, it is essential to account for surface roughness to predict the contact angle accurately, necessitating a modification of Young's equation (3.2). Researchers have formulated several models to address the complex interaction between droplets and rough surfaces. Among these, the Wenzel and Cassie models [38, 39] are notably widespread. In the scenario of the Wenzels model, the premise is that the liquid creeps into all miniature cracks and holes in the surface, so the actual contact area between the surface and liquid is considerably more significant than the projected droplet area. In such a droplet state, the contact angle for the material can be found by

$$\cos\theta_a = \xi \cos\theta_w \tag{3.16}$$

θ_a is the apparent (experimental) contact angle, ξ is a roughness factor defined by the ratio of total surface area to the projected surface area, and θ_w is the contact angle for a smooth surface with the same adhesion force. On the other hand, the premise for the Cassie model is the droplet resting on the peaks of the rough surface. For this droplet state, the contact angle θ_{CS} can be defined as

$$\cos\theta_{CS} = -1 + \varphi(\cos\theta_a + 1) \tag{3.17}$$

φ is a factor determined by the average size and distance of the roughness peaks. Both Wenzel and Cassie droplet states and a combination of the two can co-exist on the same rough surface.

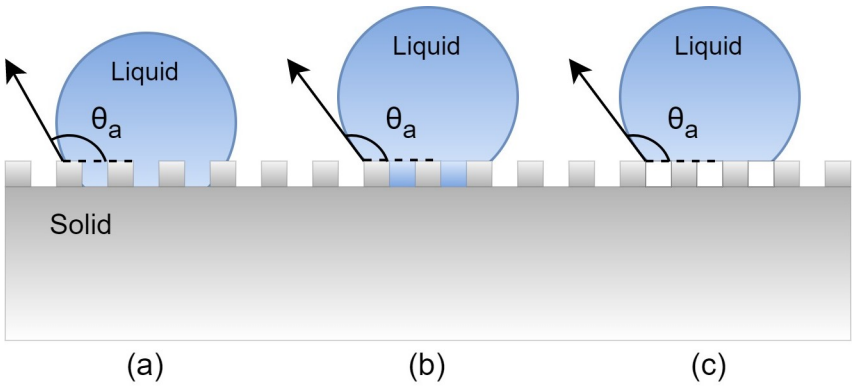

Figure 3.4: Wetting regimes over a rough surface; (a) Wenzel state (b) Partially wetting state (combined Wenzel and Cassie state) (c) Cassie state

According to El Fil et al. [21], it is easier for droplets to be removed in a Cassie state than in a Wenzel state. This is because the adhesion force is much lower in the Cassie state than in the Wenzel state due to the surface area of contact between solid and liquid being far lower.

3.1.3 Capillary action

Capillary action can be described as the process of liquids flowing into narrow spaces, like thin tubes, without assistance from external forces. The surface tension and the adhesive force between liquids and solids drive the capillary action. It is a vital function for many living organisms; for instance, trees utilize capillary action to transport water from their roots to the leaves [40]. An effort to understand the physics responsible for capillary action was initiated early in the 20th century [41]. Lucas and Washburn [42, 43] were the first to establish an expression for capillary flow speed.

Today, capillary action is utilized in various fields; for instance, in inkjet printing, the nozzle filling occurs due to capillary force [44]. In medical fields like microfluidics and drug delivery, capillary forces are also utilized for many purposes [45, 46]. Submerging a thin tube into a free water surface can relatively easily demonstrate capillary action. If the tube has a hydrophilic surface (contact angle $< 90°$), the water surface inside the tube will rise upwards until it reaches an equilibrium. This phenomenon is quantified by Jurin's law [47]

$$h = \frac{2\sigma_{LG}\cos\theta}{\rho g r} \tag{3.18}$$

where ρ represents the density of the liquid, θ the contact angle for the surface inside the tube, r is the tube radius, and h is the height of the capillary rise.

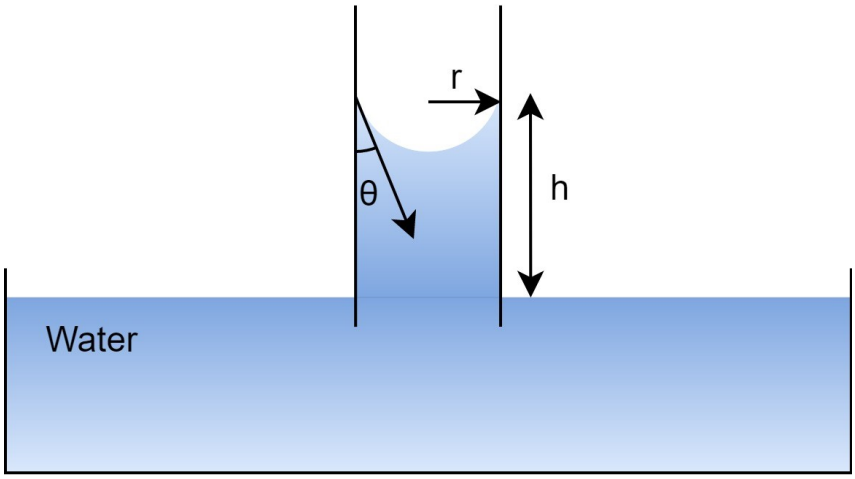

Figure 3.5: Schematic of capillary rise in a vertical tube

Jurin's law is derived by setting the surface tension pressure equal to the hydrostatic pressure in the tube. The surface tension pressure difference is calculated using the Young-Laplace equation (3.13) with only one main radius $R = \frac{r}{\cos\theta}$

$$-\rho g h = -2\sigma_{LG}\frac{\cos\theta}{r}. \tag{3.19}$$

An interesting context here is that the capillary force, due to surface tension, depends solely on the shape of the surface. The pressure induced by the capillary tube's surface is the negative pressure created by the surface of an axisymmetrical droplet with the same projected radius and $90° - \theta$ as the contact angle for the droplet.

Ivanov et al. [48] examined capillary tubes with variable cross-section areas. They present a coherent strategy for calculating forces onto a volume of water inside a conical tube or funnel, with two surfaces shared with air.

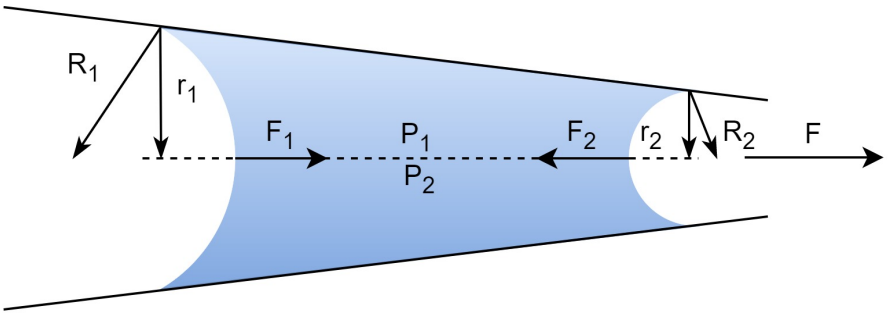

Figure 3.6: Schematic of capillary action in conical tube

They utilize the Young-Laplace equation to find terms for the pressure contributions of the two liquid surfaces. These pressure contributions are multiplied by the projected liquid surface areas A_1 and A_2 to receive the forces F_1 and F_2 exerted by the liquid surfaces.

$$p_1 = \frac{2\sigma_{LG}}{R_1} \tag{3.20}$$

$$F_1 = p_2 A_1 = 2\pi\sigma_{LG}\frac{r_1^2}{R_2} \tag{3.21}$$

$$F = F_1 - F_2 = 2\pi\sigma_{LG}\left(\frac{r_1^2}{R_2} - \frac{r_2^2}{R_1}\right) \tag{3.22}$$

The force equation 3.22 indicates that the liquid will flow towards the narrower section of the conical tube as long as the tube walls are hydrophilic. For a hydrophobic tube, the flow direction would be the opposite.

Equivalent to the sessile droplet discussed in subsection 3.1.1, the exact curvature in an axisymmetric cone under the influence of gravity can be found utilizing the differential form of the Young-Laplace equation (3.9). The boundary condition can be formulated by the height h of the water surface in the cone, the contact angle θ, and the cone slope angle α illustrated in figure 3.7.

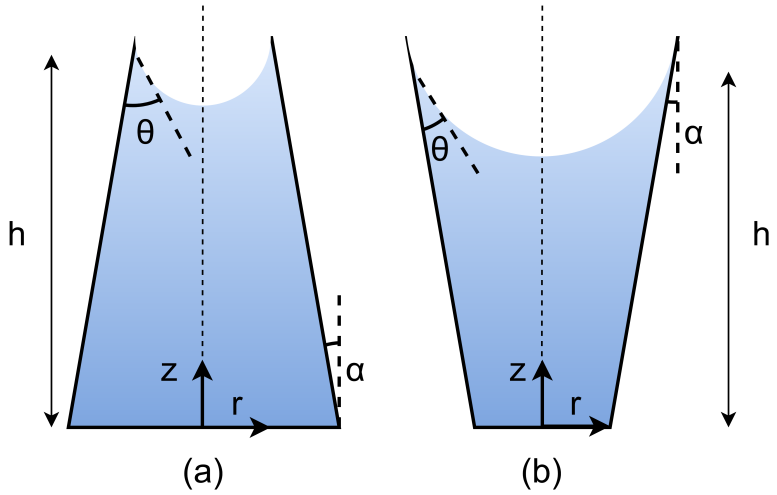

Figure 3.7: Schematic of surface curvature for (a) converging and (b) diverging cones

With these parameters, the boundary conditions presented in equations (3.23)-(3.25) can be used to obtain a unique solution.

$$z'(0) = 0 \tag{3.23}$$

$$z(r_{funnel}) = h \tag{3.24}$$

$$z'(r_{funnel}) = \tan(90° - \theta \pm \alpha) \tag{3.25}$$

Whether the slope angle α is added or subtracted from the contact angle θ depends on whether the cone diverges or converges along the z-direction. Figure 3.7 presents these two cases. For case (a), the cone converges, and thus, α is subtracted from θ. For case (b), the opposite is true.

If the sum of α and θ exceeds 90°, the surface curvature is no longer concave, as displayed in figure 3.7, but instead has a convex shape. This altered shape would encourage the liquid to flow in the direction opposite to that facilitated by a concave surface.

For the case where the slope angle α has the value of zero, the geometry is that of a straight cylinder. Furthermore, the differential Young-Laplace equation can be utilized using the same boundary conditions as for the case of the axisymmetrical cone.

Capillary action is not limited to round channels like tubes. Ouali et al. [49] investigated the spontaneous capillary-driven filling of microchannels with both open and closed rectangular cross-sections. They present Laplace-Young-derived equations, which can be utilized to calculate the capillary pressures for both open and closed

rectangular channels. These equations also take into account different side walls having different contact angles. For the case of a closed rectangular channel, out of two materials that do not share the same contact angle, where the opposite walls are from the same material, the capillary pressure can be described as

$$\Delta p = \sigma_{LG} \left(\frac{1}{R_1} + \frac{1}{R_2} \right) = 2\sigma_{LG} \left(\frac{\cos\theta_W}{W} + \frac{\cos\theta_d}{d} \right) \tag{3.26}$$

where W is the width of the channel, d is the depth, and θ_W/θ_d are the contact angles along the corresponding walls.

In later years, numerical analysis has become a valuable tool to understand capillary action further. Erickson et al. [50] conducted a numerical study of capillary flow in tubes with varying cross-section diameters. These simulation results were compared to simulations with constant cross-sections. In general, the results showed that the flow is significantly slower in the case of varying cross-sections than in the straight tubes. The difference was attributed to the slow interface advancement of the liquid going into a region with a larger diameter.

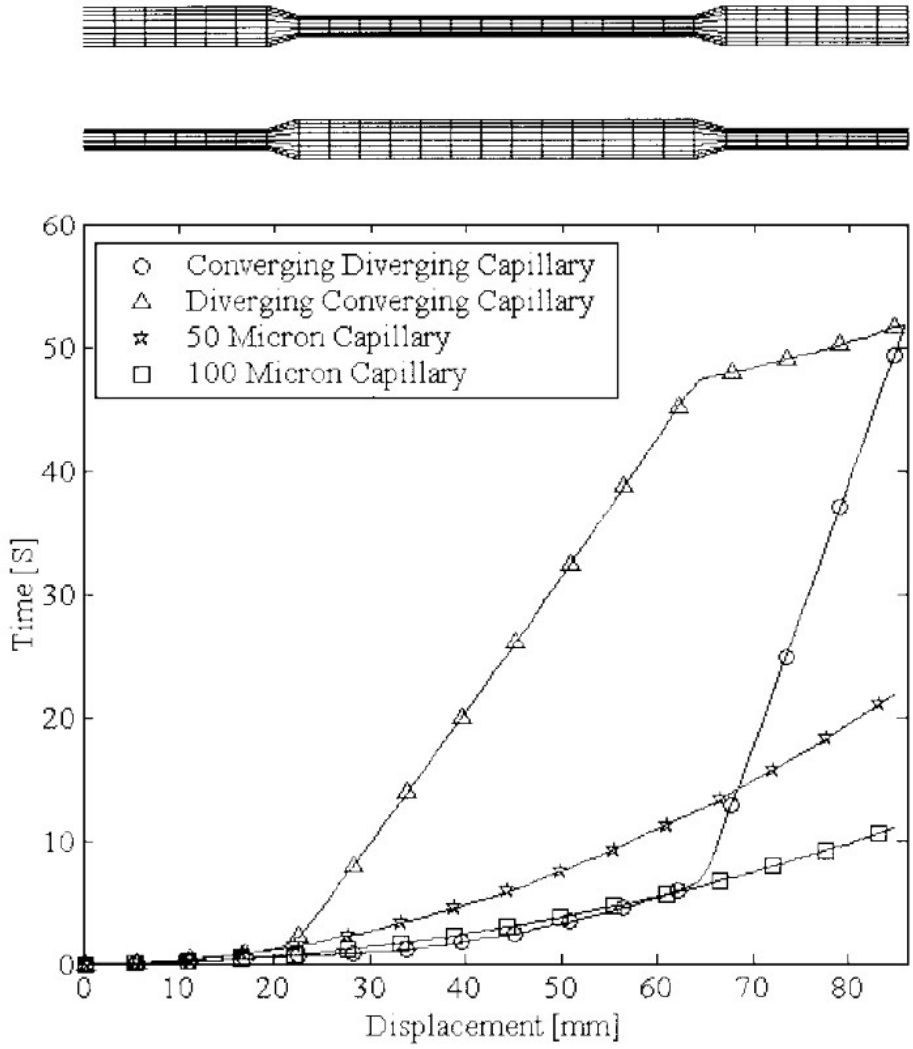

Figure 3.8: Displacement vs time plot for different capillary tubes

Source: Erickson et al. [50]

3.2 Two-Phase Flow Simulation Theory

Numerous numerical methods exist for simulating two-phase flows with surface tension, reflecting the diversity in approaches and scales at which fluid interactions can be analyzed [51]. Broadly, these methods can be categorized based on the discretization technique employed, namely Lagrangian or Eulerian, as well as the scale at which fluid physics is considered - macroscopic, microscopic, or mesoscopic. Hybrid methods that incorporate elements from multiple approaches are also prevalent.

The Lagrangian approach characteristically focuses on tracking and calculating the trajectories of individual fluid particles. This approach is often favored for its ability to capture detailed particle dynamics. In contrast, the Eulerian approach observes the evolution of fluid properties, such as concentration within discrete spatial elements. It monitors how these properties change within and between elements defined by a

computational mesh [52].

Macroscopic methods based on Eulerian discretization have historically dominated the field and remain prevalent. The most widely utilized methods within this category include the Volume of Fluid (VOF) method, the level-set method (LSM), and the phase-field method (PFM) [53]. Additionally, emerging methods such as the Lagrangian-based Smoothed Particle Hydrodynamics (SPH) [54] and the Eulerian-based mesoscopic Lattice Boltzmann Method (LBM) [55] have gained attention. These methods are notable for their suitability for parallelization, allowing them to harness the increasing computational power of Graphics Processing Units (GPUs) [56, 57].

This thesis predominantly concentrates on the level-set and phase-field methods, which have been chosen due to their reputable standing and extensive integration into major simulation software. In this section, the fundamental principles of simulating two-phase flows with surface tension are explored.

Both the level-set and phase-field method is based on incompressible flow, which follows the continuity equation (3.27) and the Navier-Stokes equation for incompressible fluids with surface tension and gravity defined by equation (3.28) [58].

$$\nabla \cdot \boldsymbol{u} = 0 \tag{3.27}$$

$$\rho \frac{\partial \boldsymbol{u}}{\partial t} + \rho(\boldsymbol{u} \cdot \nabla)\boldsymbol{u} = -\nabla p + \mu \nabla^2 \boldsymbol{u} + \rho \boldsymbol{g} + \boldsymbol{F}_{sv} \tag{3.28}$$

where F_{sv} is the volume force from the surface tension, which is derived from the normal vector version of the Young-Laplace equation (3.15)

$$\boldsymbol{F}_{sv} = -\sigma \kappa \nabla \Phi \tag{3.29}$$

where $\kappa = \nabla \cdot \hat{\boldsymbol{n}}$ is the curvature and Φ is the level-set variable or the phase-field variable.

3.2.1 Level-set method

This subsection will follow the level-set method presented by Olsson et al. [58] and Hua et al. [59]

The level-set method utilizes a scalar function, typically denoted by Φ, to represent the volume fraction of a fluid within a given computational cell. In this representation, $\Phi = 1$ indicates that a cell is fully occupied by fluid 2, whereas $\Phi = 0$ signifies the cell is fully occupied by fluid 1. Sometimes, Φ is defined to take a value of -1 instead of 0 to denote the presence of fluid 1. The interface between the two fluids is usually characterized by $\Phi = 0.5$. This formulation leads to the definitions for density and viscosity as given in equations (3.30) and (3.31), respectively.

$$\rho = \rho_1 + (\rho_2 - \rho_1)\Phi \tag{3.30}$$

$$\mu = \mu_1 + (\mu_2 - \mu_1)\Phi \tag{3.31}$$

For numerical robustness and to increase the convergence, Φ is sometimes calculated through smoothed Heaviside functions, as shown below:

$$\Phi = \begin{cases} 0, & \text{if } \phi < -\epsilon, \\ \frac{1}{2} + \frac{\phi}{2\epsilon} + \frac{1}{2\pi}\sin\left(\frac{\pi\phi}{\epsilon}\right), & \text{if } -\epsilon \leq \phi \leq \epsilon, \\ 1, & \text{if } \phi > \epsilon. \end{cases} \tag{3.32}$$

ϕ is an intermediate level-set parameter as explained by Olsson et al. ϵ represents half of the interface thickness and typically depends on the mesh size.

Surface tension is accounted for by incorporating the surface tension volume force, which is derived from the Young-Laplace equation (3.15). This force is given by equation (3.33).

$$\boldsymbol{F}_{sv} = \sigma\left(-\nabla \cdot \frac{\nabla\Phi}{|\nabla\Phi|}\right)\nabla\Phi \tag{3.33}$$

Here, $\frac{\nabla\Phi}{|\nabla\Phi|}$ represents the unit normal vector derived from the level-set function Φ.

The level-set method employs the continuity equation (3.27) and the Navier-Stokes equation (3.28) to solve for the velocity field, $\boldsymbol{u}$, in subsequent time steps. Additionally, the evolution of the level-set variable, Φ, is governed by the level-set equation (3.34), an interface variant of the Navier-Stokes equation.

$$\frac{\partial\Phi}{\partial t} + \nabla \cdot (\boldsymbol{u}\Phi) = \gamma\nabla \cdot \left(\epsilon\nabla\Phi - \Phi(\mathbf{1} - \Phi)\frac{\nabla\Phi}{|\nabla\Phi|}\right) \tag{3.34}$$

In equation (3.34), γ symbolizes a speed parameter that regulates the level of reinitialization or stabilization required for the level-set interface. The equation is initially presented in its conservative form. However, for computational efficacy, it can also be expressed in a non-conservative form:

$$\frac{\partial\Phi}{\partial t} + \boldsymbol{u} \cdot \nabla\Phi = \gamma\nabla \cdot \left(\epsilon\nabla\Phi - \Phi(\mathbf{1} - \Phi)\frac{\nabla\Phi}{|\nabla\Phi|}\right) \tag{3.35}$$

Although the non-conservative form is computationally more efficient, it may not conserve the total volume of the phases and can introduce numerical diffusion. However, by employing sufficiently fine mesh resolutions, the diffusion effects can be minimized to a practically negligible extent.

This level-set equation is typically decoupled into two distinct steps for numerical implementation: the advective step and the intermediate step.

1. The Advective Step: This step incorporates the influence of velocity on the interface by advancing the boundary at each stage. The conservative form of the advective step is given by

$$\frac{\partial \Phi}{\partial t} + \nabla \cdot (\boldsymbol{u}\Phi) = 0 \tag{3.36}$$

whereas the non-conservative form is

$$\frac{\partial \Phi}{\partial t} + \boldsymbol{u} \cdot \nabla \Phi = 0 \tag{3.37}$$

2. The Intermediate Step: In this step, the compressive flux is integrated into the solution. The conservative expression is

$$\frac{\partial \Phi}{\partial t} + \nabla \cdot \left(\Phi(\mathbf{1} - \Phi) \frac{\nabla \Phi}{|\nabla \Phi|} - \epsilon \nabla \Phi \right) = 0 \tag{3.38}$$

and the non-conservative form is

$$\frac{\partial \Phi}{\partial t} + \nabla \cdot \left(\Phi(\mathbf{1} - \Phi) \frac{\nabla \Phi}{|\nabla \Phi|} \right) = \epsilon \nabla^2 \Phi \tag{3.39}$$

By breaking down the level-set equation into these two stages, numerical stability is enhanced while accommodating the dynamic evolution of the fluid interface. This methodology enables the efficient simulation of complex interfacial phenomena inherent to multi-phase flows, such as surface tension and capillary action.

3.2.2 Phase-field method

The phase-field method, characterized by diffusion-based interface sharpness, offers a more pronounced interface than the level-set method. This subsection employs the equations put forth by Hua et al. [59].

The phase-field method uses Φ similarly to the level-set method, with $\Phi = -1$ and $\Phi = 1$ denoting 100% volume fractions of fluid 1 and fluid 2, respectively. The density and viscosity are interpolated as follows:

$$\rho = \rho_1 + (\rho_2 - \rho_1) \frac{\Phi + 1}{2} \tag{3.40}$$

$$\mu = \mu_1 + (\mu_2 - \mu_1) \frac{\Phi + 1}{2} \tag{3.41}$$

For the surface tension, phase-field utilizes multiple definitions, primarily based on the Young-Laplace equation. For example:

$$\boldsymbol{F}_{sv} = -\frac{3\sqrt{2}}{4}\sigma\epsilon\nabla\cdot\frac{\nabla\Phi}{|\nabla\Phi|}|\nabla\Phi|\nabla\Phi \tag{3.42}$$

In equation (3.42), ϵ signifies the thickness of the interface and is dependent on the mesh resolution.

Another expression based on the Young-Laplace equation is:

$$\boldsymbol{F}_{sv} = \frac{3\sqrt{2}}{4}\sigma\epsilon\nabla\cdot(|\nabla\Phi|^2 I - \nabla\Phi\otimes\nabla\Phi) \tag{3.43}$$

Here, $\nabla\Phi\otimes\nabla\Phi$ represents the tensor product of the gradient of Φ.

Additionally, a thermodynamics-based definition is:

$$\boldsymbol{F}_{sv} = \frac{3\sqrt{2}}{4\epsilon}\mu_{ch}\nabla\Phi \tag{3.44}$$

Where μ_{ch} is the chemical potential, expressed as:

$$\mu_{ch} = (\Phi^2(1-\Phi^2)^2 - \epsilon^2\nabla^2\Phi) \tag{3.45}$$

The governing equation for the phase-field method is the advective Cahn-Hilliard equation:

$$\frac{\partial\Phi}{\partial t} + \nabla\cdot(\boldsymbol{u}\Phi) = \chi\nabla^2(\Phi^2(1-\Phi^2)^2 - \epsilon^2\nabla^2\Phi) \tag{3.46}$$

In this equation (3.46), χ denotes the constant mobility, controlling the diffusion of Φ.

3.2.3 Interface thickness comparison

The level-set method has been widely employed and is well-established, as evidenced by various studies using the method in contexts similar to these studies [60, 61]. However, a notable distinction between the level-set and phase-field methods lies in the thickness of the interface separating the phases.

Figures 3.9 and 3.10 illustrate the topologies of the level-set and phase-field parameters, respectively. The figures elucidate that the interface in the phase-field method is significantly sharper than the level-set method for the exact mesh resolution. This implies that the phase-field method can provide a more accurate representation of the

phase interface, making it closer to real-world scenarios. This sharper interface in the phase-field method can be particularly advantageous in simulations where high precision is required at the interface, such as capillary forces in a channel with rapidly changing geometry.

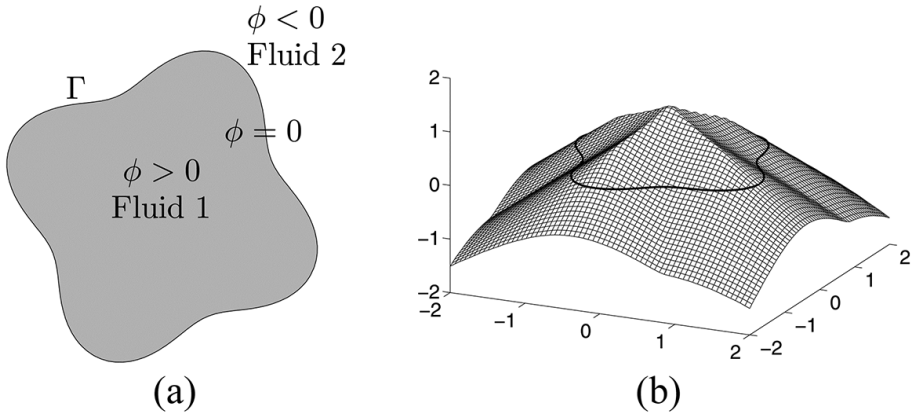

Figure 3.9: Topology representation in the level-set method. Note that in this thesis, fluid 2 is represented by $\Phi = 1$, and fluid 1 is represented by $\Phi = 0$.

Source: Hua et al. [59]

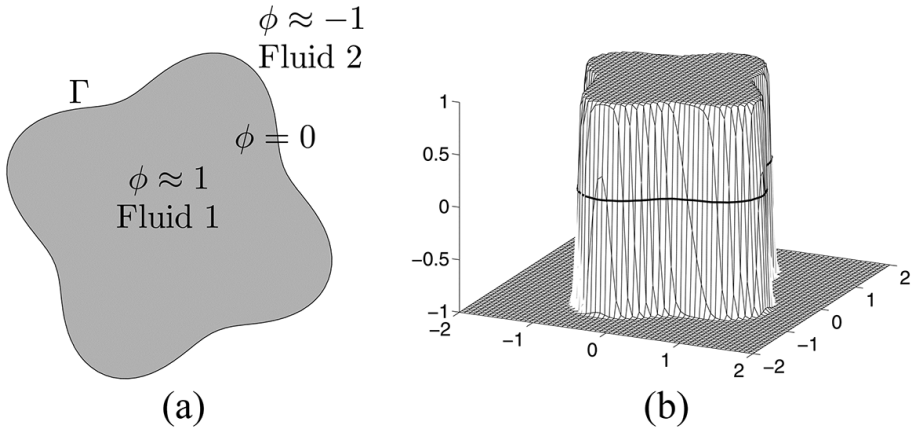

Figure 3.10: Topology representation in the phase-field method.

Source: Hua et al. [59]

4 Hourglass Concept

This chapter presents the hourglass concept for controlling liquid flow in the EBC collection. The concept is described before delving into the theoretical derivation that explains the forces and geometrical parameters involved. The implementation of the concept demonstrated through a practical Inflammacheck® use scenario is then detailed. Finally, the model is critically evaluated, highlighting potential limitations due to material properties, surface imperfections, and theoretical simplifications.

4.1 Concept Description

The previously discussed capillary action in channels with varying cross-sections can serve as a means to both accelerate and decelerate liquid flow. In combination with the gravity force, this can be utilized to collect EBC up to a critical volume before accelerating the volume toward the biosensor. The novel approach termed the "hourglass concept" is visualized in Figure 4.1. The concept is based on a vertical, rectangular cross-section channel with varying width and constant depth (out of plane). Seen from the top and downwards, the channel first narrows before it widens again. At the bottom, the channel narrows suddenly and transitions into a straight rectangular channel. The surfaces of the channel are hydrophilic.

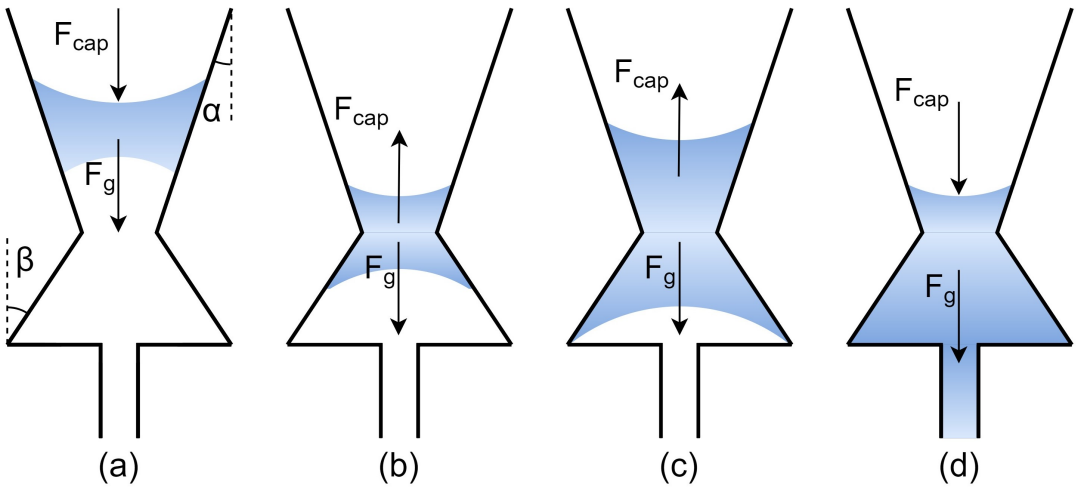

Figure 4.1: EBC collection and release with hourglass concept

When EBC enters the channel, gravity forces $F_g = \rho g V$, and capillary forces F_{cap} will influence the liquid to flow downwards. This continues until the liquid has reached the point where the channel widens again. Once a sufficient volume has passed across the transition point from converging to diverging, the vector of the net capillary force will

point upwards. When this force equals gravity, the liquid reaches a stationary equilibrium. As more EBC is added, the stationary volume grows until its bottom surface reaches the straight channel. When the liquid enters the straight channel, the vector of the net capillary force will once again point in the same direction as the vector of the gravity force, and the liquid will continue to flow downwards. After the upper boundary of the volume has passed the transition point, the vector of the net capillary forces again changes directions, and the volume moves toward a new stationary equilibrium.

For the Inflammacheck® use scenario, both the equilibrium around the hourglass neck in figure 4.1.b and the final equilibrium in figure 4.1.d are useful. The dimensions of the channel can be chosen in such a way that the first equilibrium can be utilized to collect a sufficient volume of EBC before introduction. In contrast, the second equilibrium can ensure that no fluid escapes from the testing cartridge.

4.2 Theoretical Derivation

To utilize the hourglass concept in practice, a theoretical understanding of the problem is required. Knowing how geometry parameters and contact angles influence the shape of the liquid volume at the stationary equilibrium is vital for designing a functioning solution.

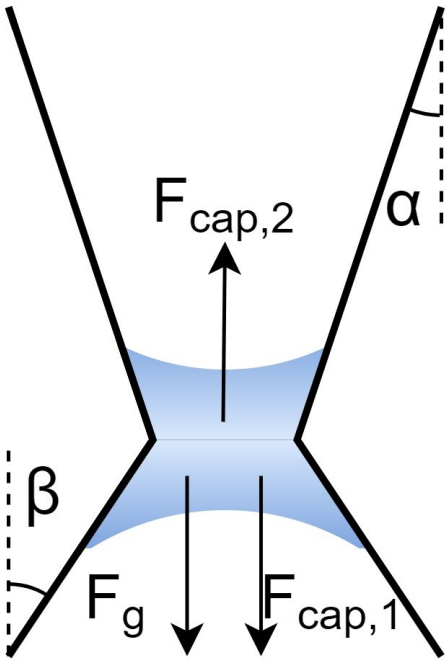

Figure 4.2: Schematic of force equilibrium in hourglass-shaped channel

A starting point for this is considering the force equilibrium in the vertical direction.

$$\sum F_z = 0 = -F_g - F_{cap,1} + F_{cap,2} \tag{4.1}$$

The two capillary force contributions can be expressed using equations (3.21) and (3.26). The pressure contribution from the upper surface is expressed as

$$P_1 = \sigma_{LG} \left(\frac{\cos(\theta_W + \alpha)}{x_1} + \frac{2\cos\theta_d}{d} \right) \tag{4.2}$$

where α is the slope of the converging (upper) section of the channel (figure 4.2) and x_1 is half the width ($W/2$) of the channel at the height of the upper surface. Here it is assumed that the gravity force is negligible for the formation of the surface curvature. The resulting force from this pressure, F_2, is found by multiplying the pressure with the cross-section area of the bottom liquid surface.

$$F_2 = 2d\sigma_{LG} \left(\frac{x_2}{x_1} \cos(\theta_W + \alpha) + x_2 \frac{2\cos\theta_d}{d} \right) \tag{4.3}$$

F_1 can be found utilizing the same strategy, giving the updated expression for the force equilibrium

$$\sum F_z = 0 = -\rho g V + 2d\sigma_{LG} \left(\frac{x_2}{x_1} \cos(\theta_W + \alpha) - \frac{x_1}{x_2} \cos(\theta_W + \beta) + (\frac{2\cos\theta_d}{d})(x_2 - x_1) \right) \tag{4.4}$$

Assuming knowledge of the channel slope angles α and β, the contact angles θ_W and θ_d, the liquid-gas surface tension σ_{LG}, the depth d, and the volume V, the equation (4.4) maintains two undefined variables, x_1 and x_2. These parameters describe the liquid volume fraction above and below the transition point, where the channel transitions from converging to diverging.

A relation between x_1 and x_2 can be obtained through the liquid volume expression. An approximation of the total volume, not considering the volume change due to the out-of-plane curvature, can be derived from calculating the volume of the two trapezoidal liquid prisms and subtracting the liquid volume of the two cylinder segments that form the water displaced by the surface tension. This simplification is viable for cases where $W >> d$.

$$V = V_{trap,1} + V_{trap,2} - V_{cyl,1} - V_{cyl,2} \tag{4.5}$$

$$V_{trap,1} = \frac{x_1^2 - x_{min}^2}{\tan\alpha} d \tag{4.6}$$

$$V_{trap,2} = \frac{x_2^2 - x_{min}^2}{\tan\beta} d \tag{4.7}$$

$$V_{cyl,1} = \frac{[\pi - 2(\theta_W + \alpha) - \sin(2(\theta_W + \alpha))]}{2\cos^2(\theta_W + \alpha)} dx_1^2 \tag{4.8}$$

$$V_{cyl,2} = \frac{[\pi - 2(\theta_W + \beta) - \sin(2(\theta_W + \beta))]}{2\cos^2(\theta_W + \beta)} dx_2^2 \tag{4.9}$$

Here, x_{min} is defined as half of the channel width at the height of the transition point ($W_{min}/2$). The equation can be rearranged to obtain an expression for x_2, depending on x_1.

$$x_2 = \sqrt{\frac{-V_{trap,1} + \frac{d}{\tan\beta} x_{min}^2 + V_{cyl,1} + V}{\frac{d}{\tan\beta} - V_{cyl,2}}} \tag{4.10}$$

Equations (4.4) and (4.10) now form a set of two equations with two variables and thus possess a unique solution.

4.3 Implementation

With some effort, the set of equations presented in the theoretical derivation can be solved analytically. However, it is solved numerically with relative ease. This is demonstrated by using the input parameters presented in table 4.1.

Table 4.1: Input parameters for numerical solving of x_1 and x_2

Parameters	V	d	x_{min}	α	β	θ_W	θ_d
Values	10 μL	0.8 mm	0.5 mm	10°	20°	60°	60°

For these input parameters, the resulting geometry of the volume can be seen in figure 4.3. The body to the left displays the front view, while the right body showcases the side view. Table 4.2 presents the resulting volume geometry's output data.

The parameter termed "Volume fraction" signifies the percentage of the liquid located above the transition point. This value is of significant interest as it reveals the substantial volume of liquid directed toward the biosensor before the second equilibrium point is attained. To minimize the EBC collection time, it is beneficial to maximize the volume fraction of the liquid situated above the transition point.

Altering the input parameters independently and methodically yields insights into their effects on the volume fraction above the transition point. A parametric investigation reveals that the volume fraction increases with the degree of hydrophilicity for the channel

walls, as well as the magnitude of the fraction β/α. Furthermore, reducing the distance W_{min} amplifies the volume fraction.

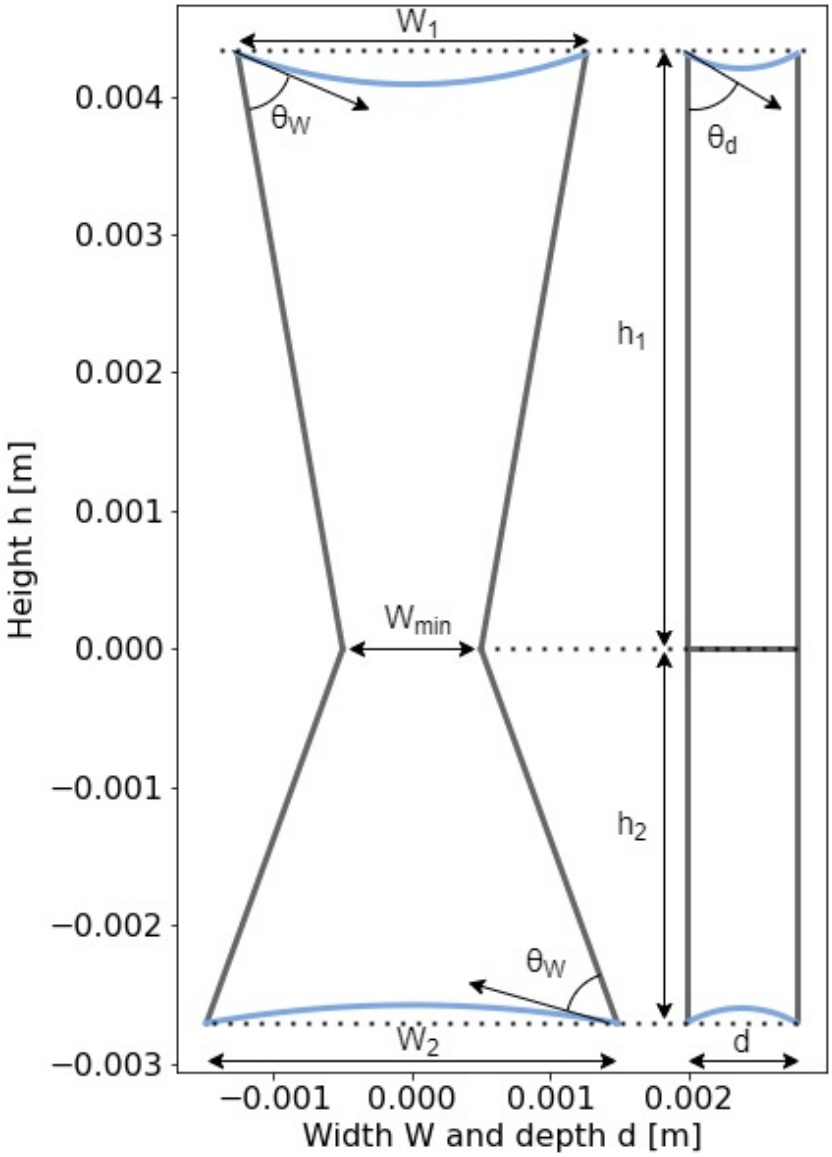

Figure 4.3: Resulting equilibrium state geometry for input parameters for table 4.1

Table 4.2: Output data for volume displayed in figure 4.3

Parameter	Value
W_1	2.52 mm
W_2	2.97 mm
W_{min}	1.00 mm
h_1	4.31 mm
h_2	2.70 mm
Volume fraction	58.5 %

4.4 Evaluation

While the hourglass concept carries significant potential, there are uncertainties and potential sources for error due to material properties, surface imperfections, and simplifications made in the theoretical derivation.

In the theoretical derivation, several simplifications were employed. For instance, all liquid-gas surfaces are modeled, disregarding the impact of gravity onto the surface curvatures, allowing their representation through merely two principal radii rather than a nonlinear differential equation (see equation (3.9)). However, in reality, gravitational forces influence both surfaces, enlarging the principal radii for the lower surface while diminishing it for the upper surface. This phenomenon consequently generates a net force directed upwards.

As previously stated, the equation for the total volume also contains a significant simplification. Specifically, the volume reduction caused by the out-of-plane curvature (θ_d) is disregarded. This simplification is predicated on the assumption that $W >> d$. However, the disparity cannot render the out-of-plane curvature completely negligible.

The resulting theoretical formulation also imposes certain constraints due to cosine terms in the equation set. Specifically, to ensure valid and consistent results, the contact angle θ_d, along with the combinations $\theta_W + \alpha$ and $\theta_W + \beta$, cannot surpass 90 degrees. These restrictions inherently define the lower limit of hydrophilicity that the model can effectively accommodate.

The model also fundamentally presumes that the channel walls are devoid of imperfections. However, in reality, all surfaces exhibit a certain degree of roughness. These microscopic irregularities can introduce additional variables and complications into the system's behavior, potentially affecting the fluid dynamics and altering the results predicted by an overly idealized model. Hence, the assumption of perfect smoothness simplifies the model but at the cost of fully capturing the complex reality of actual surfaces.

5 Numerical Study

In this chapter, the numerical simulation of capillary flow due to surface tension is presented. It begins with an overview of the software used and the strategy employed. After that, the strategy is validated through comparisons with analytical solutions before a parametric study of the hourglass geometry presented in chapter 4 is conducted and discussed.

There is a preference for employing well-established software with robust online resources for numerical simulations to ensure reliability and ease of access to support material and cost-effectiveness. After evaluating the available options, OpenFOAM, Ansys, and COMSOL emerge as potential candidates. The essential criteria include the software's capability to manage laminar two-phase flow while maintaining a constant contact angle. OpenFOAM features an API for contact angle [62] and implements the level set method [63], but falls short in terms of documentation and available examples or articles. In contrast, Ansys Fluent incorporates the Volume of Fluid (VOF) method and supports contact angles [64], offering substantial documentation but lacking examples and articles. COMSOL distinguishes itself with versatile support for phase-field, level-set, and moving mesh methods, along with extensive documentation [65]. The abundance of articles and guides makes it especially appealing, and given the limited experience in two-phase flow simulation, COMSOL emerges as the most accessible platform.

The simulations investigate four different geometries, utilizing COMSOL two-phase flow simulations. The first three are displayed in figure 5.1. A sessile droplet, a straight cylinder, and a funnel are utilized to validate the COMSOL model, as static analytical solutions for their surface curvatures can be derived from the Young-Laplace equation (3.9). Subsequently, the fourth geometry, an hourglass shape, is examined as referenced in Figure 4.2. For this geometry, parametric studies investigate the influence of different parameters on the capillary flow.

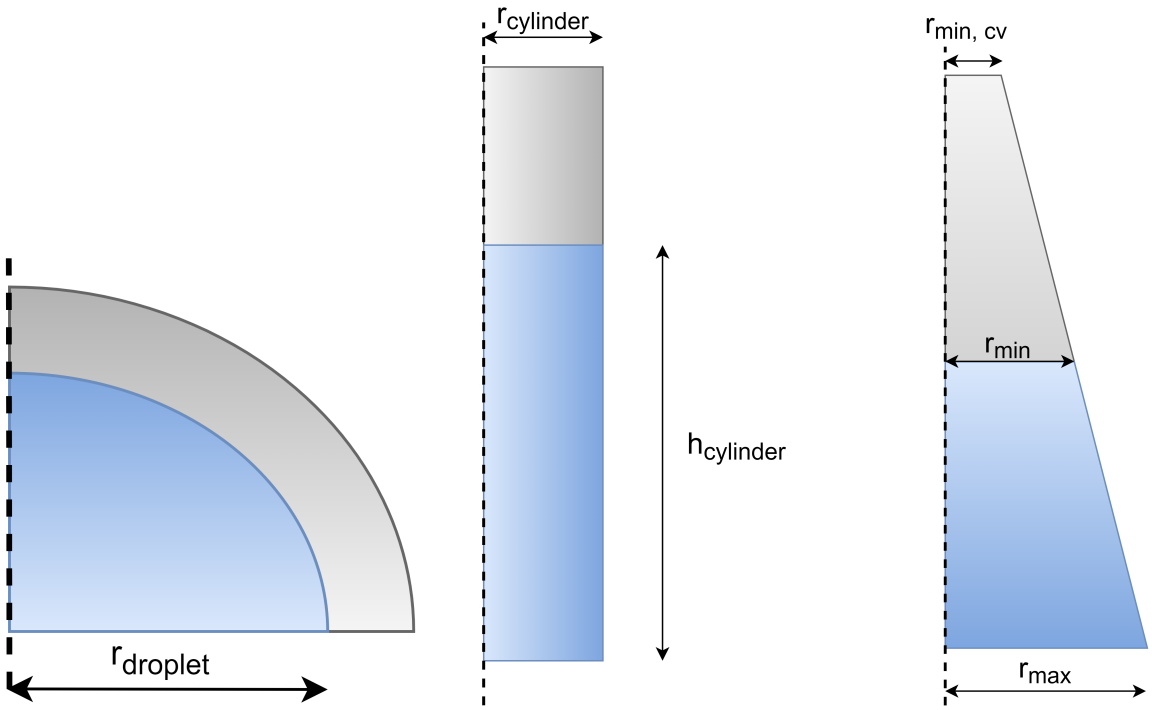

(a) Droplet (b) Cylinder (c) Funnel

Figure 5.1: The main geometries used in the numerical simulations. The droplet 5.1a, cylinder 5.1b, and the funnel 5.1c will be revolved around the centerline and will be mainly used for validation of the numerical simulations.

5.1 COMSOL Setup

To achieve comprehensive control over the simulation and automate processes such as parameter studies and plot generation, the COMSOL with MATLAB LiveLink interface is utilized.

Material Data: Standard properties from COMSOL's database for air and water are employed, but the density and surface tension are manually defined to maintain consistency with analytical simulations. Specifically, the densities are set to 997.048 kg/m^3 for water and 1.205 kg/m^3 for air, with a surface tension of 0.0728 N/m.

Geometry Configuration: The geometries are created as 2D axisymmetric models, considering the input liquid volume V and C, which approximates the control volume's relative volume compared to the liquid volume. Each geometry—droplet, cylinder, funnel (with both orientations), and hourglass shape—is mathematically defined through specific equations considering parameters like curvature radii, contact angles, and radius ratios.

For example, the dimensions for the droplet and cylinder geometries are determined using the following equations:

Droplet:

$$R_{droplet} = \left(\frac{3V}{\pi(2 + \cos\theta_W)(1 - \cos\theta_W)^2} \right)^{\frac{1}{3}} \tag{5.1}$$

$$r_{droplet} = R_{droplet} \sin\theta_W \tag{5.2}$$

Cylinder:

$$r_{cylinder} = \left(\frac{6V \cos^3\theta_W}{6hr_{ratio} - (1 - \sin\theta_W)(3\cos^2\theta_W + (1 - \sin\theta_W)^2)} \right)^{\frac{1}{3}} \tag{5.3}$$

$$h_{cylinder} = \frac{V}{\pi r_{cylinder}^2} \tag{5.4}$$

Similar equations are derived for the funnel and hourglass geometries.

3D Model Generation: 3D models are generated by revolving the 2D axisymmetric geometries around the z-axis or extruding them, noting that the extruded models do not maintain the same volume as the input.

Flow Simulation: The COMSOL Laminar Flow module is utilized to simulate the flow governed by the Navier-Stokes equation. Gravity is incorporated into this module, and zero static pressure inlets and outlets are defined, accounting for hydrostatic pressure.

Level-set Method: The Level-Set module is adopted, where stabilization techniques—streamline diffusion, crosswind diffusion, and dynamic subgrid time scale—are enabled, and linear elements with a non-conservative form are used. The reinitialization parameter, γ, is set to 0.001 m/s, and the interface thickness is default-calculated from the mesh. Initial phases are also defined for each geometry.

Phase-field Method: The Phase-Field module is employed using linear elements with a non-conservative form. The interface thickness is default-determined from the mesh. The mobility tuning parameter, χ, is set to 1 mm s/kg, which has a limited impact on the simulation as outlined in appendix A.2.1. As with the Level-Set method, initial phases are defined for each geometry, contact angles are specified, and inlets and outlets are set up.

Multiphysics Coupling: Multiphysics coupling is achieved by integrating the Laminar Flow and Level-Set modules using "Two-Phase Flow, Level Set" and "Wetted Wall" modules. For the Phase-Field method, "Two-Phase Flow, Phase Field" is used for coupling. Density and viscosity calculations are configured to "volume average", and surface tension is set to 0.0728 N/m. In the Level-Set, the Wetted Wall module is used to specify contact angles for various walls, and the slip condition is configured to Navier slip.

Mesh Generation: An automatic physics-controlled mesh generator provided by COMSOL is employed, which utilizes tetrahedrons and triangular prism elements.

Through this setup, a balance between computational efficiency and accuracy in capturing fluid dynamics within the various geometries under consideration is sought.

5.2 Validation

A numerical validation is conducted to identify a suitable approach and appropriate input parameters for the COMSOL models, aiming to yield results that align closely with real-world conditions. Five important factors will be established through this verification, and they are listed below:

1. **Gamma (γ)**
   Description: The reinitialization variable in the level-set method from equation 3.34
   Goal: Find the optimal value for accuracy and computation time
   Impact: Right parameter will increase convergence and/or give a more accurate interface boundary

2. **Chi (χ)**
   Description: The constant mobility in the phase-field method from equation 3.46
   Goal: Find the optimal value for accuracy and computation time
   Impact: Right parameter will increase convergence and/or give a more accurate interface boundary

3. **Level-set or phase-field**
   Description: These are two numerical methods used for tracking interfaces.
   Goal: Compare the solver results for accuracy, convergence rate, and numerical diffusion to decide which method is more efficient for this problem.
   Impact: The choice between level-set and phase-field can affect the accuracy of the interface tracking and computational efficiency.

4. **3D or 2D axisymmetric**
   Description: This parameter determines whether the simulation is performed in three dimensions or if it is reduced to a 2D axisymmetric representation.
   Goal: Compare the results from both to assess if a 2D axisymmetric approximation can adequately capture the essential characteristics of the 3D system.
   Impact: Choosing 2D axisymmetric simulations can significantly reduce computation time and resources but might miss some 3D effects.

5. **Mesh size**
   Description: Mesh size refers to discretizing the computational domain into small elements or cells.
   Goal: Investigate how the mesh size affects the convergence rate and numerical diffusion to optimize computational time without compromising accuracy.
   Impact: A finer mesh may result in more accurate simulations but at the cost

of increased computational time, whereas a coarser mesh may be computationally efficient but less accurate.

The droplet, cylinder, and funnel shapes, due to their accessible analytical solutions, are well suited to reveal the optimal setup for a two-phase flow simulation. This includes considerations for stability, accuracy, and time to run the simulation. The surface curvature, pressure variation across the phase interface, and numerical diffusion for these three shapes are examined. These aspects can offer valuable insights, enabling comparison between 2D and 3D simulations, evaluating level-set and phase-field methods, and determining a mesh size that offers plausible results while keeping the computational time acceptable low. Figures 5.2 through 5.8 showcases a selection of results from the validation study. The rest of the figures are in the appendix A.2. All validation simulations were completed without outlets and inlets to ensure static results were comparable with the analytical solutions.

Parametric studies were carried out for the input values of γ and χ, which are key parameters affecting the convergence speed for the level-set and phase-field methods. The result of these investigations is in appendix A.2.1 and concluded that $\gamma = 1$ mm/s and $\chi = 1$ mm·s/kg yielded a satisfyingly high rate of convergence and low numerical diffusion.

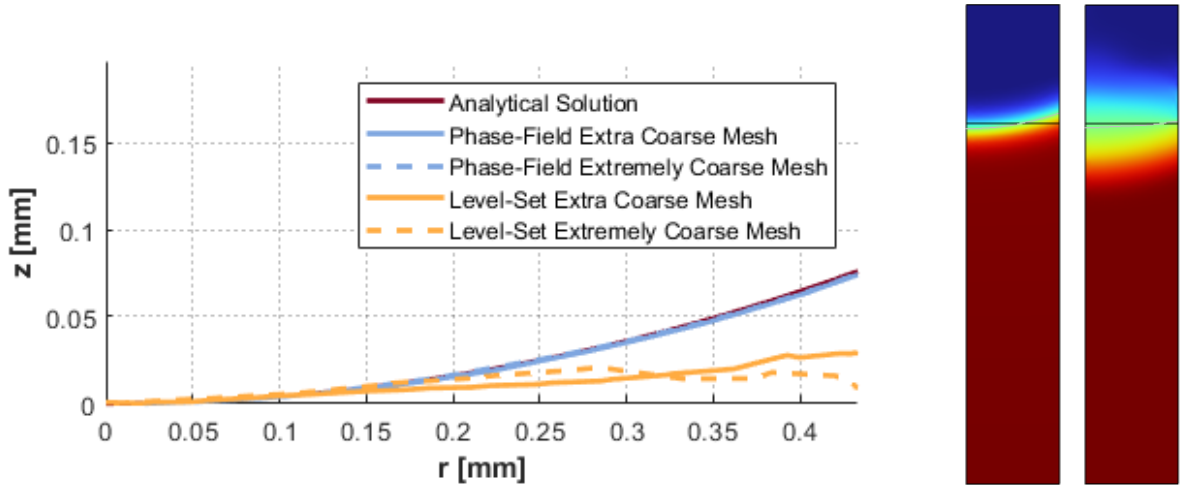

(a) (b) (c)

Figure 5.2: 5.2a show the interface curve between phases in a cylinder with 1 mm^3 volume of water and $\theta_W = 70°$ after 5 ms. The analytical is calculated by solving the axisymmetric version of the Young-Laplace equation (3.9) with the boundary condition $z'(r_{cylinder}) = \tan(90 - \theta_W)$. 5.2b shows the volume fraction of the cylinder simulated with phase-field and "Extra Coarse Mesh". The red color represents fluid 2, the water, and the blue color represents fluid 1, the air. 5.2c shows the volume fraction of the cylinder simulated with level-set and "Extra Coarse Mesh"

Figure 5.2 illustrates the surface curvature of a straight cylinder using the analytical solution, level-set method, and phase-field method implemented in a 2D axisymmetric model. Surface curvature data from simulations are collected by plotting all data points where the water volume fraction equals 50%. This is where Φ is 0.5 for the level-set and 0 for the phase-field. The coordinates for this exact value were calculated with interpolation between elements. A visual examination of the figure reveals that the phase-field simulations closely align with the analytical solution.

In contrast, the level-set simulations exhibit instability and fail to deliver consistent results. Comparing subfigures 5.2.2 and 5.2.3, one can discern a large contrast in the interface thickness between water and air. The phase-field method's capability to model a low interface thickness using a coarse mesh becomes a notable advantage. Although reducing the interface thickness for the level-set method could be achieved by decreasing the mesh size or using higher-order elements, such adjustments would substantially elevate computation time.

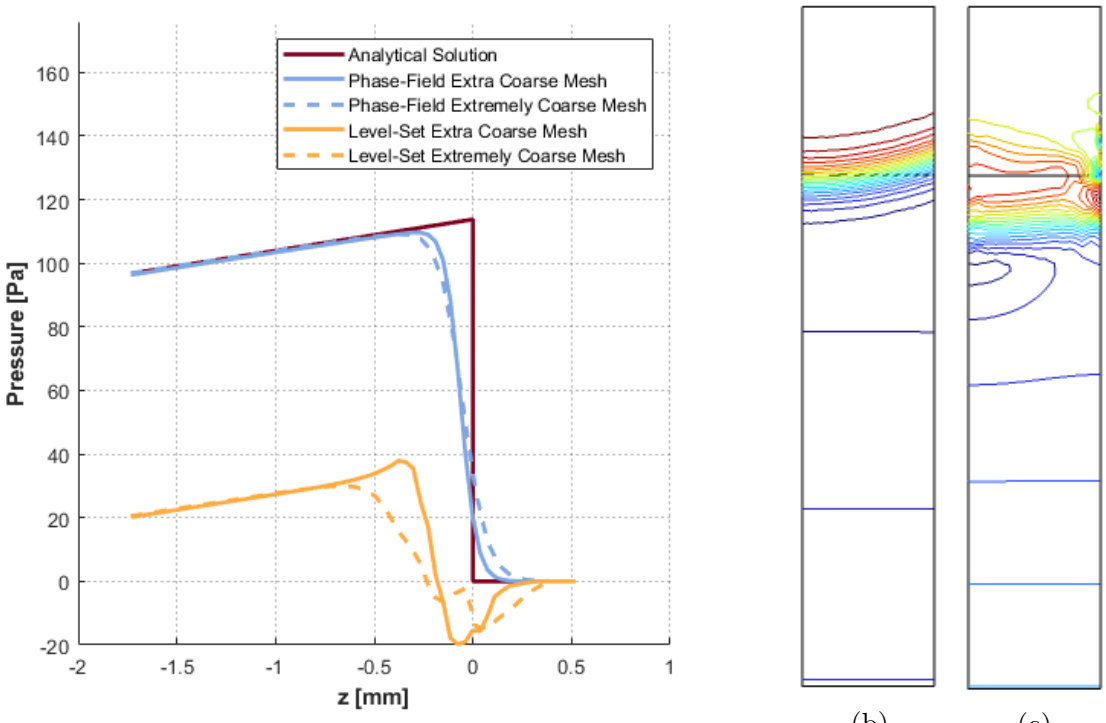

Figure 5.3:]
5.3a shows pressure along the centerline for a 2D axisymmetric cylinder with 1 mm^3 volume of water and $\theta_W = 70°$ after 5 5 ms. The analytical pressure difference in the interface is calculated from the curvature of the solution in figure 5.2a. 5.3b shows the contour-plot of the pressure for the simulation with phase-field and "Extra Coarse Mesh". 5.3c shows the contour-plot of the pressure for the simulation with level-set and "Extra Coarse Mesh".

Examining pressure along the centerline for both the level-set and phase-field simulations provides further insights into the superior agreement of the phase-field method with the

analytical solution compared to the level-set method. With the phase-field method, the slight divergence from the analytical solution largely stems from the non-infinitesimal size of the interface layer. The deviation observed between the extra coarse and extremely coarse mesh reinforces that the discrepancy between the analytical solution and the results from phase-field simulations can primarily be ascribed to mesh size considerations.

For the funnel geometry, the surface curvature and pressure results follow the same trend as for the straight cylinder, with the phase-field method returning far better results than the level-set method. However, for the droplet geometry, the results are not quite as clear as showcased in figure 5.4. Although the phase-field method also returns stable results for the droplet geometry, the results differ substantially from the analytical solution. Interestingly, the level-set simulation with the extremely coarse mesh returns the most accurate results compared to the analytical solution. The level-set droplets are smaller since the interface thickness is much larger than in the phase-field method.

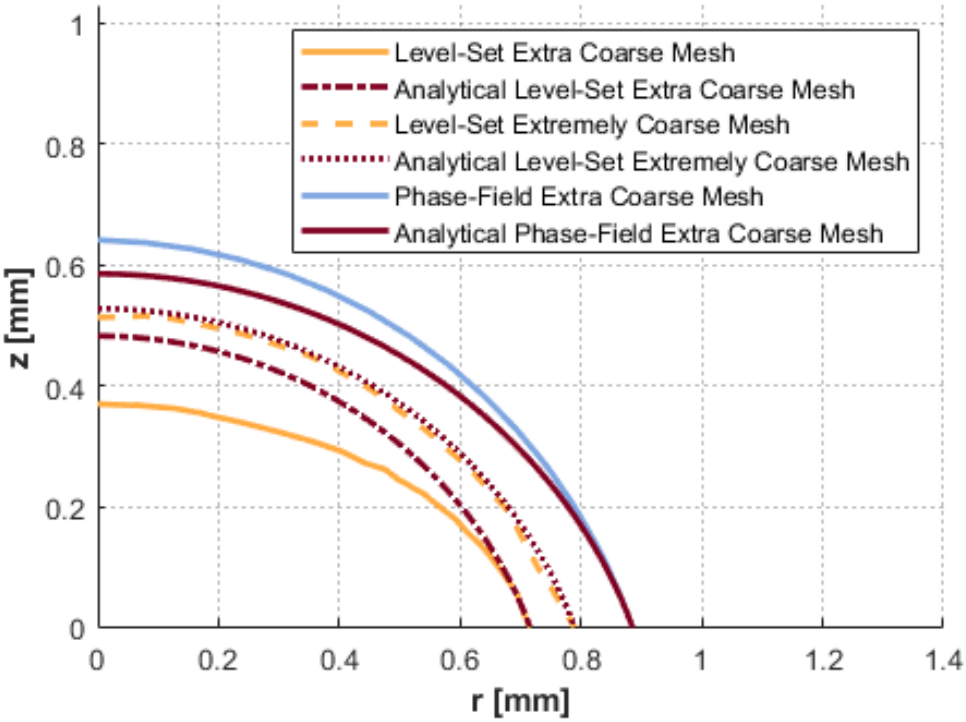

Figure 5.4: The interface curve between the phases in a droplet with $1\,\mathrm{mm}^3$ volume of water and $\theta_W = 70°$ after 5 ms. The analytical is calculated by solving the axisymmetric version of the Young-Laplace equation (3.9) with the boundary condition $z'(r_{droplet}) = -\tan(\theta_W)$. Note that there are 3 different analytical solutions since the boundary condition depends on the droplet's radius. Phase-field with "Extremely Coare Mesh" is not included since it failed to converge.

The appearance of three distinct analytical solution graphs in the plot can be attributed to the different dependencies of the analytical solution and the simulations. Specifically,

the analytical solution depends on the input radius r, while the input volume V influences the simulations. Consequently, the employed procedure involved initially simulating the shape of a droplet using the specified volume V, then determining the resulting radius r from this model, and finally calculating the associated analytical solution. Given the primary focus on capillary flow within enclosed channels, the phase-field method is the most suitable approach for this thesis.

Figures 5.5 and 5.6 illustrates the surface curvature for the 3D simulation of a straight cylinder. Again, only the phase-field method yields results that resonate with physical reality. Due to an expanded mesh size in the 3D model, the interface thickness is notably larger than the 2D axisymmetric model. Nevertheless, this enlargement has a minimal effect on the resultant surface curvature.

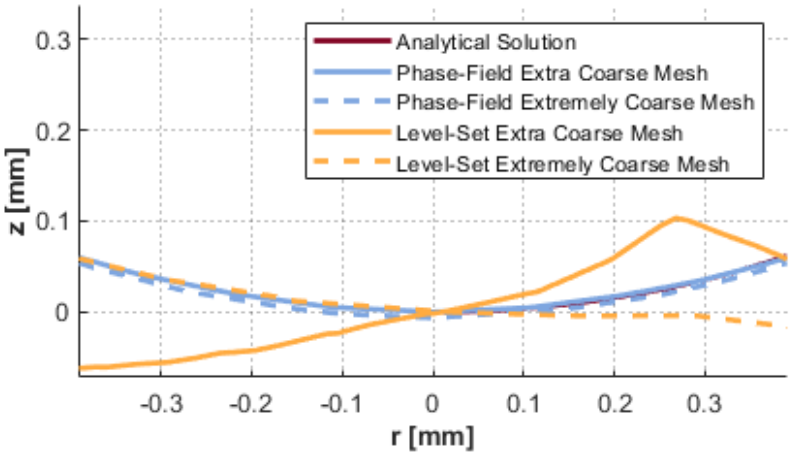

Figure 5.5: The interface curve between the phases in a 3D cylinder with 1 mm^3 volume of water and $\theta_W = 70°$ after 5 ms. The analytical is calculated by solving the axisymmetric version of the Young-Laplace equation (3.9) with the boundary condition $z'(r_{cylinder}) = \tan(90 - \theta_W)$.

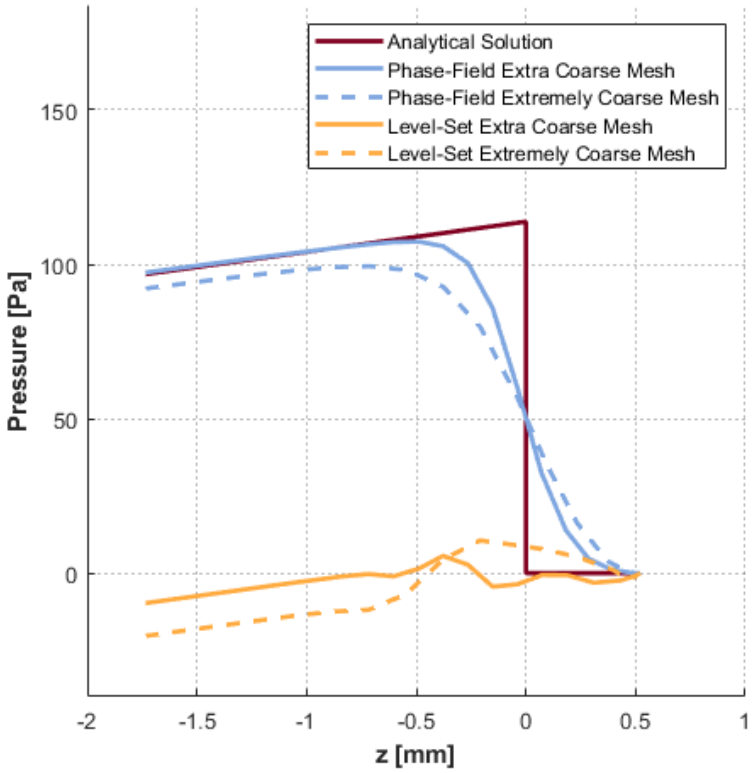

Figure 5.6: The pressure along the centerline for a 3D cylinder with $1\,\mathrm{mm}^3$ volume of water and $\theta_W = 70°$ after 5 5 ms. The analytical pressure difference in the interface is calculated from the curvature of the solution in figure 5.5.

In terms of numerical diffusion, there was a considerable discrepancy between the 2D axisymmetric model and the 3D model, as can be seen in figures 5.7 and 5.8. In fact, the numerical diffusion increases by approximately a factor of 10 from the 2D to the 3D model. However, the overall magnitude of numerical diffusion is merely about two percent for the 3D model. This diffusion seems solely dependent on mesh resolution and remains constant throughout the subsequent simulations.

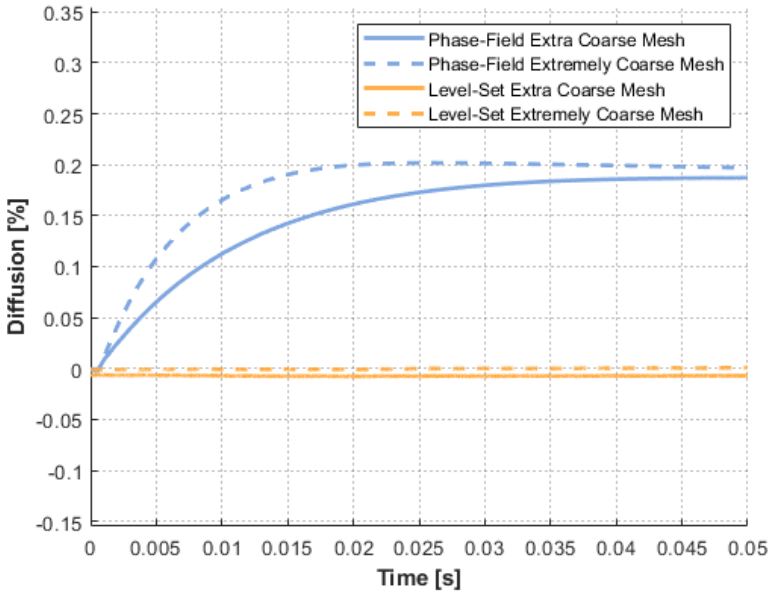

Figure 5.7: The percentage of the volume of water diffused over time in the axisymmetric cylinder with initial volume $1\,\mathrm{mm}^3$ and $\theta_W = 70°$. Some volume is always lost to the phase initialization since the meshes are too coarse to start with the given volume of water. The diffusion is calculated by surface integrating the volume fraction over all elements and dividing by the initial volume.

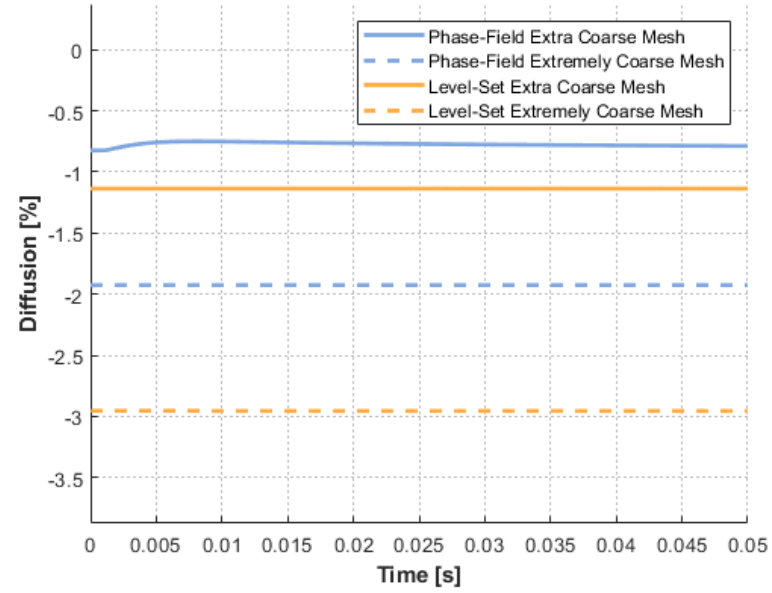

Figure 5.8: The percentage of the volume of water diffused over time in the 3D cylinder with initial volume $1\,\mathrm{mm}^3$ and $\theta_W = 70°$. Some volume is always lost to the phase initialization since the meshes are too coarse to start with the given volume of water. The diffusion is calculated by volume integrating the volume fraction over all elements and dividing by the initial volume.

5.3 Hourglass Flow Parametric Study

In chapter 4, an EBC collecting and deploying concept was presented, relying on capillary action in channels with varying cross-sections, specifically hourglass-shaped channels. Thus, it is interesting to investigate how physics, material properties, and geometric parameters influence the capillary flow through such channels. Utilizing two-phase flow simulation, all such parameters can be adjusted to quickly obtain large amounts of data on how these parameters affect the capillary flow.

The initial objective was to execute simulations that mirrored the hourglass concept delineated in chapter 4, incorporating liquid volumes with two concurrent air interfaces. Regrettably, the generation of convergent results for such models was unsuccessful. Nonetheless, simulations with only a single-phase interface, utilizing a water inlet at one end of the channel and an outlet at the other, can yield considerable insights into how various material and geometric parameters influence capillary flow.

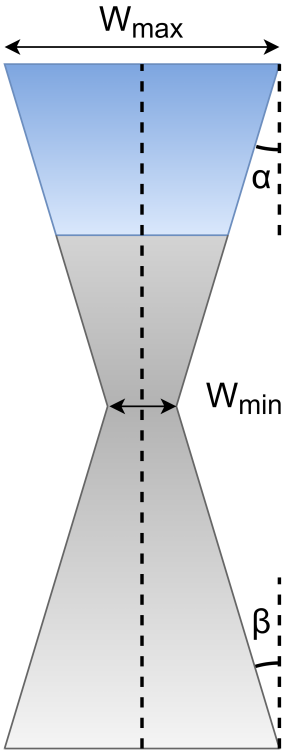

Figure 5.9: Simulation geometry for the hourglass parametric study. This 2D geometry is extruded to a depth d

The parameters subject to systematic variation in the numerical parametric study are enumerated below. Accompanying each parameter is a concise explanation detailing its significance and anticipated influence on the study.

- **Contact Angles θ_W and θ_d**
  Description: Contact angles represent the angles at which the fluid interface meets

the material's surface.
Goal: To assess how varying contact angles affect the pressure, flow, and equilibrium.
Impact: Lower contact angles will increase the capillary forces and result in curvatures with lower radii and higher pressures.

- **Slope angles α and β**
  Description: The angle between the hourglass walls and the z-axis. α represents the angle for the upper part of the geometry, while β represents the lower part.
  Goal: To investigate if the slope, in combination with the contact angle, results in the liquid behavior predicted in chapter 4.
  Impact: Increased slope angles should accelerate the flow in the converging section of the hourglass geometry and decelerate it in the diverging section.

- **Gravity g_z**
  Description: The gravitational acceleration in the z-direction. It can be positive (upwards), negative (downwards), or turned off.
  Goal: To examine how gravity will affect the curvature and flow speed.
  Impact: On the one hand, gravity will exert a force on the liquid volume along the gravity force direction. On the other hand, as discussed briefly in section 4.4, it will influence the curvature, thereby altering the capillary forces. The direction of this force depends on a combination of the contact angle and the slope angle.

- **Depth d**
  Description: The length out of the plane dimension of the channel.
  Goal: To assess the effect of the ratio between channel width and depth.
  Impact: Increased depth leads to the principal radius due to θ_d increasing. This should lower the total capillary forces.

- **Width at the transition point W_{min}**
  Description: Channel width at the narrowest point of the hourglass geometry.
  Goal: To examine how narrow the transition point can be without impacting the flow in a significant way.
  Impact: A narrow transition point will lead to a head loss, slowing the flow.

For the evaluation of contact angle, gravitational acceleration, slope angles, and channel depth, the geometry is governed by the input volume, which is appropriated from the funnel used during validation. This enables comparisons with alternate geometries while maintaining consistency in other parameters. Additionally, the ratio between the narrowest and widest points of the hourglass is maintained at a constant of 4 to simplify geometric calculations.

For subsequent examinations focused on slope angle β and width at the transition point $W_{\min}$, the geometry is reconstructed to allow precise control over these parameters while keeping other parameters unchanged. In these studies, the height of the hourglass and the initial height of the water are also regulated to ensure more uniform and consistent results.

5.4 Results and Discussion

This section delves into the numerical results and critically analyze the outcomes of the parameter study conducted on the hourglass geometry, as elucidated in section 5.3. The study entails a systematic variation of several key parameters, including contact angles ($\theta_W = \theta_d$), the slope angles alpha α and beta β, gravity g_z, the depth of the channel and the minimum width of the hourglass W_{min}.

Figures 5.10 present the water volume fraction in a series of snapshots from three representative simulations at distinct time steps. These visuals serve as a pedagogical tool to interpret various fluid dynamics phenomena that consistently manifest across the simulation results.

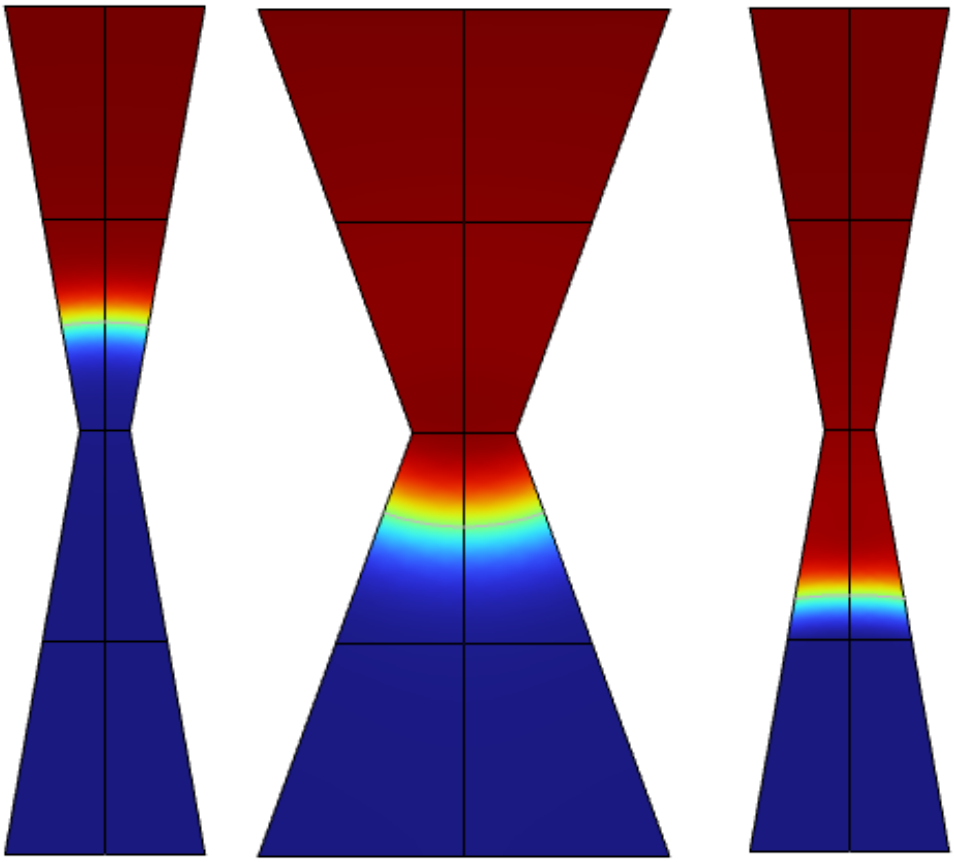

(a) (b) (c)

Figure 5.10: The volume fraction under the hourglass simulation. 5.10a has contact angle of 90° and α of 10°. 5.10b has contact angle of 90° and α of 20°. 5.10c has contact angle of 70° and α of 10°. Note that W_{min} changes with α since this was not an input parameter.

In Figure 5.10a, the liquid hasn't reached the transition point within the hourglass. Here, surface tension plays a pivotal role by inducing curvature in the fluid-air interface. This curvature, governed by the Young-Laplace equation, results in a pressure differential across the interface, propelling the liquid downward.

Proceeding to Figure 5.10b, the fluid has traversed past the transition point. Interestingly, the change in the wall slope at this junction prompts an opposite curvature in the fluid interface. Consequently, the pressure differential drives the fluid upward, counteracting the initial downward acceleration.

Lastly, Figure 5.10c portrays a scenario where the fluid has surpassed the transition point, akin to the previous case. However, the resultant curvature causes the fluid to accelerate downward due to a different set of parameters.

This triad of cases encapsulates the intricate interplay between geometrical constraints, surface tension, and pressure differentials in dictating the fluid's motion within the hourglass geometry. Subsequent subsections will provide a more detailed discussion of how parameter variations like contact angles, slope angles, gravity, depth, and minimum width influence these mechanisms.

5.4.1 Angles: Contact angle, α and β

Figure 5.11 shows the evolution of the phase interface surface in the centerline for different slope angles (α), where the contact angle is set to 90°. The interface surface is accelerating toward the transition point in the early stages. A crucial observation is that the acceleration is more distinct for higher values of α.

This observation is consistent with the previously established theory. Specifically, for regions above the transition point, where $\theta - \alpha$ is lower than 90°, the curvature of the interface is concave. This curvature gives rise to a pressure difference which propels the fluid downward. The magnitude of this pressure difference, and hence the acceleration, is directly proportional to the deviation of $\theta - \alpha$ from 90°. The following relation between the capillary force and angles above the transition point can be derived from the boundary condition (3.25) and the Young-Laplace equation (3.9).

$$F_{cap} \propto \Delta p \propto \theta - \alpha - 90^\circ \tag{5.5}$$

Under the transition point, the relation between the capillary force and angles is

$$F_{cap} \propto \Delta p \propto \theta + \beta - 90^\circ \tag{5.6}$$

As the fluid interface crosses the transition point, an inflection occurs in the surface height. This inflection is where the surface changes from decelerating to accelerating toward the transition point. Intriguingly, regardless of the initial values of α, the fluid interface converges to an equilibrium state with the interface surface at the transition point. This behavior is coherent with the earlier discussed relation between angles and capillary forces. Below the transition point, a convex curvature is observed if $\theta+\alpha$ is above 90°. With a contact angle of 90° and divergent walls, the curvature is always convex in the absence of gravity. This leads the interface to consistently accelerate back toward the transition point, thus substantiating the analytical expectation of the interface settling at the transition point as the equilibrium state.

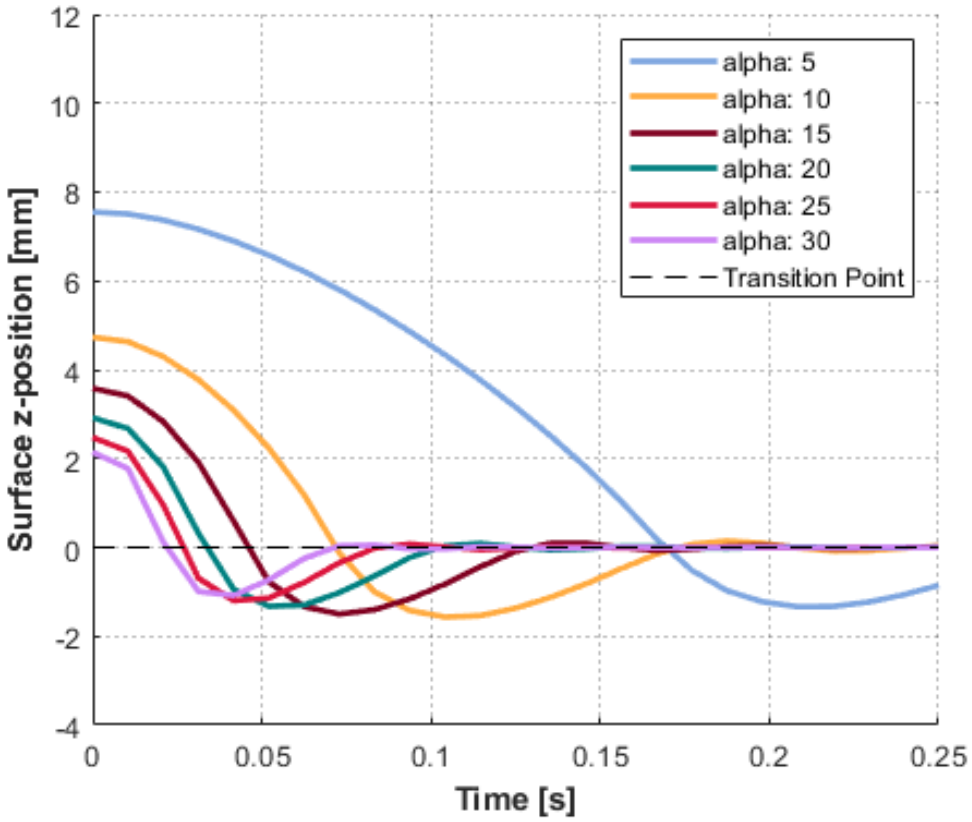

Figure 5.11: The phase interface in the centerline for different $\alpha = \beta$, The depth is1 mm, the contact angle is 90°, and no gravity is applied. The phase interface surface is obtained by finding where the phase-field parameter (Φ) is 0 by interpolation. The surface starts at different levels since the start position depends on α.

However, it's essential to examine specific aspects of this setup critically. First, the fluid interface commences at different heights based on the value of α. Furthermore, the height of the hourglass itself varies with α, and the minimum width, W_{min}, is not held constant. These variations could introduce confounding factors in understanding the sole impact of the slope angles on the fluid dynamics. It might be beneficial to conduct further simulations with controlled initial positions and consistent hourglass dimensions to more accurately isolate and understand the implications of varying slope angles.

Figure 5.12 illustrates the evolution of the phase interface for varying contact angles with α of 10°. Notably, the contact angles for the side and out-of-plane walls are consistent ($\theta_W = \theta_d$). The initial observation reveals a clear trend: a lower contact angle results in a faster acceleration towards the transition point. This acceleration can be attributed to the capillary forces, which increase as the contact angle decreases. Conversely, the liquid decelerates to a greater extent for a higher contact angle after crossing the transition point.

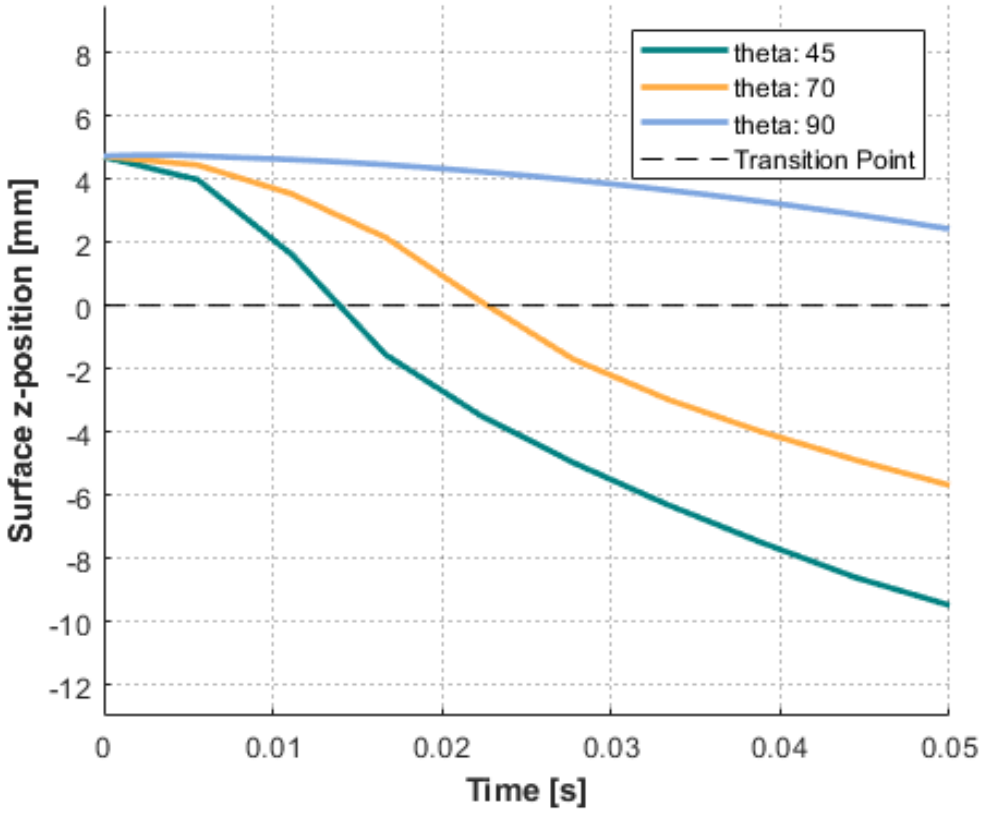

Figure 5.12: The phase interface in the centerline for different contact angles 45°, 70°, and 90° applied to an hourglass geometry with $\alpha = 10°$ and no gravity applied. The phase interface surface is obtained by finding where the phase-field parameter (Φ) is 0 by interpolation.

In contrast to 90°, the interface for 70° does not return to the transition point but continues to descend along the hourglass shape. This behavior aligns with the theoretical expectation since, for this configuration, $\theta + \alpha$ equals 80°, less than 90°. Thus, the capillary force is still directed downwards, allowing the interface to keep moving in the same direction.

However, an interesting observation is that the difference between the 45° and 70° cases after the transition point is not significantly high. A possible explanation for this might be that the change in the cross-sectional area of the hourglass plays a more substantial role in influencing the velocity of the liquid surface compared to the variation in contact angles.

Figure 5.13 portrays similar phenomena, albeit with α at 20°. The patterns largely mirror those seen in Figure 5.12, with lower contact angles accelerating more rapidly toward the transition point. Comparing the two figures shows that a larger α leads to faster acceleration, consistent with observations from Figure 5.11.

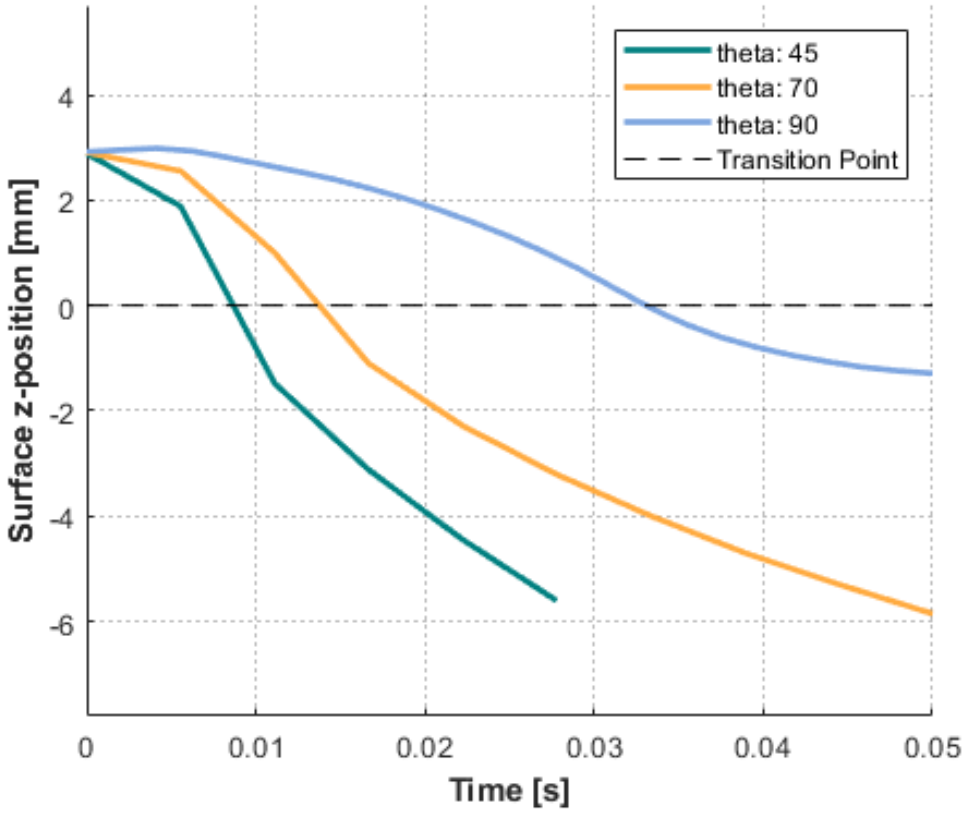

Figure 5.13: The phase interface in the centerline for different contact angles 45°, 70°, and 90° applied to an hourglass geometry with $\alpha = 20°$, depth 1 mm and no gravity applied. The phase interface surface is obtained by finding where the phase-field parameter (Φ) is 0 by interpolation.

Figure 5.14 shows the surface progression for varying β, representing the slope angle below the transition point. In contrast to previous simulations, β is varied here while α is held constant at 10°. Moreover, gravity is incorporated into the simulation, and gravity's impact will be analyzed in the next subsection. It can be observed from Figure 5.14 that the fluid decelerates more with a higher contact angle. This outcome is in alignment with earlier observations. Theoretically, the fluid interface would reverse its direction without gravity and gravitate back towards the transition point when β exceeds 20°. However, such a phenomenon necessitates extended simulation timeframes to allow the fluid interface sufficient time to reverse and accelerate back.

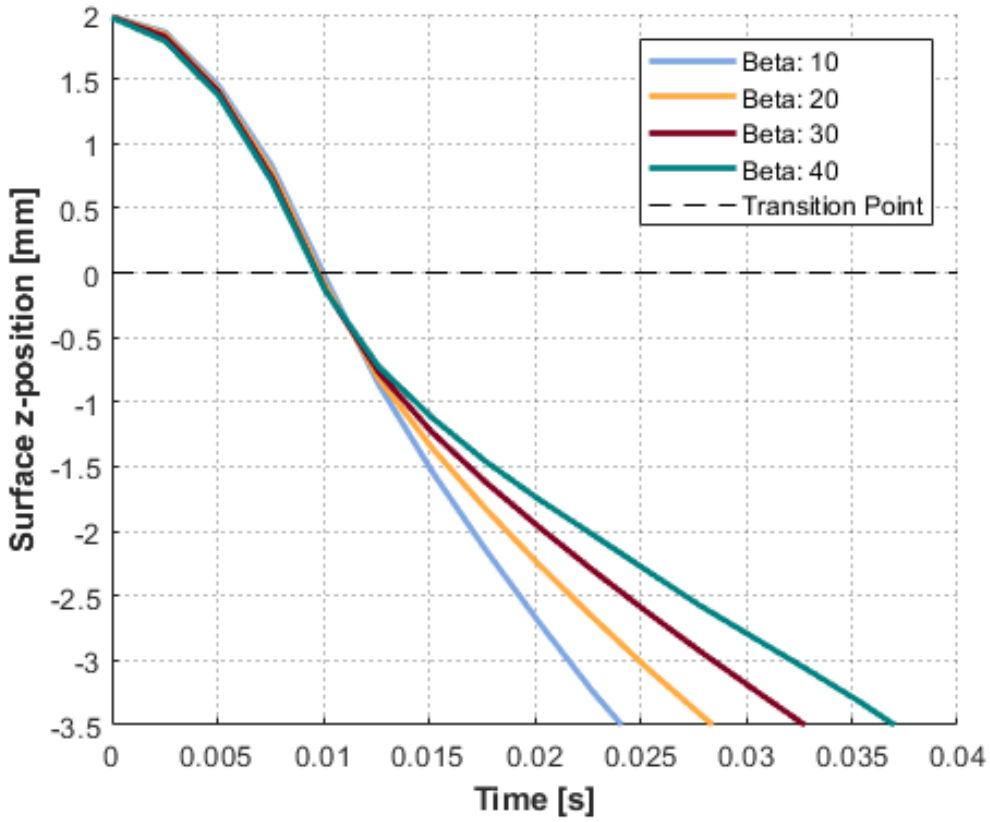

Figure 5.14: The phase interface in the centerline for varying β, The depth is1 mm, the contact angle is 70°, α is 10° and the gravity is pointing down. The phase interface surface is obtained by finding where the phase-field parameter (Φ) is 0 by interpolation.

The simulations and analyses conducted in this subsection have yielded some critical insights into the fluid dynamics within an hourglass-shaped channel and how these dynamics are influenced by various angles - contact angle, α, and β. The main observations and takeaways are as follows:

- Lower contact angles and higher α result in higher downward acceleration of the water above the transition point.

- Higher contact angles and higher α/β result in lower downward or higher upward acceleration of the water below the transition point.

While these observations generally align with the established theoretical framework, it is imperative to acknowledge that the simulations carry certain confounding factors that limit the robustness of the numerical results. For instance, the fluid interface starts at different heights depending on the value of α, and the hourglass dimensions, such as minimum width, are not held constant across different simulations. These variations may obscure the isolated effects of the slope angles on the fluid dynamics. To develop a more comprehensive and confident understanding, executing additional simulations that meticulously control these factors would be beneficial. Furthermore, long-term simulations may be necessary to fully observe phenomena such as the fluid interface returning to the

transition point under certain conditions.

5.4.2 Gravity and depth

The impact of gravity force on capillary flow is intriguing because it influences the liquid in two ways. On the one hand, it accelerates the liquid due to the mass of the liquid. Several studies have been conducted on how the capillary rise is influenced by low-gravity or no-gravity environments [66, 67]. They report that liquid rises faster and higher when gravity is decreased or completely removed. This finding agrees with Jurin's law (3.18).

On the other hand, gravity also influences the surface curvature inside a capillary channel. Naydich et al. [68] studied this phenomenon, showing how the principal radius of the surface curvature considerably decreased in a no-gravity environment. Such a reduction in the principal radius subsequentially lead to a reduction in capillary force.

These two effects, induced by gravity, have opposite effects on the liquid in a capillary channel. For a large volume of liquid, the mass of the liquid dominates. However, for low volumes, this is not necessarily the case. Figures 5.15 and 5.16 display the effect of gravity in the hourglass channel by comparing three scenarios. For the case of (-g), the gravity vector points in the same direction as the flow, while the opposite is true for the case of (+g).

For both contact angles, the same trend is apparent. The simulation where the gravity is directed opposite to the flow direction (+g) accelerates faster than the other two simulations. All simulations decelerate once the surface interface reaches the diverging part of the channel. Here the effect of the gravitational acceleration becomes visible, with (-g) decelerating more slowly than the other simulations.

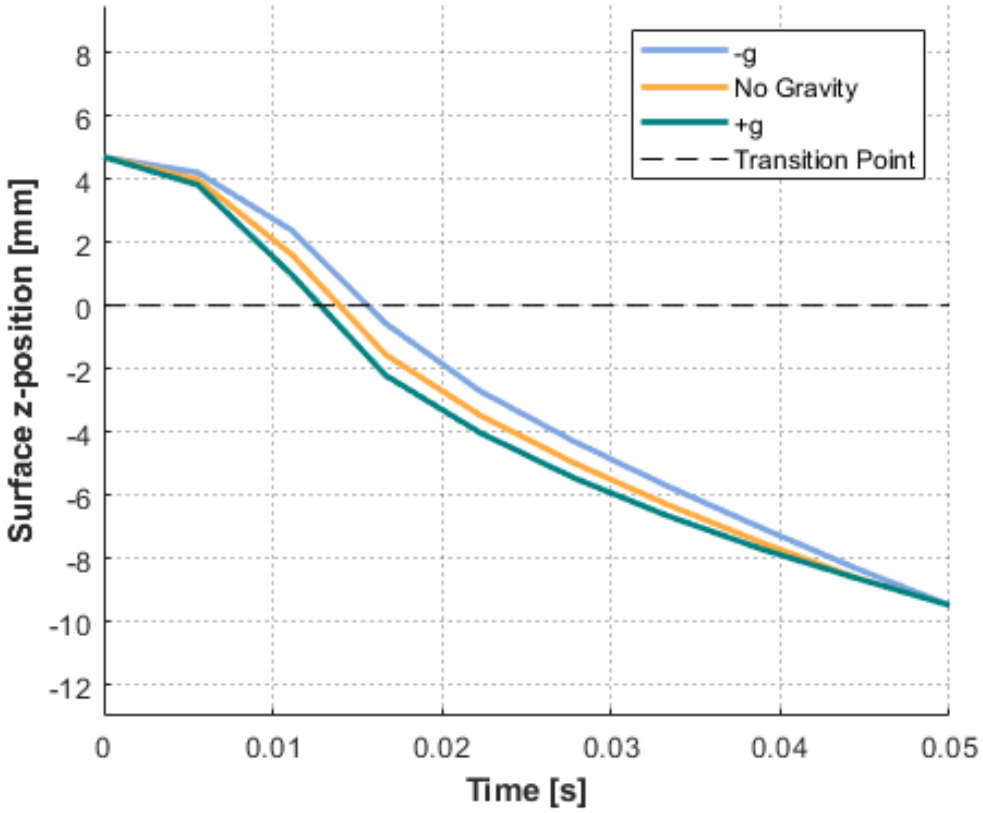

Figure 5.15: The phase interface in the centerline for affected by gravity, The depth is 1 mm, the contact angle is 45°, and $\alpha = 10°$. The phase interface surface is obtained by finding where the phase-field parameter (Φ) is 0 by interpolation.

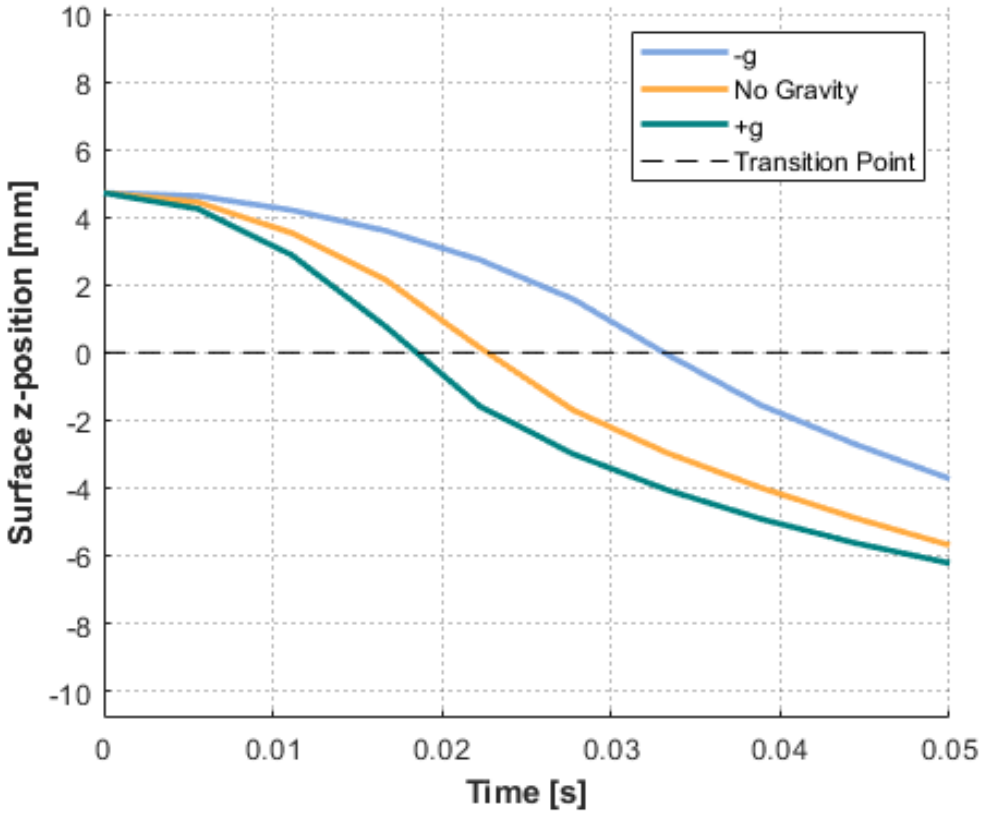

Figure 5.16: The phase interface in the centerline for affected by gravity, The depth is 1 mm, the contact angle is 70°, and $\alpha = 10°$. The phase interface surface is obtained by finding where the phase-field parameter (Φ) is 0 by interpolation.

A further observation of note is that the influence of gravity diminishes significantly in scenarios with low contact angles. At the same time, simulations run with high contact angles are significantly affected by it. This suggests that in cases of high hydrophilicity, capillary forces dominate over gravity, reducing the effect of gravitational forces to near insignificance.

However, on closer investigation, it becomes clear that the discrepancy in acceleration between the gravity cases is considerably impacted by the first few time steps, where the contact angles and curvatures are created. Figure 5.17 showcases the positions of the surface interface lines 0.003 seconds into the simulation for $\theta = 70°$. While there is no noticeable difference in surface curvature, the simulation for (+g) is ahead of the simulation for (-g). It appears that the rate at which the surface interface develops its curvature at the simulation's beginning depends on the gravity force's direction, with (+g) allowing for the fastest curvature development.

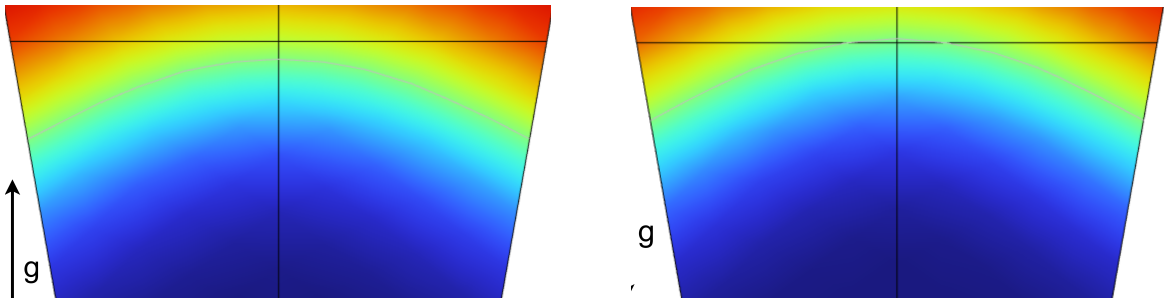

(a) (b)

Figure 5.17: Surface curvature postition of $\theta = 70°$ after 0.003 seconds for (a) +g and (b) -g. The thin horizontal line indicates the starting position of the water

The generation of surface curvature in these simulations starts from an initially flat water surface, a factor that introduces a degree of deviation from real-world scenarios. In reality, the liquid-gas interface invariably possesses some curvature, provided that the aggregate of the slope angle, α, and the contact angle of the channel wall do not strictly equal 90°.

The variation in the time needed for developing surface curvature introduces significant uncertainties in the gravity parametric study. A potential improvement of these simulations could be incorporating an estimated initial surface curvature into the model of the initial water volume. This might minimize the time required for the initial formation of curvature, consequently providing a consistent starting point for the investigations into all three scenarios. However, this hypothesis was not investigated further due to the time constraints of this project.

The effects of gravity forces on capillary flow within a channel geometry of $\theta = 70°$ and $\alpha = 10°$ but with a depth $d = 0.5$ mm were also studied. The impact is demonstrated in Figure 5.18. A comparative analysis between these results and those from an equivalent channel with depth $d = 1$ mm, displayed in figure 5.16, reveals a significantly reduced influence of gravity forces in the case of $d = 0.5$ mm. This observation aligns well with capillary action theory, which proposes that capillary force magnitude is inversely proportional to the channel cross-sectional area—increasing as this area diminishes.

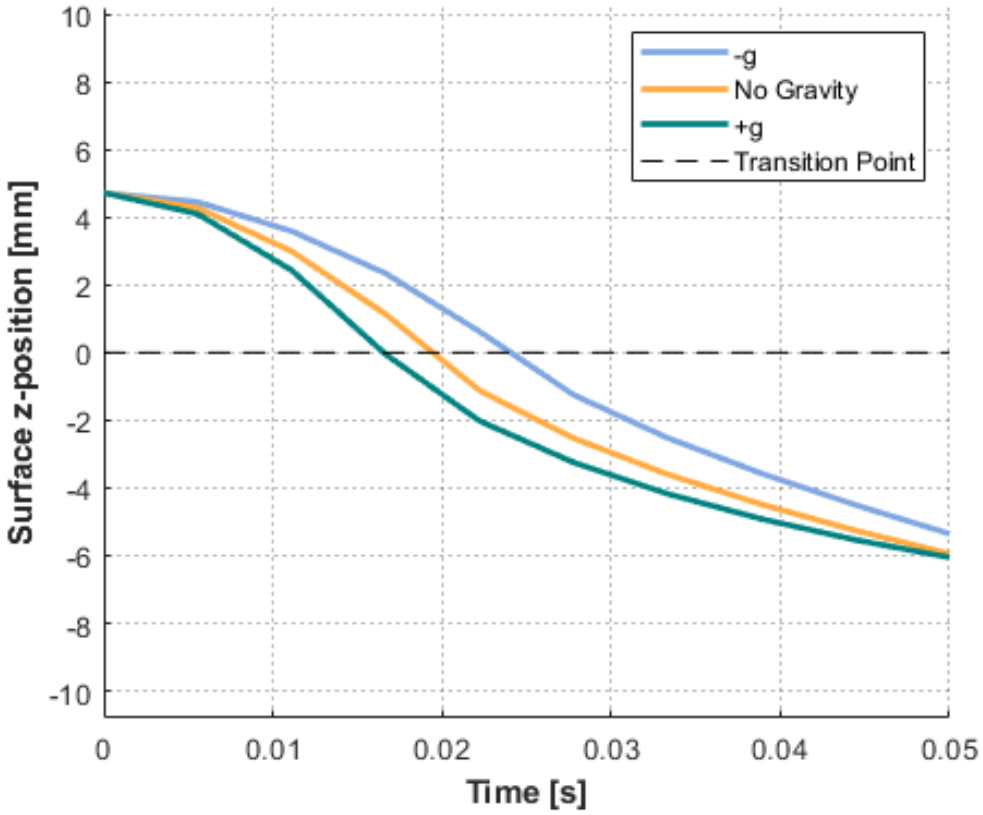

Figure 5.18: The phase interface in the centerline for affected by gravity, The depth is 0.5 mm, the contact angle is 70°, and $\alpha = 10°$. The phase interface surface is obtained by finding where the phase-field parameter (Φ) is 0 by interpolation.

5.4.3 Width W_{min} at the transition point

The last parameter to be investigated is the hourglass geometry's minimum width W_{min}. The geometries and pressure contours of two of these simulations are illustrated in figure 5.19 and 5.20 with W_{min} of respectively 0.25 mm and 2.0 mm. A consistent set of parameters, including a contact angle of 70°, slope angles α and β of 20°, an hourglass height of 8 mm, and an initial water surface height of 2 mm was employed to isolate the effects of W_{min}. The simulations incorporate gravity to emulate real-world scenarios better. However, one must exercise caution when interpreting these results, as the inclusion of gravity complicates the analysis. In an ideal scenario with ample resources, additional simulations with and without gravity should be conducted for a more comprehensive understanding.

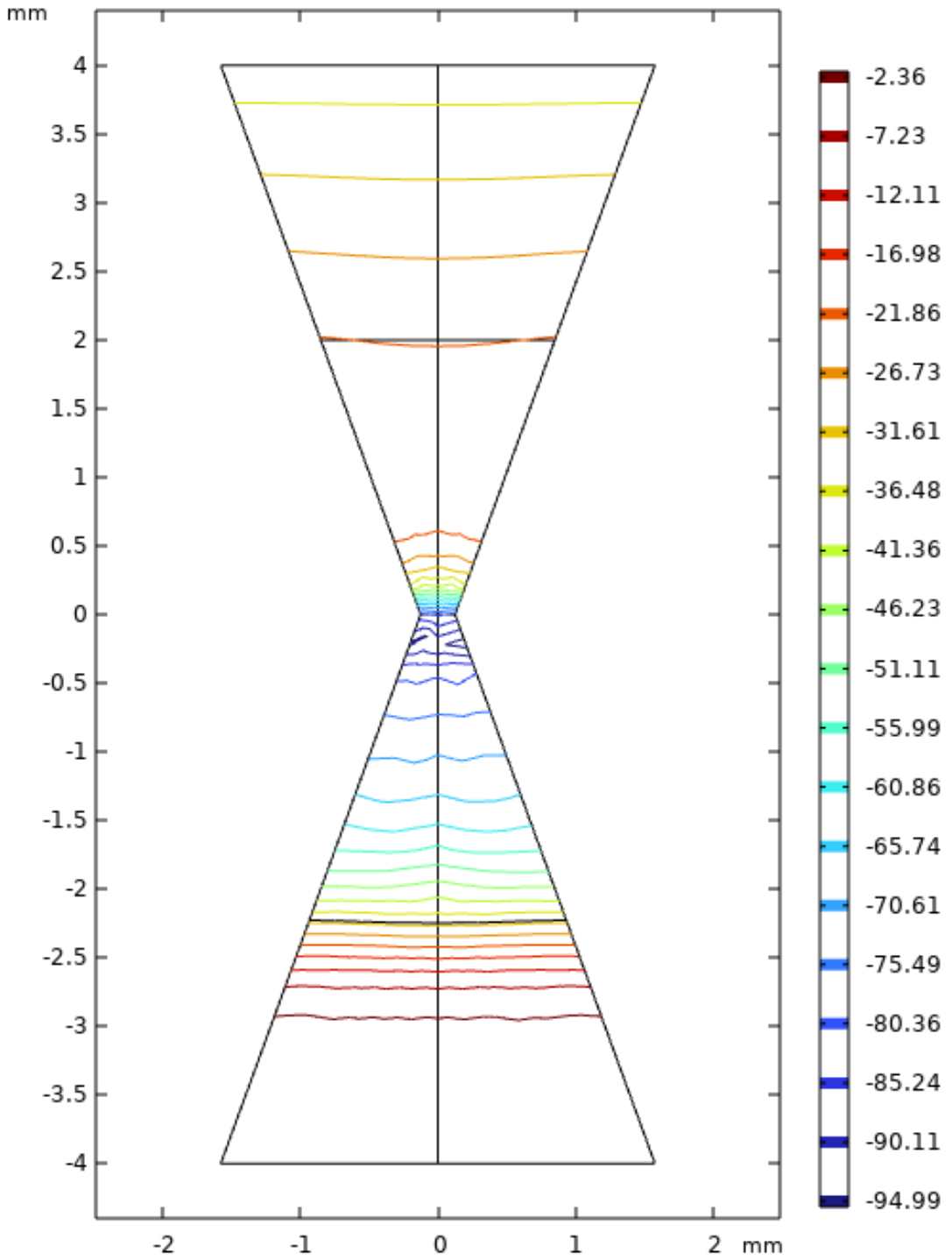

Figure 5.19: The pressure contour-plot in Pa for hourglass with W_{min} of 0.25 mm, the contact angle of 70°, slope angle $\alpha = \beta$ of 20°, depth 1 mm, and gravity pointing downward. The reference pressure is in the bottom center of the hourglass. The upper black line at 2 mm is the starting position of the water surface. The current water surface is the lower black line at -2.25 mm.

Figures 5.19 and 5.20 depict the water surface almost perfectly horizontal at the height of -2.25 mm. At this moment, capillary forces are minimal. Without gravity, the water surface would theoretically be exactly horizontal as $\theta + \beta = 90°$. This configuration

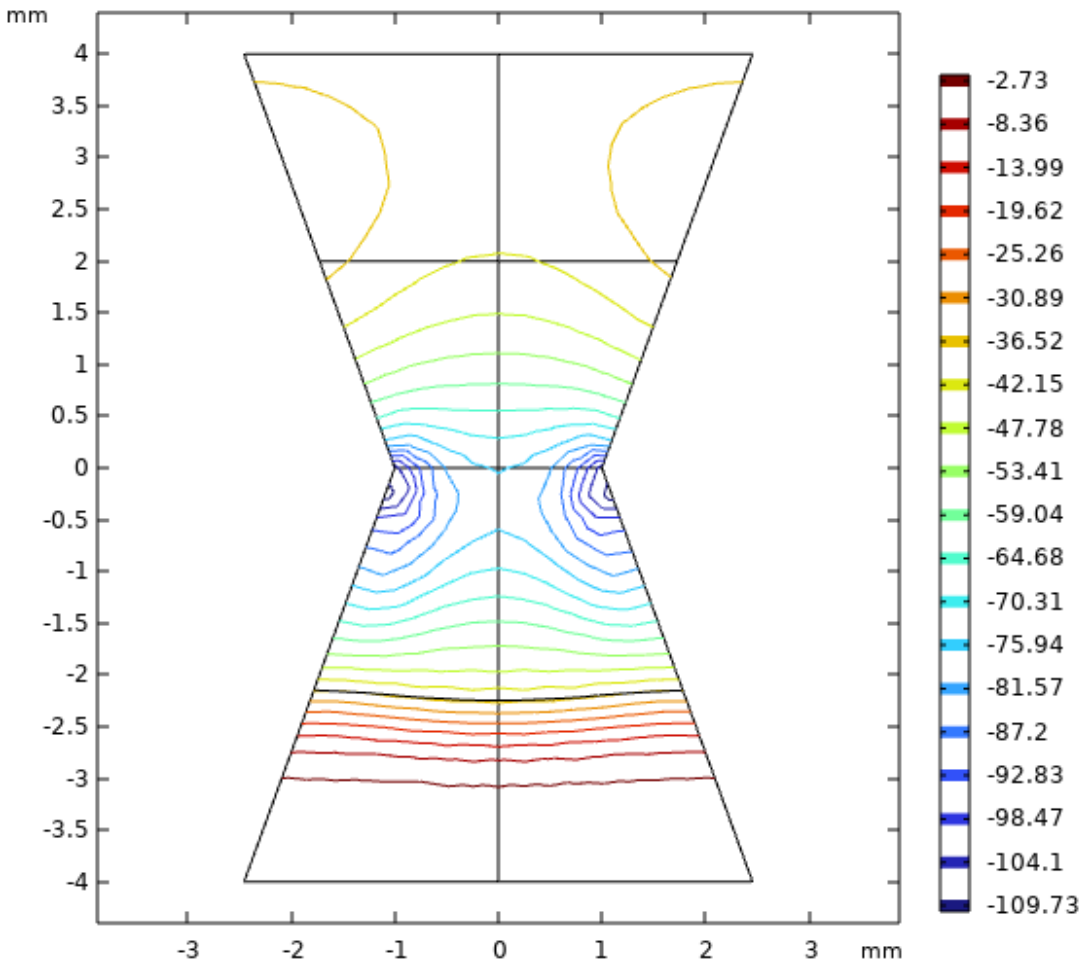

Figure 5.20: The pressure contour-plot in Pa for hourglass with W_{min} of 2.0 mm, the contact angle of 70°, slope angle $\alpha = \beta$ of 20°, depth 1 mm, and gravity pointing downward. The reference pressure is in the bottom center of the hourglass. The upper black line at 2 mm is the starting position of the water surface. The current water surface is the lower black line at -2.25 mm.

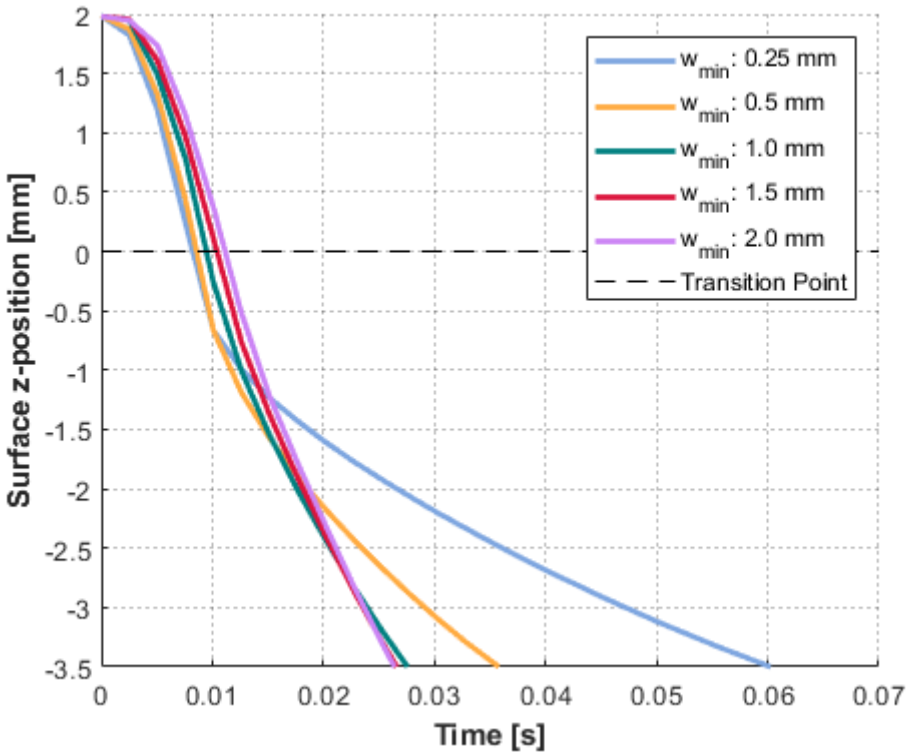

Figure 5.21: The phase interface surface in the centerline for varying W_{min}. The depth is 1 mm, the contact angle is 70°, and the gravity is pointing down. The phase interface surface is obtained by finding where the phase-field parameter (Φ) is 0 by interpolation. Additional figures for the W_{min} parameter study are in appendix A.3.

provides a basis to examine the sole effects of W_{min}.

Figure 5.21 shows the interface surface over time for varying values of W_{min}. A prominent observation from the figure is the pronounced acceleration of the interface toward the transition point as W_{min} decreases. Subsequently, there is a notable deceleration post the transition point for the lower values of W_{min}.

The acceleration before the transition point can be attributed to a couple of mechanisms. First, as W_{min} decreases, the relative reduction in cross-sectional area is more significant, which, according to the principle of continuity, necessitates a higher flow velocity to conserve the volumetric flow rate. Second, the role of capillary forces becomes increasingly pronounced for smaller cross-sections, contributing to acceleration.

The deacceleration after the transition point can be attributed to the conservation of volumetric flow rate demands a reduction in velocity as the cross-sectional area expands. Additionally, the head loss incurred due to the sudden expansion in the channel is critical. This head loss is more significant for a smaller W_{min}, where the constriction is more pronounced. The pressure contour plots in figure 5.19 and 5.20 exemplify this, demonstrating a pressure loss around the minimum width.

The total head loss across the geometry is represented by equation (5.7), which

encompasses both frictional and geometric losses [69].

$$h_{L,total} = \sum_i \frac{f_i L_i}{D_i} \frac{V_i^2}{2g} + \sum_j K_{L,j} \frac{V_j^2}{2g} \tag{5.7}$$

Here, K_L denotes the head loss coefficient, f represents the Darcy friction factor, L is the channel length, D is the hydraulic diameter, and V is the average inlet velocity. The head loss is intricately related to the pressure drops through the relationship $\Delta p = h_{L,total}\rho g$. The geometry influences the head loss coefficient, K_L, and increases with the ratio of the maximum to minimum cross-sectional area. Moreover, the head loss is more considerable for expansions than contractions for circular tubes; this could be analogous to the hourglass geometry.

Estimating the head loss coefficient for an hourglass-shaped channel is non-trivial and may not have readily available empirical correlations. Computational simulations tailored to the specific geometry can provide insights into the head loss coefficients.

Furthermore, equation (5.7) implies a dependency of the head loss on the square of the fluid velocity. As can be discerned from figure 5.21, the fluid velocity increases with W_{min} at a given position (e.g., $-2.25\,\mathrm{mm}$), which has implications for the head loss. The interplay between the head loss coefficient and the fluid velocity may account for the observed trends, particularly the similarity among the cases with larger W_{min}.

In summary, a lower W_{min} results in a more considerable reduction in flow velocity following the transition point, attributed to increased head losses. However, this effect becomes marginal for values of W_{min} above $1\,\mathrm{mm}$.

6 Experimental Study

Having detailed the theoretical basis for the hourglass concept in chapter 4, it is sensible to proceed with experimentation to verify the theoretical assumptions and uncover aspects overlooked in previous considerations.

This chapter describes the experimental setup, designed to provide empirical evidence supporting the theoretical predictions. Through these experiments, The aim is to bridge the gap between theory and reality, observing firsthand how the fluid behaves in the hourglass design, specifically during the attainment of the first equilibrium state. Following this, the experiment results are presented and discussed.

6.1 Experimental Setup

The experimental procedure involves capturing videos of specified water volumes being introduced into self-fabricated cartridges, mimicking the size constraints of the Inflammacheck® scenario, and featuring the proposed hourglass channel shape. Following this, the actual geometries and volume fractions obtained from the experiments will be compared to the predictions generated by the analytical model. The tests will also be executed where geometric parameters are varied systematically to assess the concept's robustness.

6.1.1 Hourglass cartridge

To fabricate suitable testing cartridges, several crucial requirements must be met. Primarily, the cartridges must be constructed from hydrophilic materials to ensure that capillary forces behave in accordance with the theoretical model. Additionally, the surfaces of the channels should exhibit a high degree of smoothness to promote consistent and efficient wetting. This requirement rule additive manufacturing techniques as they tend to generate surfaces characterized by mesostructure, a feature incompatible with homogeneous wetting. Moreover, it is essential to ensure that the channel is hermetically sealed to confine the water movement exclusively along the channel's length, thereby eliminating the possibility of unintended leakage or bypass routes.

The selected approach to cartridge fabrication involves a layer-by-layer assembly process, with each layer crafted through laser cutting technology. A complete cartridge comprises three distinct layers: a back plate, a front plate, and an intermediary layer responsible for constructing the channel sidewalls. Due to its desirable properties, acrylic plexiglass (PMMA) is utilized for the front and back plates. The sidewall layer is crafted from a "sandwich structure" comprising multiple adhesive film layers. Data sheets for the film can be found in appendix C.

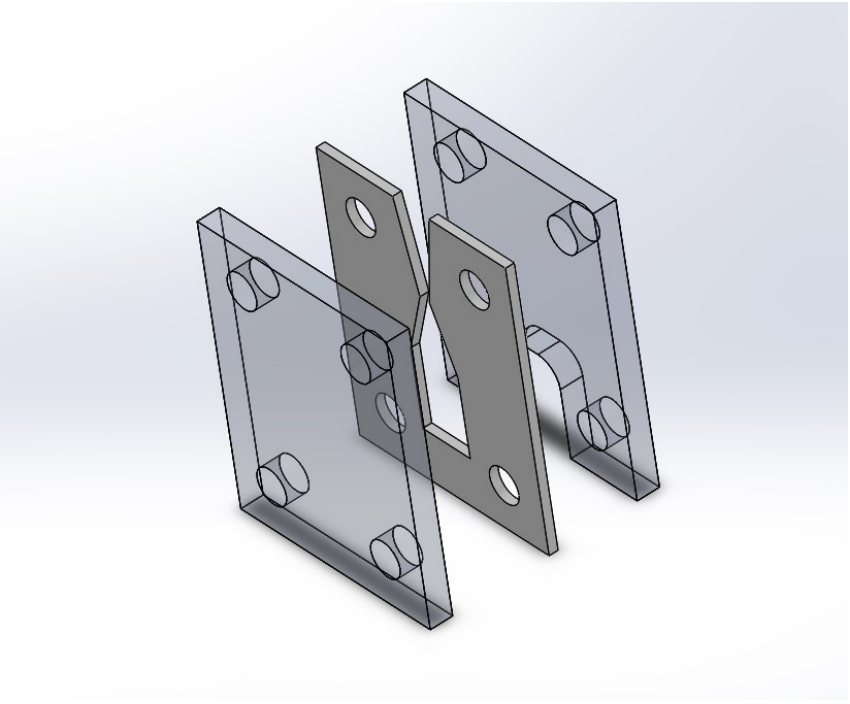

Figure 6.1: Exploded view of hourglass cartridge assembly

PMMA, generally considered hydrophilic, demonstrates contact angles around 70 degrees according to multiple literature sources [70, 71]. However, a significant unknown in the experiments lies with the hydrophilic properties of the self-fabricated sandwich structure, for which no specific data is available. This presents a considerable variable that might influence the results. The choice to proceed with this material was primarily due to its adjustable thickness and unique characteristic of having a double-sided adhesive layer, a

property not found in the other materials available to us. Another important requirement for the test cartridge is that both liquid-gas surfaces are exposed to the ambient air, ensuring no pressure difference between them.

Figure 6.2: Schematic of the hourglass cartridge channel cross-section

The three layers are manufactured separately through laser cutting and assembled using a 3D printed assembly jig, as shown in figure 6.3.

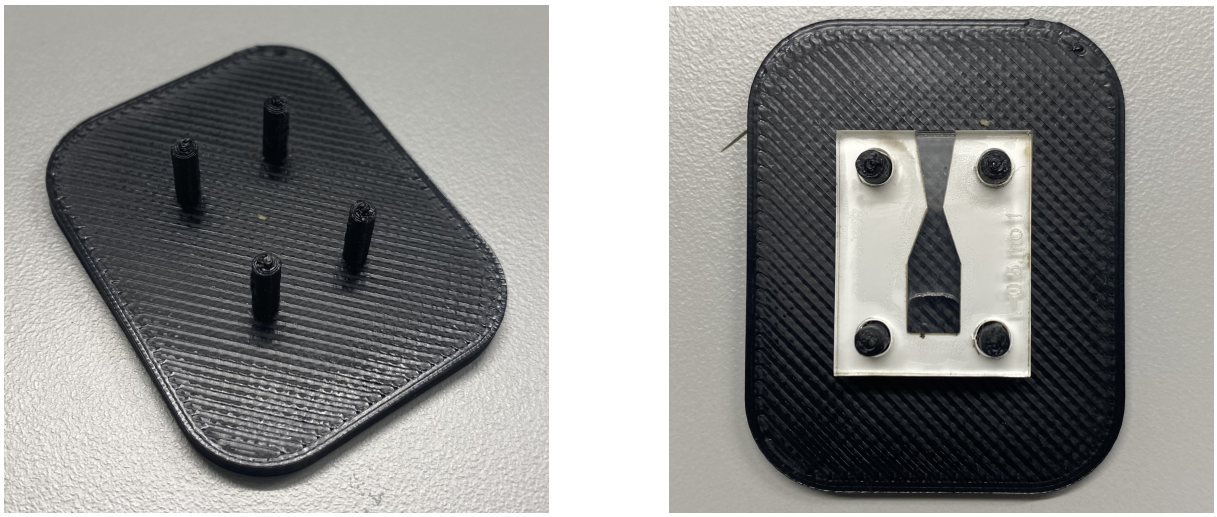

Figure 6.3: 3D printed mounting jig for cartridge assembly

The design of the cartridge channel dimensions is informed by the theoretical model established in chapter 4. The channel slope angles are $\alpha = 10°$ and $\beta = 20°$. In accordance with the reported material properties of PMMA, the contact angle is assumed to be $\theta_d = \theta_{PMMA} = 70°$. Furthermore, the contact angle θ_W is assigned a value of 69.9° — the highest permissible value under the theoretical model constraints ($\theta_W + \beta < 90°$). Three distinct channel designs are generated, each differing in width at the transition point, W_{min}. The variations in W_{min} are set to 1 mm, 1.5 mm, and 2 mm, offering a range of experiment parameters. The input parameters are summarized in table 6.1, while figures 6.4-6.6 and tables 6.2-6.4 present the resulting volume geometries and key data.

Table 6.1: Input parameters for cartridge design

Parameters	V	d	x_{min}	α	β	θ_W	θ_d
Values	20 μL	1.0 mm	0.5/0.75/1.0 mm	10°	20°	69.9°	70°

W_{min} = 1 mm:

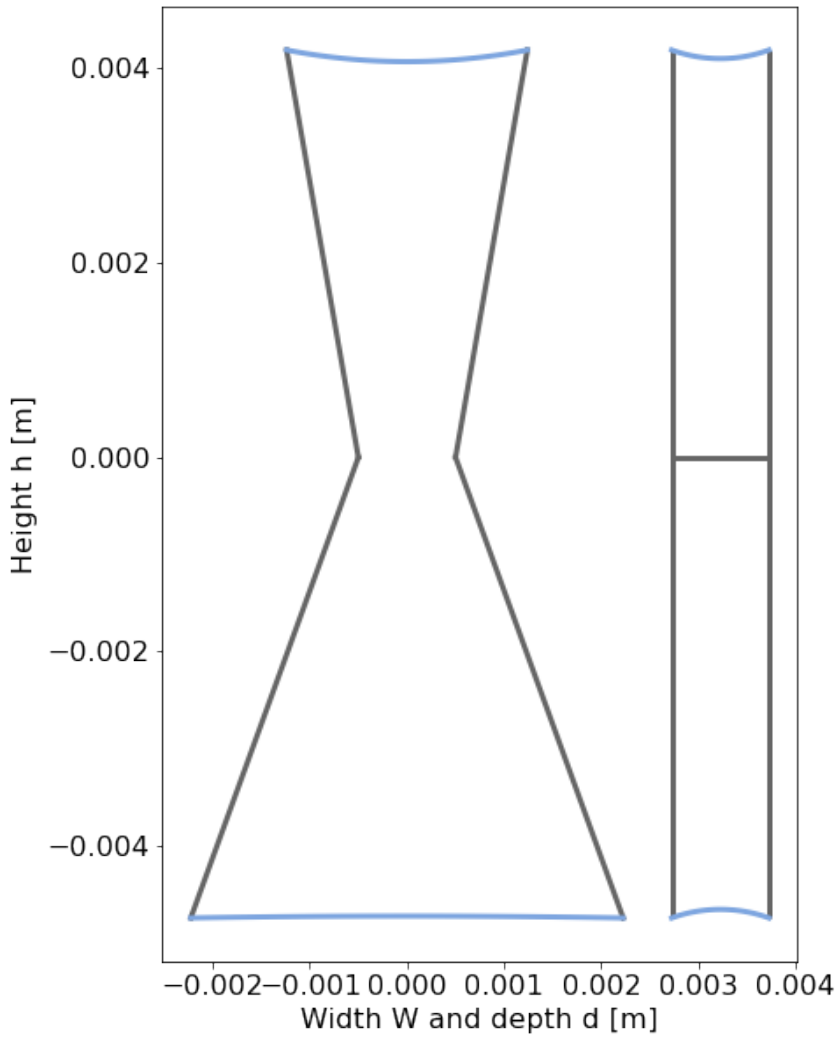

Figure 6.4: Resulting equilibrium state geometry for W_{min} = 1 mm

Table 6.2: Output data for W_{min} = 1 mm

Parameter	Value
W_1	2.47 mm
W_2	4.45 mm
W_{min}	1.00 mm
h_1	4.19 mm
h_2	4.74 mm
Volume fraction	35.5 %

W_{min} = 1.5 mm:

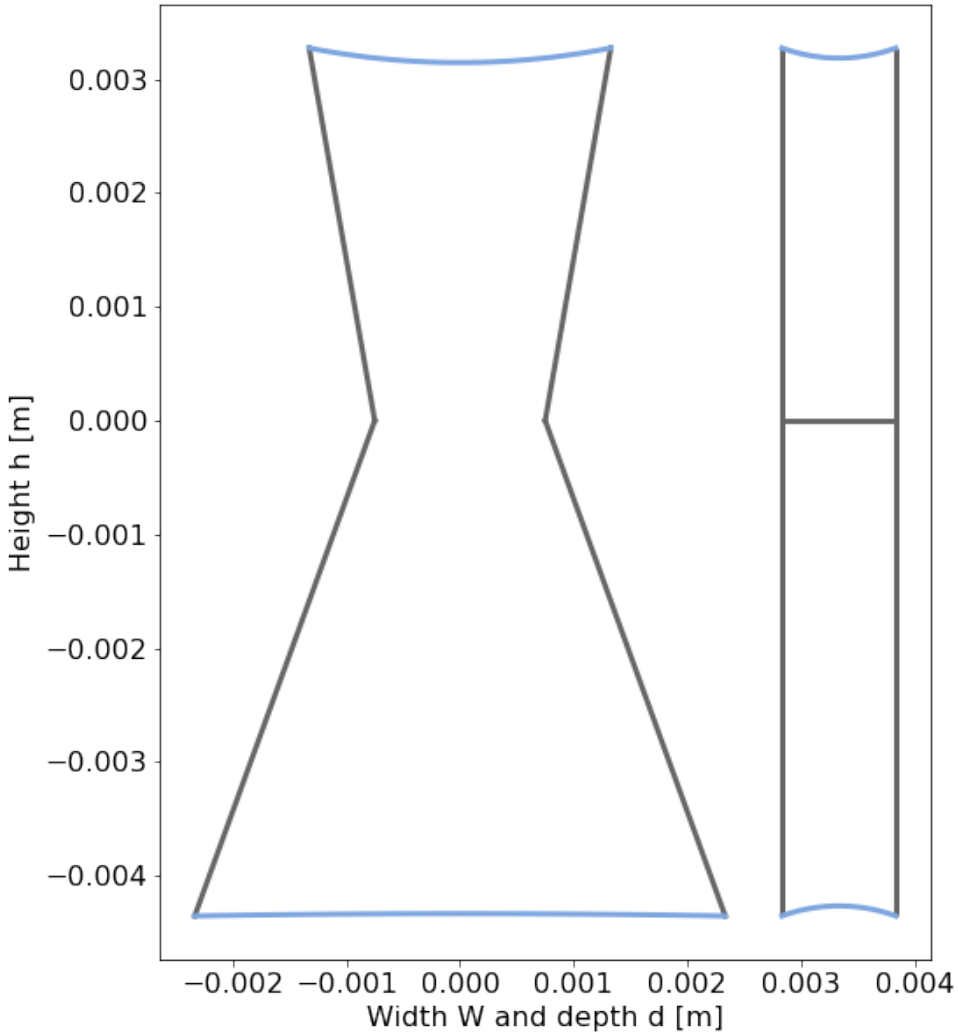

Figure 6.5: Resulting equilibrium state geometry for W_{min} = 1.5 mm

Table 6.3: Output data for W_{min} = 1.5 mm

Parameter	Value
W_1	2.65 mm
W_2	4.67 mm
W_{min}	1.50 mm
h_1	3.27 mm
h_2	4.35 mm
Volume fraction	33.0 %

W_{min} = 2 mm:

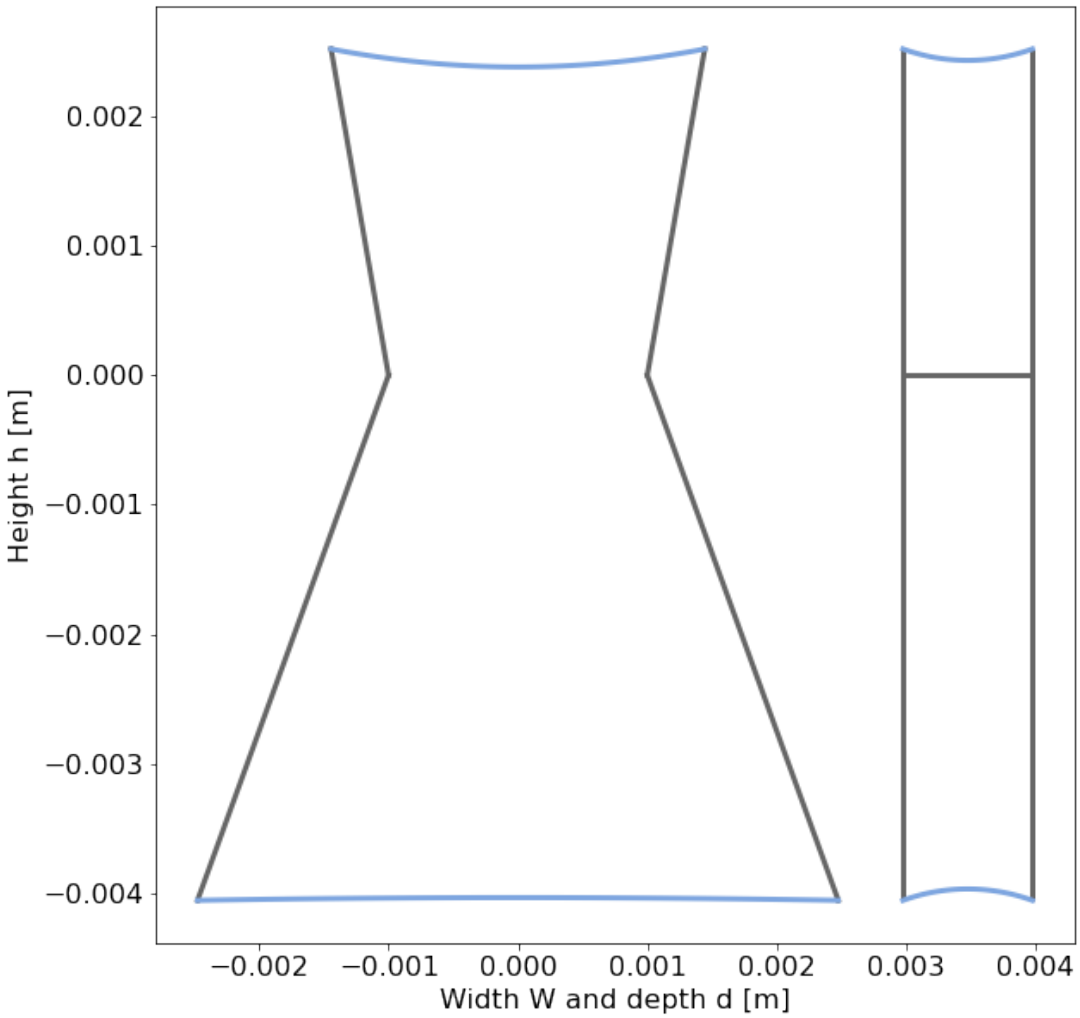

Figure 6.6: Resulting equilibrium state geometry for W_{min} = 2 mm

Table 6.4: Output data for W_{min} = 2 mm

Parameter	Value
W_1	2.89 mm
W_2	4.95 mm
W_{min}	2.00 mm
h_1	2.52 mm
h_2	4.06 mm
Volume fraction	29.6 %

Figure 6.7 is a representative sample from each of the three variations of the testing cartridges.

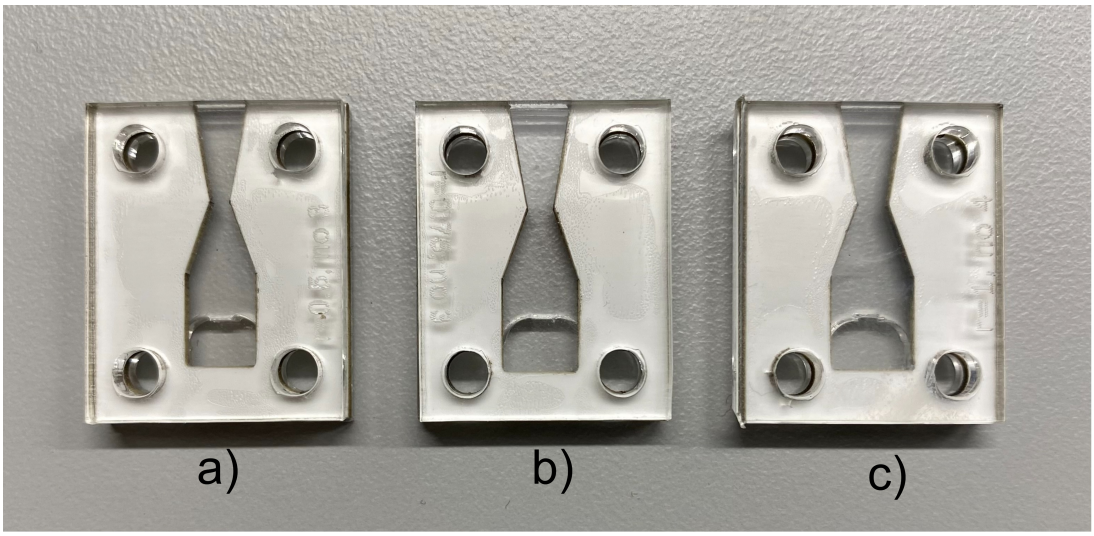

Figure 6.7: Assembled hourglass cartridges: a) W_{min} = 1 mm, b) W_{min} = 1.5 mm, c) W_{min} = 2 mm,

6.1.2 Experiment realization

The experimental setup comprises several key components, each playing an integral role. Firstly, a digital microscope is employed to capture video footage of the experiments in progress. A 3D-printed bracket holds the cartridge securely in place during the experiments. The cartridge, which serves as the focal point of the experiments, is carefully affixed to this bracket. A shared base connects the microscope and the cartridge bracket to avoid relative movement during the experiments. A table lamp is utilized to ensure clear visibility of the liquid-air interfaces, which provides the necessary illumination. Lastly, a syringe introduces controlled volumes of liquid into the system. The setup can be viewed in figure 6.8.

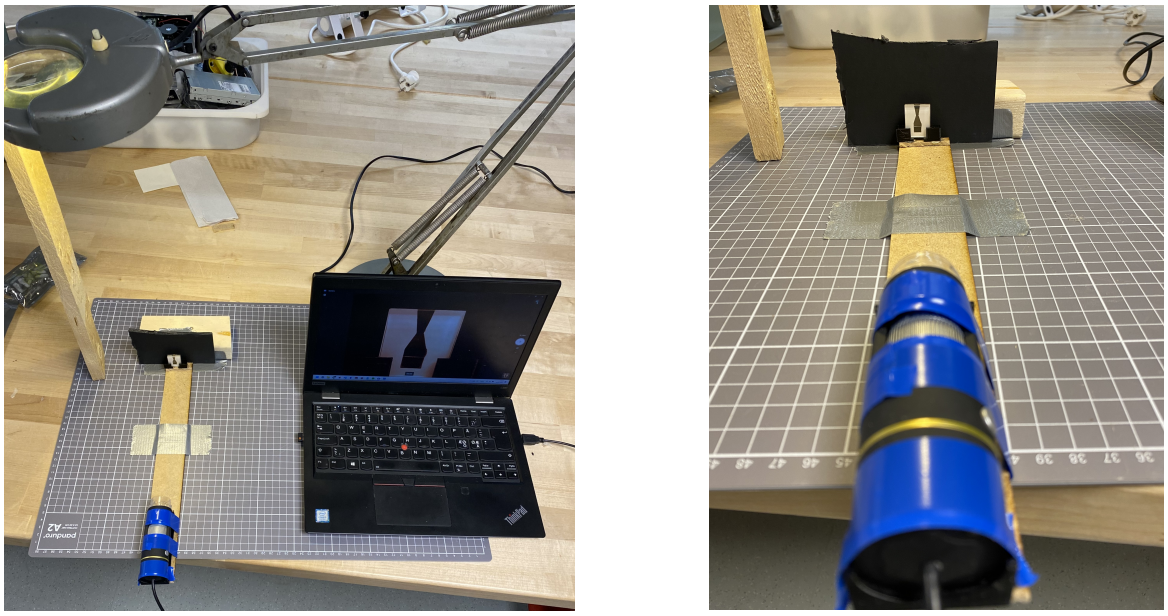

Figure 6.8: Experimental setup for hourglass cartridge tests

The experimental procedure unfolds as follows: The digital microscope is initially prepared to commence recording. Next, a syringe introduces a volume of 20 μL of water into the system. The subsequent progression of the liquid, as it traverses towards its equilibrium position, is diligently observed for a ten-minute duration, or until no visible movement is noticed for at least three minutes, for each sample. This protocol is replicated for each cartridge variant, undergoing four separate test iterations.

The data planned to be acquired from these tests include several essential metrics. In addition to proving the concept, the goal is to quantify the average contact angles, denoted as θ_W, and discern the average volume fractions above the transition point. Complementing this numerical data, observational notes regarding the duration from the introduction of the fluid to the attainment of equilibrium will also be collected. This combination of quantitative and qualitative data is meant to provide a comprehensive overview of the experiment's outcomes.

The analysis of collected data will be conducted using ImageJ [72], an open-source image processing platform developed by the National Institutes of Health. This tool facilitates precise measurements of angles, distances, and areas.

6.2 Results and Discussion

This section outlines the findings from the hourglass cartridge experiments, detailed in section 6.1, and discusses what these results suggest. The section begins with a showcase of the experiment specimens' images at times when the liquid has settled into equilibrium. This is succeeded by presenting the collected data, focusing on the volume fraction above the transition point and the contact angles. Concluding this section, anecdotal observations about the flow duration from its inception to equilibrium are discussed.

6.2.1 Equilibrium positions

Video recordings of the experiment were analyzed with ImageJ software. To determine the volume, cartridge width was employed as a reference length. Approximations of liquid areas were made by drawing polygons and measuring their respective areas. Given the channel thickness remains constant, multiplying the measured area by the thickness yielded the resultant volume. The contact angles were measured in accordingly, as can be seen in figure 6.9.

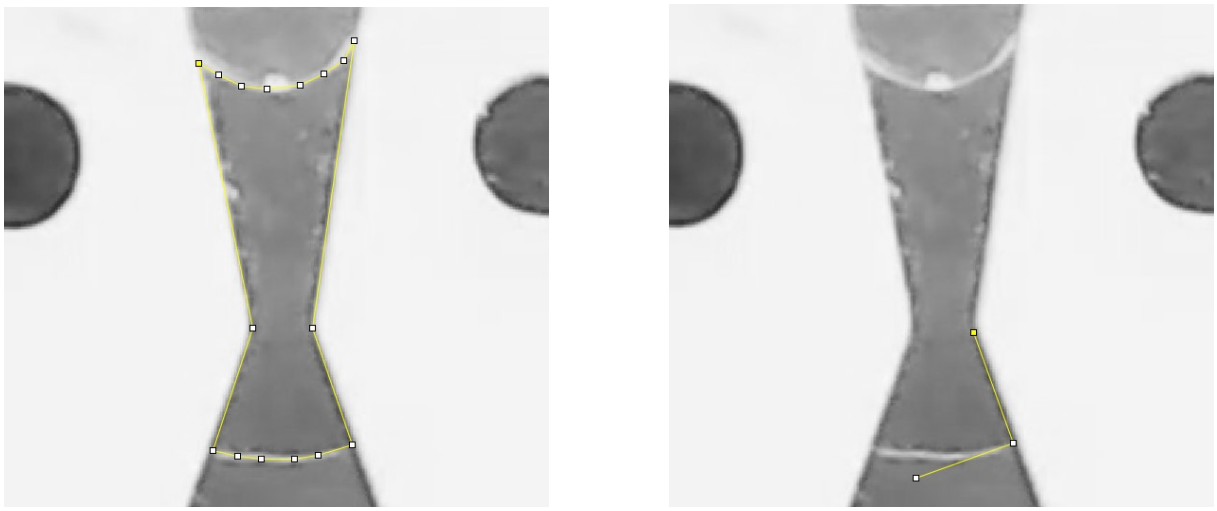

Figure 6.9: Examples on measuring a) the total volume of fluid, and b) the contact angles

Figures 6.10-6.12 illustrate the liquid equilibrium positions. The equilibrium state, defined as a stable liquid position enduring over three minutes without noticeable movement, is demonstrated for four samples each of W_{min} values 1 mm, 1.5 mm, and 2 mm.

W_{min} **= 1 mm:**

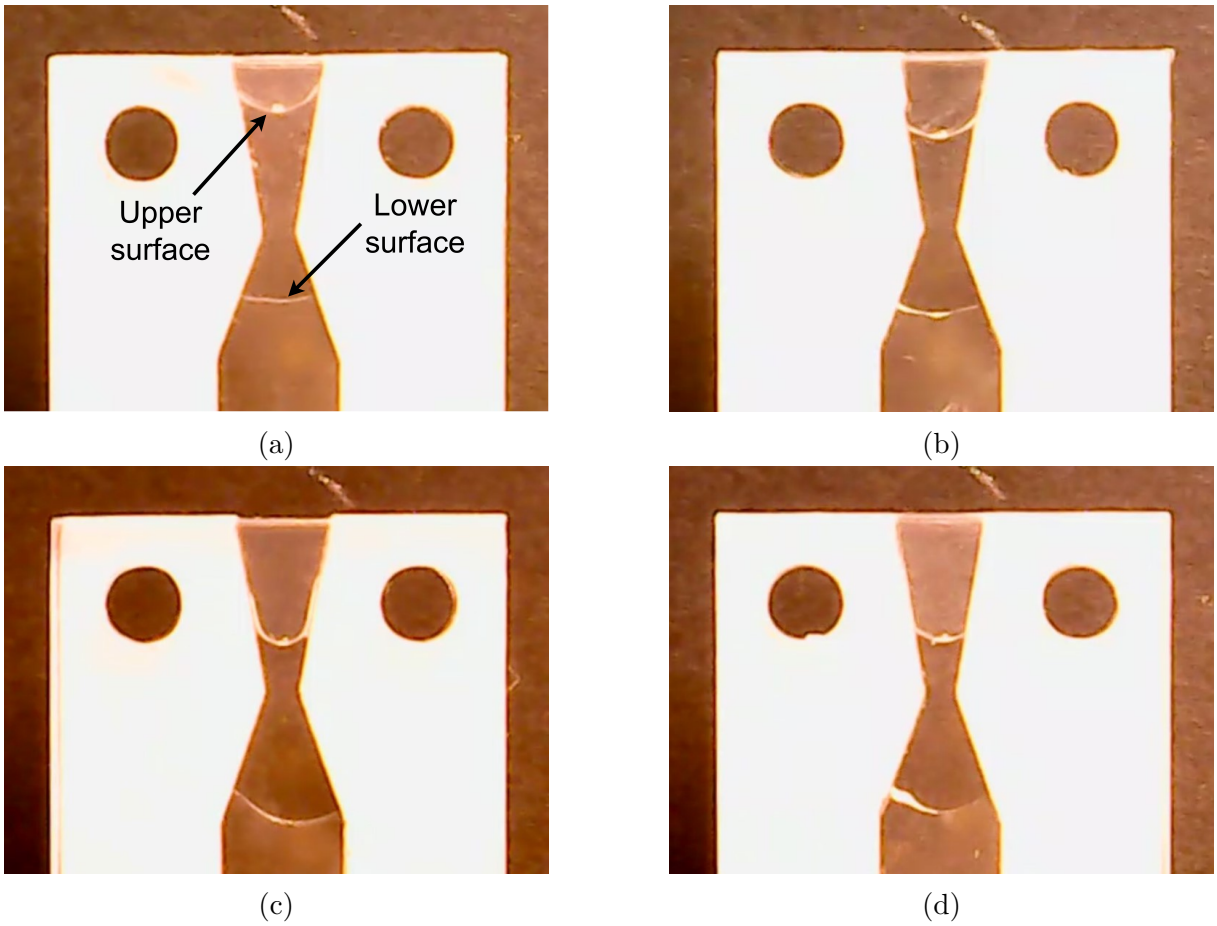

Figure 6.10: Liquid equilibrium for cartridges with W_{min} = 1 mm, samples 1-4

W_{min} **= 1.5 mm:**

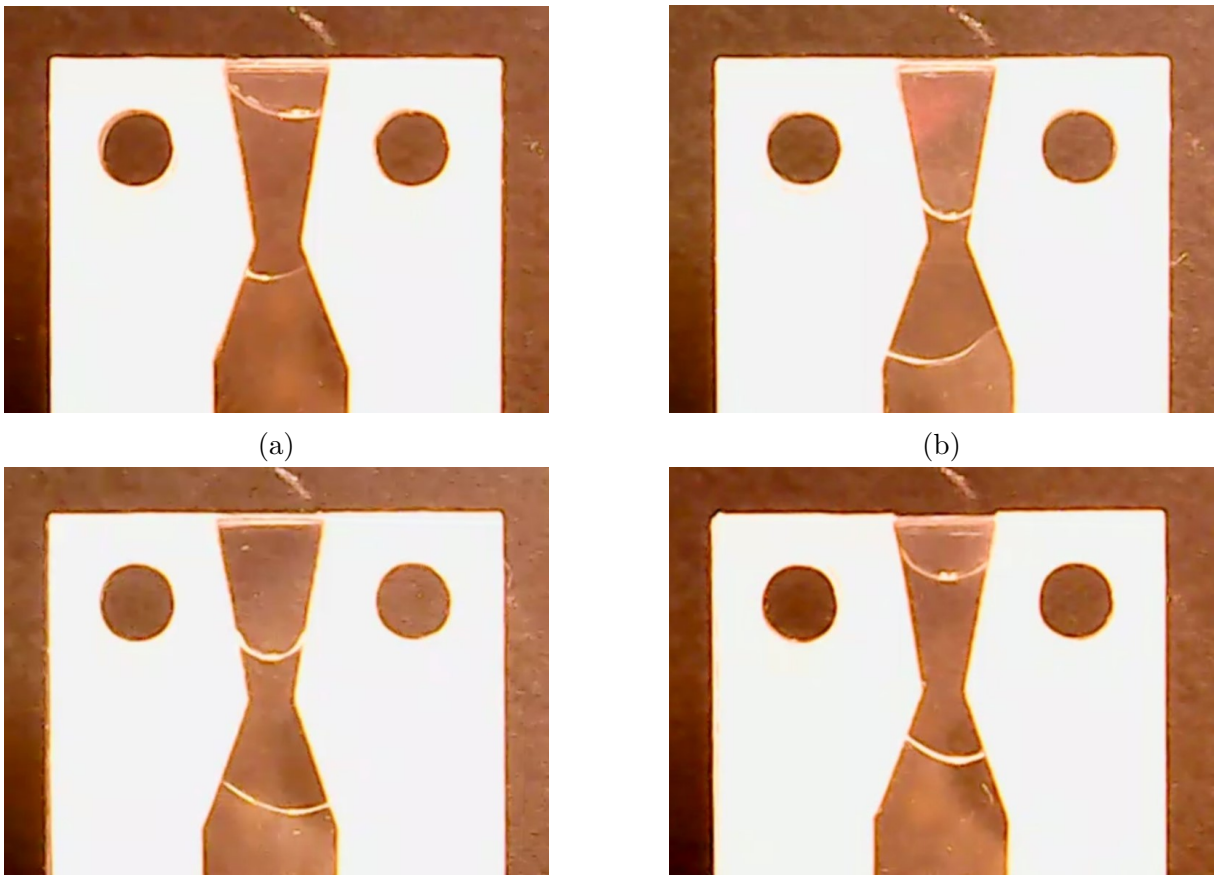

(a) (b)

(c) (d)

Figure 6.11: Liquid equilibrium for cartridges with W_{min} = 1.5 mm, samples 1-4

W_{min} **= 2 mm:**

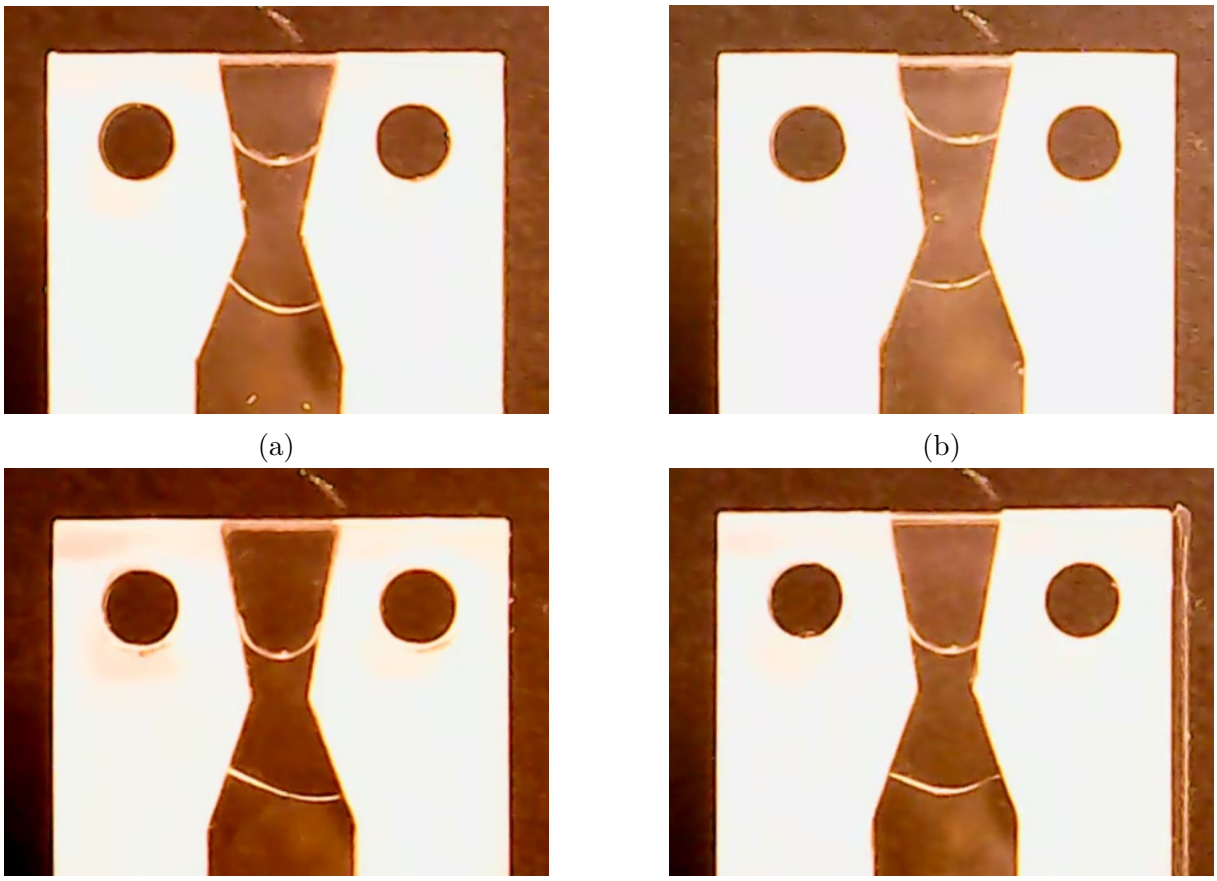

(a) (b)

(c) (d)

Figure 6.12: Liquid equilibrium for cartridges with $W_{min} = 2$ mm, samples 1-4

The results illustrated in Figures 6.10-6.12 demonstrate large variability. A key observation from the experimentation was the profound impact of the liquid's introduction height on its final position. Although the liquid consistently reached a stable equilibrium, it tended to remain close to its initial introduction point, indicating a lesser degree of fluid movement along the channel length than anticipated. Tables 6.5 and 6.6 present data on the measured total volume introduced in the separate tests, as well as the volume fractions above the transition point. The data concerning volume fractions distinctly highlight the variability that is also readily perceptible in the associated figures.

Table 6.5: Total volume of liquid V_{total} [μL] measured for all samples

Sample / W_{min} [mm]	1	2	3	4	Mean
1	19.3	17.8	21.8	18.2	19.3
1.5	20.2	19.0	20.4	21.4	20.3
2	20.0	19.4	21.8	21.0	20.6

Table 6.6: Volume fraction [%] of liquid above transition point measured for all samples

W_{min} [mm] \ Sample	1	2	3	4	Mean
1	67.6	48.9	20.9	22.4	40.0
1.5	83.9	10.8	23.5	64.6	45.7
2	48.9	63.7	25.8	23.5	40.5

The disparity in contact angles between the upper and lower surfaces is quite evident across all samples. Interestingly, a correlation seems to manifest between the values of the upper and lower contact angles. To illuminate this relationship, figure 6.13 illustrates a plot of the mean upper contact angle versus the mean lower contact angle for each sample. To provide a better understanding of this correlation, a line of linear regression is also included in the plot.

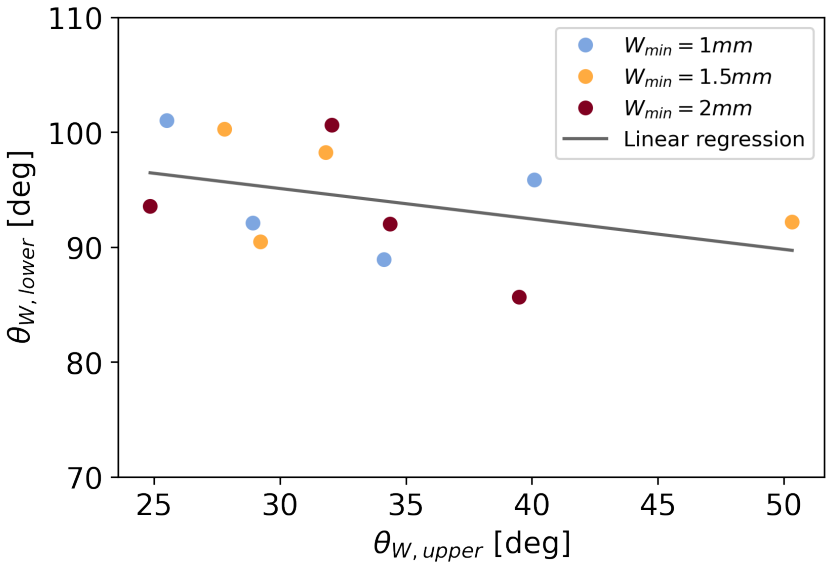

Figure 6.13: Average upper contact angles vs average lower contact angles

Despite considerable variations in individual contact angles, the mean total contact angle—which accounts for all four contact angles—displays a consistency across all samples. This consistency appears to stem from the apparent correlation between the upper and lower contact angles. The values for the mean total contact angle for all samples, along with standard error and deviation, are showcased in table 6.7.

Table 6.7: Value and standard deviation for average mean contact angle

Mean	Standard deviation
63.7	3.36

The hourglass experiments, in their entirety, demonstrate a significant level of variability. The hypothesized trend, detailed in subsection 6.1.1, suggesting a decrease in the volume

fraction above the transition point with increasing W_{min} values, could not be corroborated by the conducted experiments. This discrepancy emphasizes the complex nature of the system and indicates the presence of influential factors beyond those accounted for in the initial model.

Upon examining the equilibrium positions of the liquid, it is observed that a divergence exists between the upper and lower contact angles, θ_W. This divergence induces a concave formation on the upper surface, while the lower surface exhibits a convex form. Consequently, both surfaces exert an upward-directed force on the liquid [48], counteracting the force of gravity and facilitating a state of equilibrium where the volumes remain static .

In most instances, barring a few where the volume fraction above the transition point is exceptionally high, the principal radius of the upper surface is discernibly smaller than that of the lower surface. This can be attributed to a composite of factors, including the lower contact angle, narrower channel width, and diminished slope angle. As per Jurin's law [47], the upper surface, with its diminished principal radius, plays a more substantial role in contributing to the total capillary force vector.

The difference in contact angles at the top and bottom surfaces of the liquid significantly influences the behavior of the liquid within the cartridge. Interestingly, the liquid adheres strongly to the side walls yet does not exhibit extensive spread. Law proposes that hydrophilicity entails two separate elements; adhesion forces and surface roughness [37], a phenomenon well elucidated by the Wenzel model (3.16). According to this model, an increase in surface roughness amplifies the roughness factor, consequently increasing the contact angle. A study by Wang et al. [73] indicates a correlation between the effort required for a liquid to spread along a surface and the value of the contact angle hysteresis—the difference between advancing and receding contact angles. Furthermore, Wang et al. observe that on highly rough surfaces, there is a consistent increase in both the contact angle hysteresis and the work required for spreading the liquid across the surface. This aligns well with findings from the experiments that illustrate a high contact angle hysteresis for θ_W and a lower propensity for wetting along the side walls.

While figures 6.10-6.12 suggest a convex lower surface, it's essential to consider that this only holds for one of the principal radii. The other radius lies in the out-of-plane direction and depends on the PMMA contact angle, denoted by θ_d. As the channel's depth greatly diminishes compared to its width at the height of the lower surface, the out-of-plane principal radius will inevitably be significantly smaller than the visible radius. Consequently, it plays a more substantial role in contributing to the total capillary forces. In exploring capillary flow within rectangular microchannels, Zhu and Petkovic-Duran [74] noticed that despite the seemingly flat or even convex appearance of the liquid-gas interface from the observer's perspective, capillary flow persisted as if the surface were concave. They attributed this observation to the out-of-plane concave curvature as displayed in figure 6.14. It seems plausible that a similar mechanism could be at play in the current investigation, though definitive evidence is not available from this experiment.

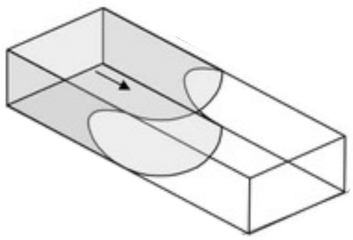

Figure 6.14: Phenomenom of capillary flow with convex in plane contact angle and concave out of plane contact angle

Source: Zhu and Petkovic-Duran [74] (Modified)

The outcomes of the empirical investigation did not entirely align with the initial hypotheses, underscoring the system's complexity under study. It is, however, noteworthy that a state of static equilibrium was consistently achieved across all experimental trials. In this state, the upper surface persistently situated itself above the transition point, with the lower surface conversely residing beneath it. While not offering definitive proof, this recurring observation provides compelling empirical indications to suggest that the uniquely hourglass-shaped channel possesses an inherent capacity for establishing equilibrium conditions.

6.2.2 Time to equilibrium

The path to equilibrium for different samples merits attention, especially when considering the contrasting behaviors of samples 1 and 2 for $W_{min} = 1.5$ mm. Sample 1, possessing a large volume fraction above the transition point, starkly contrasts with sample 2, which displays a significantly lower volume fraction. Figures 6.15 and 6.16 visually track these divergent patterns by representing the liquid movement of both samples over eight minutes. Notably, the liquid in sample 1 continues its movement throughout the entire period, whereas the liquid in sample 2 appears immobile after just two minutes, with any subsequent movement barely visible.

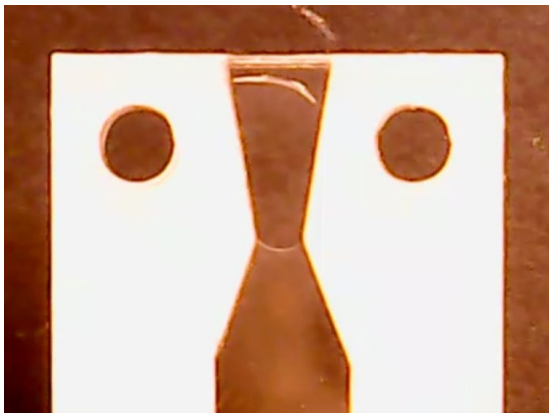

(a) 0 minutes

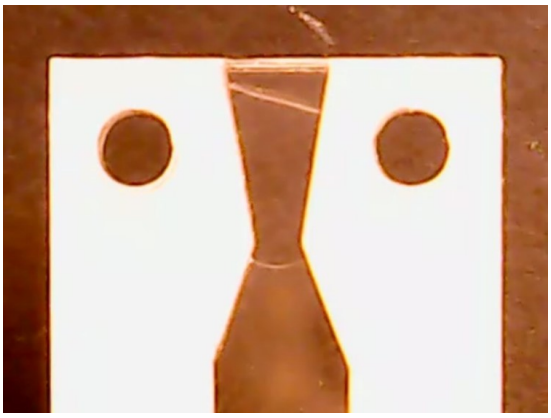

(b) 2 minutes

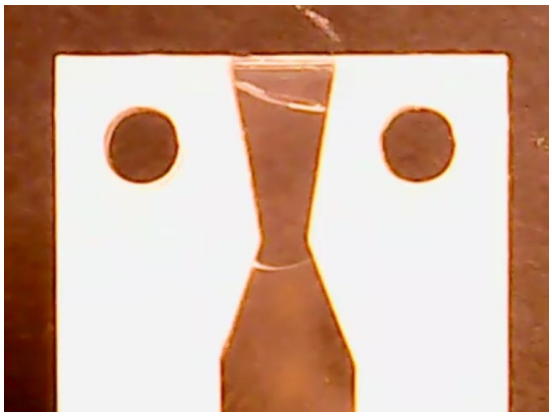

(c) 5 minutes

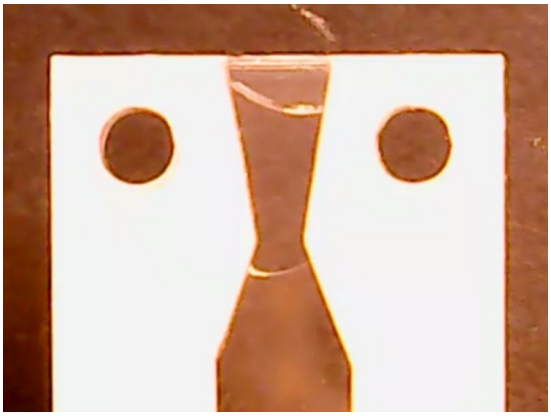

(d) 8 minutes

Figure 6.15: Liquid movement for W_{min} = 1.5 mm, sample 1, through eight minutes

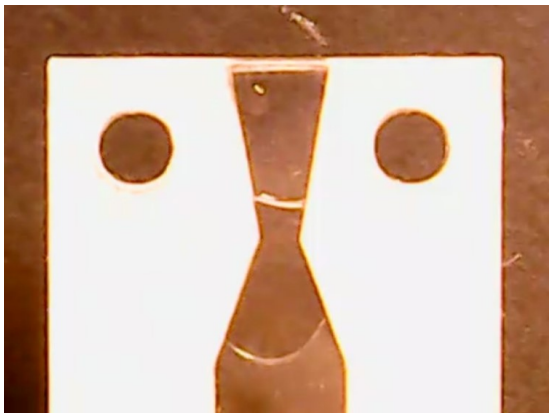

(a) 0 minutes

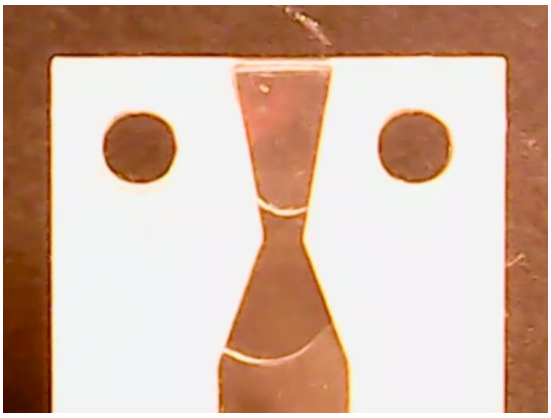

(b) 2 minutes

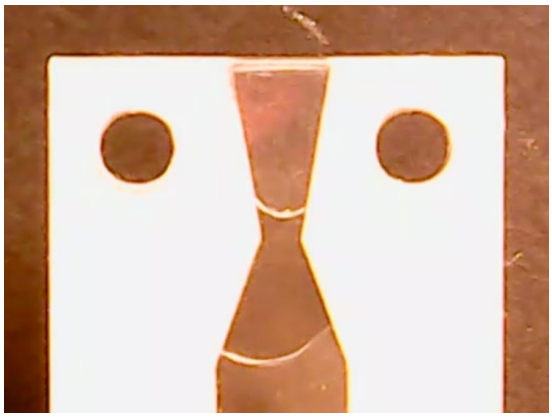

(c) 5 minutes

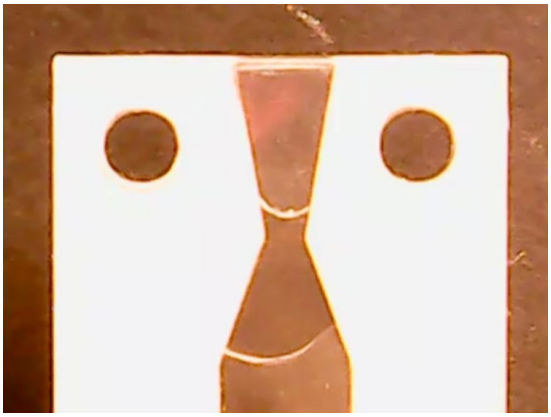

(d) 8 minutes

Figure 6.16: Liquid movement for W_{min} = 1.5 mm, sample 2, through eight minutes

The difference in time and distance taken to reach equilibrium may provide clues about the hypothetical position of equilibrium, assuming the sidewalls were more conducive to wetting. Mukhopadhyay et al. [75] noted a tangible slowdown in capillary flow speed in conditions exhibiting diminished wettability. The experiments exhibited diminished sidewall wettability, substantially impeding capillary flow. Sample one, intriguingly, continued to display significant movement for eight minutes. This suggests that if the sidewalls were smoother, facilitating better wetting, the actual equilibrium point would likely be notably lower. Conversely, sample two hardly exhibited any movement, implying that although capillary forces might be exerting upward pressure, they were unable to surmount the resistance offered by the sidewalls' wetting characteristics.

6.2.3 Experimental setup evaluation

While the experiments did not prove the hypothesized correlation between the minimum width, W_{min}, and the volume fraction above the transition point, they nonetheless provided insights regarding the liquid behavior in response to a converging-diverging channel cross-section. It was observed that the liquid consistently achieved equilibrium in all cases. However, the precise equilibrium position was subject to influences from multiple variables, encompassing surface roughness, introduction height, and potentially, factors not yet identified or fully understood.

The experimental outcomes' validity could have been improved by considering several factors. For one, a more nuanced understanding of the surface characteristics of the deployed materials was needed. For instance, a sessile droplet test could have been implemented to estimate the contact angle of the PMMA. This procedure involves placing numerous droplets on a horizontal surface and evaluating the average contact angle [76]. However, estimating the contact angle for the adhesive film sandwich structure presents complications since it is 1 mm thick. An alternative approach could encompass fabricating numerous straight capillary channels, replicating the production methodology employed for the hourglass cartridges. These channels could then be immersed in a free water surface, facilitating the documentation of the liquid-gas interface height within the capillary channel and the contact angle, θ_W.

The layer-by-layer fabrication approach adopted for the channel design was a further limitation of the experimental setup. Capillary action inherently draws the liquid into tight crevices and corners, which are hard to remove between the layers. In capillary action research, photolithography has emerged as a reliable manufacturing technique[74, 75]. By leveraging this method, it becomes feasible to eliminate leakage from the channels, thereby ensuring that capillary forces attributable to this leakage do not interfere with the study outcomes.

In general, deploying materials exhibiting superior adhesive forces and smoother surfaces for these experiments could have been advantageous. Such a modification would have amplified the capillary forces, facilitating the liquid's more effortless attainment of equilibrium positions.

Drawing on the analytical concept derived in chapter 4, it is evident that the volume fraction above the transition point is more significantly influenced by the magnitude of the fraction β/α than the distance W_{min}. Consequently, varying these parameters would have provided a more compelling proof of concept.

The inability to observe the out-of-plane contact angle, denoted as θ_d, along with the surface curvatures during the experimental process, also represents a notable limitation. A more advantageous design would feature entirely transparent channel walls and incorporate an additional recording device. Such an enhancement would enable multi-directional monitoring of the surface curvature, enriching the clarity and precision of the observations.

Finally, as alluded to previously, maintaining repeatability in the sample introduction procedure emerged as a significant obstacle. Precise consistency in liquid volume was challenging to achieve using only a rudimentary syringe. Simultaneously, the inconsistency in the introduction height and speed was noticeable and, as evidenced by the results, substantially influenced the equilibrium positions of the liquid. An ideal approach would be to incorporate a degree of automation into the sample introduction procedure to enhance the repeatability and mitigate these variables.

7 Synthesis of Findings

Through both the numerical parametric studies and the physical experiments, substantial information about the surface tension and capillary forces was obtained. In addition, it has provided insight into the potential and constraints of the hourglass concept. This chapter summarizes the insights gathered from the numerical and experimental studies and attempts to synthesize them in order to present a concise strategy for the implementation of the hourglass concept for the collection and introduction of EBC within the Inflammacheck® device. Following this, recommendations for further work are presented.

7.1 Key Findings and Implications

The theoretical understanding and the numerical results both indicate that lower contact angles and higher slope angles (α and β) increase capillary forces. The hourglass design aims to achieve two objectives: retaining the liquid within the channel up to a specific volume and facilitating its release once that volume is surpassed.

To retain the liquid effectively, the capillary forces must act against gravity. To optimize this, the upper water surface of the hourglass concepts should ideally be concave (i.e., $\theta + \alpha < 90°$) or as close to concave as possible. At the same time, the lower water surface should be convex (i.e., $\theta + \beta > 90°$) or as close to convex as possible.

Conversely, it is desirable to have the opposite configuration for maximizing the acceleration when releasing the liquid. This means the upper water surface of the hourglass concept should ideally be convex, and the lower water surface should be concave.

This creates an optimization challenge as the ideal configuration depends on several factors, such as the volume of the liquid, the desired speed of release, and the constraints imposed by the materials and manufacturing methods available. Thus, it is challenging to recommend one-size-fits-all strategies. However, several insights can be deduced:

- If the slope angle below the hourglass neck β is greater than the slope angle above the hourglass neck α. In that case, the net effect of capillary forces will be directed upwards, counteracting gravity up to a certain volume. According to the theory, this will result in a higher fraction of the liquid above the transition point and, therefore, higher gravitational potential for the flow after release.

- Lower contact angles decrease the relative influence of gravity, thus providing more control over the liquid's behavior.

The physical experiments highlighted the dependence of the equilibrium position on the

introduction height. The sidewall surfaces displayed a substantial contact angle hysteresis - the disparity between the advancing and receding contact angle - implying a high level of roughness. This led to an extremely slow liquid movement, which is unsuitable for practical applications. Conversely, surface roughness wasn't accounted for in the numerical study, and all simulations were conducted assuming perfectly smooth wall surfaces. This presumption facilitated high-speed capillary flow, an attribute challenging to attain in real-world scenarios.

Given the significant impact of surface roughness on capillary flow, it is crucial to prioritize smooth surfaces. This approach would boost capillary flow speed and enhance predictability regarding the equilibrium location for a specific volume and channel geometry. Smooth surfaces are arguably more critical than opting for materials and manufacturing methods with high wall adhesion which corresponds with low contact angles. Utilizing geometries with β significantly higher than α, the desired volumes of liquid can still be retained despite a high contact angle or low wall adhesion. However, materials exist that concurrently demonstrate high wall adhesion and exceptional smoothness.

The influence of the minimum width, W_{min}, and depth on the system's behavior was less substantial than anticipated, as evidenced by both numerical simulations and experimental observations. Specifically, when W_{min} is reduced to values below 1 mm, it constrains the liquid flow but without a corresponding significant enhancement in capillary forces. It is prudent, therefore, to exercise caution in employing small values of W_{min}. However, it is essential to note that additional research is necessary to arrive at a more definitive understanding of the effects of minimal channel width.

In the broader perspective, the minimum width of the hourglass at the neck W_{min} and the out-of-plane depth of the channel appear to be the less critical parameters influencing the system's behavior. Other factors had a more significant impact on the performance of the system. Consequently, efforts to optimize the design or understand its underlying principles should prioritize investigating and modulating the more influential parameters, like slope angles, contact angles, and surface roughness.

7.2 Further Work

Rigorous testing of contact angles and hysteresis

A significant limitation of the experiment was the uncertainty related to the contact angle and surface roughness. Two additional experiments were planned but not conducted to clarify these aspects. Similar to the original, the first additional experiment would use a straight cylindrical channel to isolate the contact angle hysteresis more effectively, enabling comparisons with theoretical models and other experimental results. The second additional experiment involves submerging a straight cylinder in water and closely monitoring height and contact angle changes over time. This would offer critical data on how the liquid interacts with the surface and the role of surface roughness on contact angle and hysteresis.

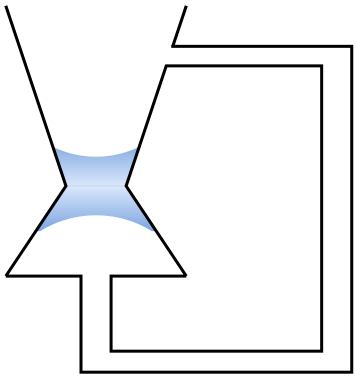

Figure 7.1: Illustration of the closed loop design concept

Rush mechanism testing

While the experiments in this thesis focus on understanding the liquid equilibrium of the hourglass concept, testing the hypothesized rush function of the concept is just as vital in order to implement the concept into a functioning product. This should be further investigated by altering the cartridge design utilized in the experiments to include a narrow straight channel at the bottom, which is exposed to ambient air.

Closed loop

The scope of breathalyzers like the Inflammacheck® extends beyond measuring H_2O_2. The technology can also be proficient at detecting the presence of bacteria and viruses. However, to realize this application, it's imperative to prevent the patient's breath from dispersing into the air - ensuring no EBC particles escape from the device during testing or come in contact with the ambient air. It should be investigated if the hourglass concept could achieve this by incorporating a closed-loop design, integrating an airflow channel linking the air space above and beneath the EBC volume. An illustration of this design is presented in figure 7.1. Coupling this solution with particle filters in the Inflammacheck® flow chamber could ensure the containment of EBC particles within the device, preventing their escape into the surrounding air.

Geometry improvements

It should be investigated if adding a rush funnel at the end of the hourglass geometry could accelerate the liquid as it nears the end of its path. This acceleration might be crucial in certain applications and could enhance the device's functionality.

As the study progressed, several ideas emerged for possible improvements to the device's geometry.

Non-Linear Walls: One of the possibilities is incorporating walls that aren't straight. Curved or angled walls could affect the liquid flow and the capillary forces in beneficial ways, and exploring different shapes might result in an optimized design. Gorce et al. [77] investigated the capillary imbibition into converging tubes with curved walls and

theoretically derived the optimal wall shape for capillary flow speed. This concept could also be applied to the hourglass concept.

Exploring Out-of-Plane Geometries: Investigating geometries that extend out of the plane, such as slopes, might have interesting effects on how the liquid moves. These geometries could offer alternative paths or innovatively influence the forces acting on the liquid.

Analytical solutions

One limitation associated with the differential form of the Young-Laplace equation (3.9) was that its boundary conditions were not directly based on the liquid volume. Additionally, calculating the volume beneath the curve derived from solving the differential equation necessitated numerical integration. This introduced significant constraints on the utility and applicability of the analytical solution of the Young-Laplace equation.

Attempts were made to reformulate the equation to incorporate the liquid volume as a direct parameter. However, it was not possible to achieve this within the scope and limited time frame of this study. Additionally, it requires in-depth mathematical and geometry understanding beyond undergraduate mathematics studies.

Ideally, incorporating the differential form of the Young-Laplace equation into the analytical framework for the hourglass concept would enable a more comprehensive representation of the system. This integration would account for the effects of gravity and the influences of in-plane surface curvature. However, achieving this integration requires overcoming the aforementioned challenges and possibly devising a more sophisticated approach to relate the equation to the liquid volume directly.

Numerical simulations

Two objectives for the numerical simulations, which were not realized, involved the simulation of dual water surfaces and the incorporation of surface roughness effects. An attempt was made to simulate two water surfaces, but the endeavor faced challenges such as slow convergence and instability during simulation. However, with additional time and computational resources, successful simulation of dual surfaces is likely feasible.

Incorporating surface roughness, on the other hand, poses a more complex challenge. It appears that there are no standard implementations in Comsol or Ansys that inherently consider surface roughness without explicitly explaining the geometrical features of the rough surface. This would demand a significantly higher level of computational resources, the exploration of alternative solvers, or even the development of intelligent simplifications to approximate the effects of surface roughness.

In addition to these objectives, a few straightforward enhancements can be made to the simulation strategy. For instance, initiating the simulation with a theoretically curved surface would be beneficial. Another improvement is extending the simulation runtime to

capture the system until it reaches equilibrium. Moreover, it is vital to judiciously select and limit the number of essential parameters in the simulation, ensuring that the analysis remains focused and manageable without compromising the integrity of the results.

Concepts with other forces/phenomena

During this thesis's initial stages, various concepts for volume-control valve mechanisms were explored, as documented in the Preliminary Study (section 2.4). These concepts, summarized in Table 2.1, ranged from capillary force balances and hydrophobic barriers to electrowetting and mechanical valves. While the focus of this thesis ultimately narrowed to an in-depth examination and development of a select few concepts, it is essential to acknowledge that several potentially viable alternatives were set aside due to the scope and constraints of this master thesis.

As part of future work, revisiting and further investigating these sidelined concepts may be valuable. For example, electrowetting, which offers fine-tuned control over fluid wettability by applying an electric field, may present innovative avenues for controlling fluid flow. Similarly, integrating hydrophobic barriers or employing microfluidic pumps could be examined for their feasibility and efficacy in specific applications. Moreover, combining different concepts, possibly integrating features from multiple mechanisms, could yield hybrid solutions that capitalize on the strengths of individual approaches.

It is imperative to weigh the merits and drawbacks of each concept against the specific requirements of the application at hand. Additionally, advancements in materials, manufacturing techniques, and computational tools may open new possibilities or alter the feasibility of various concepts. As such, the sidelined concepts from the Preliminary Study should not be disregarded but considered as potential starting points for further research and development in microfluidics.

8 Conclusion

This thesis addresses the challenge of collecting and transporting exhaled breath condensate in the sensor cartridge of the Inflammacheck® breathalyzer through an innovative method based on surface tension and capillary action. The comprehensive investigation entailed analytical calculations, numerical simulations, and experimental study, focusing on the hourglass concept developed around converging and diverging capillary channels.

Through a combination of analytical, numerical, and experimental analysis, the thesis provides an understanding of the critical factors governing capillary flow in the sensor cartridge. It was established that the capillary forces in converging and diverging channels are influenced by the sum of the channel slope and the angle contact angle between the channel surface and the liquid-gas surface. By manipulating these factors, a desired equilibrium position can be achieved for a specific volume of liquid. This observation provides a fundamental mechanism for designing systems where the capillary forces can effectively retain the liquid and subsequently aid in its release toward the biosensor.

However, the experimental results highlighted surface roughness as a significant factor impeding capillary flow. The study revealed a discrepancy between idealized numerical simulations and the results from the experimental study due to surface roughness, emphasizing the importance of material selection and manufacturing aiming at smooth surfaces for efficient transport of the condensate.

In summary, this thesis presents a promising solution for EBC collection and deployment in breathalyzers, provides valuable insights into the influence of surface properties and geometric parameters, and highlights the profound impact of surface roughness on capillary flow. For developing a prototype with commercial potential, it is crucial to prioritize modulating the more influential parameters, like slope angles, contact angles, and surface roughness.

The findings in this thesis are not only relevant for the improvement of devices like Inflammacheck® but also contribute to the broader scientific understanding of capillary action and surface tension.

Bibliography

1. Afrooz PN, Pozner JN, and DiBernardo BE. Noninvasive and Minimally Invasive Techniques in Body Contouring. English. Clinics in Plastic Surgery 2014 Oct; 41. Publisher: Elsevier:789–804. DOI: 10.1016/j.cps.2014.07.006. Available from: https://www.plasticsurgery.theclinics.com/article/S0094-1298(14)00097-2/fulltext [Accessed on: 2023 Jun 24]
2. Norwitz ER and Levy B. Noninvasive Prenatal Testing: The Future Is Now. Reviews in Obstetrics and Gynecology 2013; 6:48–62. Available from: https://www.ncbi.nlm.nih.gov/pmc/articles/PMC3893900/ [Accessed on: 2023 Jun 24]
3. Warsof SL, Larion S, and Abuhamad AZ. Overview of the impact of noninvasive prenatal testing on diagnostic procedures. en. Prenatal Diagnosis 2015; 35. _eprint: https://onlinelibrary.wiley.com/doi/pdf/10.1002/pd.4601:972–9. DOI: 10.1002/pd.4601. Available from: https://onlinelibrary.wiley.com/doi/abs/10.1002/pd.4601 [Accessed on: 2023 Jun 24]
4. Barsanti C, Lenzarini F, and Kusmic C. Diagnostic and prognostic utility of non-invasive imaging in diabetes management. World Journal of Diabetes 2015 Jun; 6:792–806. DOI: 10.4239/wjd.v6.i6.792. Available from: https://www.ncbi.nlm.nih.gov/pmc/articles/PMC4478576/ [Accessed on: 2023 Jun 24]
5. Murugan A and Sharma G. Obesity and respiratory diseases. en. Chronic Respiratory Disease 2008 Nov; 5. Publisher: SAGE Publications Ltd STM:233–42. DOI: 10.1177/1479972308096978. Available from: https://doi.org/10.1177/1479972308096978 [Accessed on: 2023 Jun 9]
6. Ferkol T and Schraufnagel D. The Global Burden of Respiratory Disease. Annals of the American Thoracic Society 2014 Mar; 11. Publisher: American Thoracic Society - AJRCCM:404–6. DOI: 10.1513/AnnalsATS.201311-405PS. Available from: https://www.atsjournals.org/doi/full/10.1513/AnnalsATS.201311-405PS [Accessed on: 2023 Jun 9]
7. Maniscalco M, Ambrosino P, Ciullo A, Fuschillo S, Valente V, Gaudiosi C, Paris D, Cobuccio R, Stefanelli F, and Motta A. A Rapid Antigen Detection Test to Diagnose SARS-CoV-2 Infection Using Exhaled Breath Condensate by A Modified Inflammacheck® Device. en. Sensors 2021 Jan; 21. Number: 17 Publisher: Multidisciplinary Digital Publishing Institute:5710. DOI: 10.3390/s21175710. Available from: https://www.mdpi.com/1424-8220/21/17/5710 [Accessed on: 2023 Jun 9]
8. Neville DM, Fogg C, Brown TP, Jones TL, Lanning E, Bassett P, and Chauhan AJ. Using the Inflammacheck Device to Measure the Level of Exhaled Breath Condensate Hydrogen Peroxide in Patients With Asthma and Chronic Obstructive Pulmonary Disease (The EXHALE Pilot Study): Protocol for a Cross-Sectional Feasibility Study. EN. JMIR Research Protocols 2018 Jan; 7. Company: JMIR Research Protocols Distributor: JMIR Research Protocols Institution: JMIR Research Protocols Label: JMIR Research Protocols Publisher:

JMIR Publications Inc., Toronto, Canada:e8768. DOI: 10.2196/resprot.8768. Available from: https://www.researchprotocols.org/2018/1/e25 [Accessed on: 2023 Jun 9]
9. Inflammacheck® – Inflammacheck. en-US. Available from: https://www.exhalationtechnology.com/inflammacheck/ [Accessed on: 2023 Jun 28]
10. Domènech-Clar R, López-Andreu J, Compte-Torrero L, De Diego-Damiá A, Macián-Gisbert V, Perpiñá-Tordera M, and Roqués-Serradilla J. Maximal static respiratory pressures in children and adolescents. en. Pediatric Pulmonology 2003; 35. _eprint: https://onlinelibrary.wiley.com/doi/pdf/10.1002/ppul.10217:126–32. DOI: 10.1002/ppul.10217. Available from: https://onlinelibrary.wiley.com/doi/abs/10.1002/ppul.10217 [Accessed on: 2023 Jun 12]
11. Hettiarachchi K and Lee AP. VENTURI-BASED TWO-LAYER MICROFLUIDIC PUMPING SYSTEM. en. San Diego 2008
12. Saha S and Team TE. High accuracy microfluidic pumps. en. Elveflow 2021 Jun. Publisher: Elvesys. Available from: https://www.elveflow.com/microfluidic-products/microfluidics-flow-control-systems/high-accuracy-vacuum-pressure-pumps/ [Accessed on: 2023 Jun 12]
13. Micropumps. en-GB. Available from: https://www.bartels-mikrotechnik.de/en/micropumps/ [Accessed on: 2023 Jun 12]
14. Nguyen NT and Truong TQ. A fully polymeric micropump with piezoelectric actuator. en. Sensors and Actuators B: Chemical 2004 Jan; 97:137–43. DOI: 10.1016/S0925-4005(03)00521-5. Available from: https://www.sciencedirect.com/science/article/pii/S0925400503005215 [Accessed on: 2022 Oct 17]
15. Li L, Wang X, Pu Q, and Liu S. Advancement of electroosmotic pump in microflow analysis: A review. en. Analytica Chimica Acta 2019 Jul; 1060:1–16. DOI: 10.1016/j.aca.2019.02.004. Available from: https://www.sciencedirect.com/science/article/pii/S0003267019301643 [Accessed on: 2023 Jun 11]
16. Wang X, Cheng C, Wang S, and Liu S. Electroosmotic pumps and their applications in microfluidic systems. en. Microfluidics and Nanofluidics 2009 Feb; 6:145–62. DOI: 10.1007/s10404-008-0399-9. Available from: https://doi.org/10.1007/s10404-008-0399-9 [Accessed on: 2023 Jun 11]
17. Takamura Y, Onoda H, Inokuchi H, Adachi S, Oki A, and Horiike Y. Low-voltage electroosmosis pump for stand-alone microfluidics devices. en. ELECTROPHORESIS 2003; 24. _eprint: https://onlinelibrary.wiley.com/doi/pdf/10.1002/elps.200390012:185–92. DOI: 10.1002/elps.200390012. Available from: https://onlinelibrary.wiley.com/doi/abs/10.1002/elps.200390012 [Accessed on: 2023 Jun 11]
18. Chen G and Das S. Electroosmotic transport in polyelectrolyte-grafted nanochannels with pH-dependent charge density. Journal of Applied Physics 2015 May; 117:185304. DOI: 10.1063/1.4919813
19. Olanrewaju A, Beaugrand M, Yafia M, and Juncker D. Capillary microfluidics in microchannels: from microfluidic networks to capillaric circuits. en. Lab on a Chip 2018; 18. Publisher: Royal Society of Chemistry:2323–47. DOI: 10.1039/C8LC00458

G. Available from: https://pubs.rsc.org/en/content/articlelanding/2018/lc/c8lc00458g [Accessed on: 2023 Jun 11]
20. Nenad M, Rong X, Daniel John P, Ryan E, Ian M, and Evelyn N. W. Condensation on Hydrophilic, Hydrophobic, Nanostructured Superhydrophobic and Oil-Infused Surfaces. en. Journal of Heat Transfer 2013 Aug; 135:080906. DOI: 10 . 1115 / 1 . 4024188. Available from: https://asmedigitalcollection.asme.org/heattransfer/article/doi/10.1115/1.4024188/374832/Condensation-on-Hydrophilic-Hydrophobic [Accessed on: 2023 Jun 12]
21. El Fil B, Kini G, and Garimella S. A review of dropwise condensation: Theory, modeling, experiments, and applications. en. International Journal of Heat and Mass Transfer 2020 Oct; 160:120172. DOI: 10.1016/j.ijheatmasstransfer.2020.120172. Available from: https://www.sciencedirect.com/science/article/pii/S0017931020331082 [Accessed on: 2023 Jun 11]
22. Yang L, Luo X, Chang W, Tian Y, Wang Z, Gao J, Cai Y, Qin Y, and Duxbury M. Manufacturing of anti-fogging super-hydrophilic microstructures on glass by nanosecond laser. en. Journal of Manufacturing Processes 2020 Nov; 59:557–65. DOI: 10.1016/j.jmapro.2020.10.011. Available from: https://www.sciencedirect.com/science/article/pii/S1526612520306794 [Accessed on: 2023 Jun 12]
23. Ems H and Ndao S. Microstructure-alone induced transition from hydrophilic to hydrophobic wetting state on silicon. en. Applied Surface Science 2015 Jun; 339:137–43. DOI: 10 . 1016 / j . apsusc . 2015 . 02 . 135. Available from: https://www.sciencedirect.com/science/article/pii/S0169433215004511 [Accessed on: 2023 Jun 12]
24. Grassin C. Microfluidics Electrowetting platform. en. Available from: https://charleslabs.fr/en/project-Microfluidics+Electrowetting+platform [Accessed on: 2023 Jun 12]
25. Moradi M, Chini SF, and Rahimian MH. Vibration-enhanced condensation heat transfer on superhydrophobic surfaces: An experimental study. AIP Advances 2020 Sep; 10:095123. DOI: 10 . 1063 / 5 . 0020139. Available from: https://doi.org/10.1063/5.0020139 [Accessed on: 2023 Jun 12]
26. Oh I, Cha H, Chen J, Chavan S, Kong H, Miljkovic N, and Hu Y. Enhanced Condensation on Liquid-Infused Nanoporous Surfaces by Vibration-Assisted Droplet Sweeping. ACS Nano 2020 Oct; 14. Publisher: American Chemical Society:13367–79. DOI: 10 . 1021 / acsnano . 0c05223. Available from: https://doi.org/10.1021/acsnano.0c05223 [Accessed on: 2023 Jun 12]
27. Hong Y, Chi Y, Wu S, Li Y, Zhu Y, and Yin J. Boundary curvature guided programmable shape-morphing kirigami sheets. en. Nature Communications 2022 Jan; 13. Number: 1 Publisher: Nature Publishing Group:530. DOI: 10 . 1038 / s41467 - 022 - 28187 - x. Available from: https://www.nature.com/articles/s41467-022-28187-x [Accessed on: 2023 Jun 12]
28. Al-Faqheri W, Thio THG, Qasaimeh MA, Dietzel A, Madou M, and Al-Halhouli A. Particle/cell separation on microfluidic platforms based on centrifugation effect: a review. en. Microfluidics and Nanofluidics 2017 May; 21:102. DOI: 10.1007/s10404-017-1933-4. Available from: https://doi.org/10.1007/s10404-017-1933-4 [Accessed on: 2023 Jun 11]

29. Berry MV. The molecular mechanism of surface tension. en. Physics Education 1971 Mar; 6:79. DOI: 10.1088/0031-9120/6/2/001. Available from: https://dx.doi.org/10.1088/0031-9120/6/2/001 [Accessed on: 2023 Jun 10]
30. Surface Tension and Water — U.S. Geological Survey. Available from: https://www.usgs.gov/special-topics/water-science-school/science/surface-tension-and-water [Accessed on: 2023 Jun 10]
31. Dezellus O and Eustathopoulos N. Fundamental issues of reactive wetting by liquid metals. en. Journal of Materials Science 2010 Aug; 45:4256–64. DOI: 10.1007/s10853-009-4128-x. Available from: https://doi.org/10.1007/s10853-009-4128-x [Accessed on: 2023 Jun 10]
32. Vafaei S and Podowski MZ. Theoretical analysis on the effect of liquid droplet geometry on contact angle. en. Nuclear Engineering and Design. Festschrift Edition Celebrating the 65th Birthday of Prof. Richard T. Lahey, Jr. 2005 May; 235:1293–301. DOI: 10.1016/j.nucengdes.2005.02.026. Available from: https://www.sciencedirect.com/science/article/pii/S0029549305000932 [Accessed on: 2023 Apr 27]
33. Bashforth F and Adams JC. An Attempt to Test the Theories of Capillary Action by Comparing the Theoretical and Measured Forms of Drops of Fluid. en. Google-Books-ID: n94EAAAAYAAJ. University Press, 1883
34. Siqveland LM and Skjæveland SM. Derivations of the Young-Laplace equation. en. Capillarity 2021 Jun; 4:23–30. DOI: 10.46690/capi.2021.02.01. Available from: https://www.sciopen.com/article/10.46690/capi.2021.02.01 [Accessed on: 2023 Jun 10]
35. Taylor J. II—mean curvature and weighted mean curvature. en. Acta Metallurgica et Materialia 1992 Jul; 40:1475–85. DOI: 10.1016/0956-7151(92)90091-R. Available from: https://linkinghub.elsevier.com/retrieve/pii/095671519290091R [Accessed on: 2023 Jun 15]
36. Gaydos J and Neumann AW. The dependence of contact angles on drop size and line tension. en. Journal of Colloid and Interface Science 1987 Nov; 120:76–86. DOI: 10.1016/0021-9797(87)90324-9. Available from: https://www.sciencedirect.com/science/article/pii/0021979787903249 [Accessed on: 2023 Jun 11]
37. Law KY. Definitions for Hydrophilicity, Hydrophobicity, and Superhydrophobicity: Getting the Basics Right. The Journal of Physical Chemistry Letters 2014 Feb; 5. Publisher: American Chemical Society:686–8. DOI: 10.1021/jz402762h. Available from: https://doi.org/10.1021/jz402762h [Accessed on: 2023 Jun 11]
38. Wenzel RN. RESISTANCE OF SOLID SURFACES TO WETTING BY WATER. Industrial & Engineering Chemistry 1936 Aug; 28. Publisher: American Chemical Society:988–94. DOI: 10.1021/ie50320a024. Available from: https://doi.org/10.1021/ie50320a024 [Accessed on: 2023 Jun 11]
39. Cassie A and Baxter S. Wettability of porous surfaces. English. Transactions of the Faraday Society 1944; 40:546–51. DOI: 10.1039/tf9444000546
40. Honschoten JWv, Brunets N, and R. Tas N. Capillarity at the nanoscale. en. Chemical Society Reviews 2010; 39. Publisher: Royal Society of Chemistry:1096–114. DOI: 10.1039/B909101G. Available from: https://pubs.rsc.org/en/content/articlelanding/2010/cs/b909101g [Accessed on: 2023 Jun 11]

41. Rayleigh L. On the Theory of the Capillary Tube. Proceedings of the Royal Society of London. Series A, Containing Papers of a Mathematical and Physical Character 1916; 92. Publisher: The Royal Society:184–95. Available from: https://www.jstor.org/stable/93546 [Accessed on: 2023 May 27]
42. Lucas R. Ueber das Zeitgesetz des kapillaren Aufstiegs von Flüssigkeiten. 1918 Jul. DOI: 10.1007/bf01461107. Available from: https://zenodo.org/record/1428302 [Accessed on: 2023 Jun 11]
43. Washburn EW. The Dynamics of Capillary Flow. en. Physical Review 1921 Mar; 17:273–83. DOI: 10.1103/PhysRev.17.273. Available from: https://link.aps.org/doi/10.1103/PhysRev.17.273 [Accessed on: 2023 Apr 28]
44. Carnahan RD and Hou SL. Ink Jet Technology. IEEE Transactions on Industry Applications 1977 Jan; IA-13. Conference Name: IEEE Transactions on Industry Applications:95–104. DOI: 10.1109/TIA.1977.4503368
45. Li X, Zhao Y, and Zhao C. Applications of capillary action in drug delivery. en. iScience 2021 Jul; 24:102810. DOI: 10.1016/j.isci.2021.102810. Available from: https://www.sciencedirect.com/science/article/pii/S2589004221007781 [Accessed on: 2023 Jun 12]
46. Narayanamurthy V, E. Jeroish Z, S. Bhuvaneshwari K, Bayat P, Premkumar R, Samsuri F, and M. Yusoff M. Advances in passively driven microfluidics and lab-on-chip devices: a comprehensive literature review and patent analysis. en. RSC Advances 2020; 10. Publisher: Royal Society of Chemistry:11652–80. DOI: 10.1039/D0RA00263A. Available from: https://pubs.rsc.org/en/content/articlelanding/2020/ra/d0ra00263a [Accessed on: 2023 Jun 12]
47. Rodríguez-Valverde MÁ and Miranda MT. Derivation of Jurin's law revisited. en. European Journal of Physics 2010 Nov; 32:49. DOI: 10.1088/0143-0807/32/1/005. Available from: https://dx.doi.org/10.1088/0143-0807/32/1/005 [Accessed on: 2023 Jun 12]
48. Ivanov D and Petrova H. Capillary effects. en. Physics Education 2000 Jul; 35:262. DOI: 10.1088/0031-9120/35/4/08. Available from: https://dx.doi.org/10.1088/0031-9120/35/4/08 [Accessed on: 2023 Apr 29]
49. Ouali FF, McHale G, Javed H, Trabi C, Shirtcliffe NJ, and Newton MI. Wetting considerations in capillary rise and imbibition in closed square tubes and open rectangular cross-section channels. en. Microfluidics and Nanofluidics 2013 Sep; 15:309–26. DOI: 10.1007/s10404-013-1145-5. Available from: https://doi.org/10.1007/s10404-013-1145-5 [Accessed on: 2023 Apr 28]
50. Erickson D, Li D, and Park C. Numerical Simulations of Capillary-Driven Flows in Nonuniform Cross-Sectional Capillaries. en. Journal of Colloid and Interface Science 2002 Jun; 250:422–30. DOI: 10.1006/jcis.2002.8361. Available from: https://linkinghub.elsevier.com/retrieve/pii/S002197970298361X [Accessed on: 2023 May 27]
51. Wörner M. Numerical modeling of multiphase flows in microfluidics and micro process engineering: a review of methods and applications. en. Microfluidics and Nanofluidics 2012 May; 12:841–86. DOI: 10.1007/s10404-012-0940-8. Available from: https://doi.org/10.1007/s10404-012-0940-8 [Accessed on: 2023 Jun 14]
52. Saidi MS, Rismanian M, Monjezi M, Zendehbad M, and Fatehiboroujeni S. Comparison between Lagrangian and Eulerian approaches in predicting motion of micron-sized particles in laminar flows. en. Atmospheric Environment 2014 Jun;

89:199–206. DOI: 10.1016/j.atmosenv.2014.01.069. Available from: https://www.sciencedirect.com/science/article/pii/S1352231014000946 [Accessed on: 2023 Jun 14]
53. Tryggvason G, Bunner B, Esmaeeli A, Juric D, Al-Rawahi N, Tauber W, Han J, Nas S, and Jan YJ. A Front-Tracking Method for the Computations of Multiphase Flow. en. Journal of Computational Physics 2001 May; 169:708–59. DOI: 10.1006/jcph.2001.6726. Available from: https://linkinghub.elsevier.com/retrieve/pii/S0021999101967269 [Accessed on: 2023 Jun 14]
54. Wang ZB, Chen R, Wang H, Liao Q, Zhu X, and Li SZ. An overview of smoothed particle hydrodynamics for simulating multiphase flow. en. Applied Mathematical Modelling 2016 Dec; 40:9625–55. DOI: 10.1016/j.apm.2016.06.030. Available from: https://www.sciencedirect.com/science/article/pii/S0307904X16303419 [Accessed on: 2023 Jun 14]
55. Gunstensen AK, Rothman DH, Zaleski S, and Zanetti G. Lattice Boltzmann model of immiscible fluids. en. Physical Review A 1991 Apr; 43:4320–7. DOI: 10.1103/PhysRevA.43.4320. Available from: https://link.aps.org/doi/10.1103/PhysRevA.43.4320 [Accessed on: 2023 Jun 14]
56. Crespo AC, Dominguez JM, Barreiro A, Gómez-Gesteira M, and Rogers BD. GPUs, a New Tool of Acceleration in CFD: Efficiency and Reliability on Smoothed Particle Hydrodynamics Methods. PLoS ONE 2011 Jun; 6:e20685. DOI: 10.1371/journal.pone.0020685. Available from: https://www.ncbi.nlm.nih.gov/pmc/articles/PMC3113801/ [Accessed on: 2023 Jun 14]
57. Obrecht C, Kuznik F, Tourancheau B, and Roux JJ. Multi-GPU implementation of the lattice Boltzmann method. en. Computers & Mathematics with Applications. Special Issue on Mesoscopic Methods in Engineering and Science (ICMMES-2010, Edmonton, Canada) 2013 Jan; 65:252–61. DOI: 10.1016/j.camwa.2011.02.020. Available from: https://www.sciencedirect.com/science/article/pii/S0898122111001064 [Accessed on: 2023 Jun 14]
58. Olsson E and Kreiss G. A conservative level set method for two phase flow. en. Journal of Computational Physics 2005 Nov; 210:225–46. DOI: 10.1016/j.jcp.2005.04.007. Available from: https://www.sciencedirect.com/science/article/pii/S0021999105002184 [Accessed on: 2023 Jun 14]
59. Hua H, Shin J, and Kim J. Level Set, Phase-Field, and Immersed Boundary Methods for Two-Phase Fluid Flows. Journal of Fluids Engineering 2013 Nov; 136. DOI: 10.1115/1.4025658. Available from: https://doi.org/10.1115/1.4025658 [Accessed on: 2023 Jun 15]
60. Berthier J, Gosselin D, Pham A, Boizot F, Delapierre G, Belgacem N, and Chaussy D. Spontaneous capillary flows in piecewise varying cross section microchannels. en. Sensors and Actuators B: Chemical 2016 Feb; 223:868–77. DOI: 10.1016/j.snb.2015.10.023. Available from: https://www.sciencedirect.com/science/article/pii/S0925400515304895 [Accessed on: 2023 May 3]
61. Walker S and Shapiro B. Modeling the Fluid Dynamics of Electrowetting on Dielectric (EWOD). en. Journal of Microelectromechanical Systems 2006 Aug;

15:986–1000. DOI: 10.1109/JMEMS.2006.878876. Available from: http://ieeexplore.ieee.org/document/1668195/ [Accessed on: 2023 May 8]
62. OpenFOAM: API Guide: alphaContactAngleTwoPhaseFvPatchScalarField Class Reference. Available from: https://www.openfoam.com/documentation/guides/latest/api/classFoam_1_1alphaContactAngleTwoPhaseFvPatchScalarField.html [Accessed on: 2023 Jun 16]
63. OpenFOAM: API Guide: src/finiteVolume/cfdTools/general/levelSet Directory Reference. Available from: https://www.openfoam.com/documentation/guides/latest/api/dir_057e4865767d08d37202aa1080d029d3.html [Accessed on: 2023 Jun 16]
64. ANSYS FLUENT 12.0 Theory Guide - 16.3.8 Surface Tension and Wall Adhesion. Available from: https://www.afs.enea.it/project/neptunius/docs/fluent/html/th/node305.htm [Accessed on: 2023 Jun 16]
65. Two-Phase Flow Modeling Guidelines. en. Available from: https://www.comsol.com/support/learning-center/article/Two-Phase-Flow-Modeling-Guidelines-59411 [Accessed on: 2023 Jun 16]
66. Siegel R. Transient Capillary Rise in Reduced and Zero-Gravity Fields. Journal of Applied Mechanics 1961 Jun; 28:165–70. DOI: 10.1115/1.3641647. Available from: https://doi.org/10.1115/1.3641647 [Accessed on: 2023 Jun 25]
67. Young WB. Analysis of capillary flows in non-uniform cross-sectional capillaries. en. Colloids and Surfaces A: Physicochemical and Engineering Aspects 2004 Feb; 234:123–8. DOI: 10.1016/j.colsurfa.2003.12.007. Available from: https://www.sciencedirect.com/science/article/pii/S0927775703006800 [Accessed on: 2023 Jun 25]
68. Naydich YV, Gab II, Evdokimov VA, Kurkova DI, and Stetsyuk T. Shape of a Liquid Surface and Capillary Phenomena under Reduced or Zero Gravity. en. Powder Metallurgy and Metal Ceramics 2004 Mar; 43:170–8. DOI: 10.1023/B:PMMC.0000035706.34256.78. Available from: https://doi.org/10.1023/B:PMMC.0000035706.34256.78 [Accessed on: 2023 Jun 25]
69. Çengel Y and Cimbala J. Fluid Mechanics: Fundamentals and Applications. 4th. McGraw-Hill Education, 2019
70. Zdziennicka A, Szymczyk K, Krawczyk J, and Jańczuk B. Some remarks on the solid surface tension determination from contact angle measurements. en. Applied Surface Science 2017 May; 405:88–101. DOI: 10.1016/j.apsusc.2017.01.068. Available from: https://www.sciencedirect.com/science/article/pii/S0169433217300685 [Accessed on: 2023 Jun 16]
71. Ryan BJ and Poduska KM. Roughness effects on contact angle measurements — American Journal of Physics — AIP Publishing. 2008. Available from: https://pubs.aip.org/aapt/ajp/article/76/11/1074/1042354/Roughness-effects-on-contact-angle-measurements [Accessed on: 2023 Jun 16]
72. ImageJ. Available from: https://imagej.nih.gov/ij/ [Accessed on: 2023 Jun 17]
73. Wang J, Wu Y, Cao Y, Li G, and Liao Y. Influence of surface roughness on contact angle hysteresis and spreading work. en. Colloid and Polymer Science 2020 Aug; 298:1107–12. DOI: 10.1007/s00396-020-04680-x. Available from: https://doi.org/10.1007/s00396-020-04680-x [Accessed on: 2023 Jun 21]

74. Zhu Y and Petkovic-Duran K. Capillary flow in microchannels. en. Microfluidics and Nanofluidics 2010 Feb; 8:275–82. DOI: 10.1007/s10404-009-0516-4. Available from: https://doi.org/10.1007/s10404-009-0516-4 [Accessed on: 2023 Jun 21]
75. Mukhopadhyay S, Banerjee JP, and Roy SS. Effects of liquid viscosity, surface wettability and channel geometry on capillary flow in SU8 based microfluidic devices. en. International Journal of Adhesion and Adhesives 2013 Apr; 42:30–5. DOI: 10.1016/j.ijadhadh.2012.12.001. Available from: https://www.sciencedirect.com/science/article/pii/S014374961200187X [Accessed on: 2023 Jun 21]
76. Kung CH, Sow PK, Zahiri B, and Mérida W. Assessment and Interpretation of Surface Wettability Based on Sessile Droplet Contact Angle Measurement: Challenges and Opportunities. en. Advanced Materials Interfaces 2019; 6. _eprint: https://onlinelibrary.wiley.com/doi/pdf/10.1002/admi.201900839:1900839. DOI: 10.1002/admi.201900839. Available from: https://onlinelibrary.wiley.com/doi/abs/10.1002/admi.201900839 [Accessed on: 2023 Jun 22]
77. Gorce JB, Hewitt IJ, and Vella D. Capillary Imbibition into Converging Tubes: Beating Washburn's Law and the Optimal Imbibition of Liquids. Langmuir 2016 Feb; 32. Publisher: American Chemical Society:1560–7. DOI: 10.1021/acs.langmuir.5b04495. Available from: https://doi.org/10.1021/acs.langmuir.5b04495 [Accessed on: 2023 Jun 25]

A Numerical Results

A.1 Droplet Young-Laplace Derivation

Following is a rough derivation of the Young-Laplace equation for axisymmetric droplets.

Force equilibrium in the z-direction for an axisymmetric droplet

$$\sum F_z = 0 = -dF_g(r) + F_p(r+dr) - F_p(r) + F_\sigma(r)\sin(\theta) - F_\sigma(r+dr)\sin(\theta+d\theta) - p_g 2\pi r dr \tag{A.1}$$

Where

$$dF_g(z) = \rho g \pi r^2 dz \tag{A.2}$$
$$F_p(z) = \rho g z(r) \pi r^2 \tag{A.3}$$
$$F_\sigma = \sigma_{lg} 2\pi r \tag{A.4}$$
$$p_g = \rho_g g z(r) + p_0 \approx p_0 \tag{A.5}$$

p_0 is the pressure at the top of the droplet in the center

Insert the relations above into the equilibrium and makes z dependent on r

$$\sum F_z = 0 \tag{A.6}$$
$$= -\rho g \pi r^2 dz + \rho g \pi z(r+dr)(r+dr)^2 - \rho g z(r)\pi r^2 + \sigma_{lg} 2\pi r \sin(\theta) \tag{A.7}$$
$$- \sigma_{lg} 2\pi (r+dr)\sin(\theta+d\theta) - p_0 2\pi r dr - \rho g z(0)\pi r^2 \tag{A.8}$$

Divide by $\pi\sigma_{lg}$ and set $C = \frac{\rho g}{\sigma_{lg}}$ and $C_p = \frac{p_0}{\sigma_{lg}}$

$$0 = -Cr^2 dz + Cz(r+dr)(r+dr)^2 - Cr^2 z(r) + 2r\sin(\theta) - 2(r+dr)\sin(\theta+d\theta) - 2C_p r dr \tag{A.9}$$

Relations for θ and $d\theta$

$$d\theta = \frac{\frac{d^2z}{dr^2}}{1+\left(\frac{dz}{dr}\right)^2} dr$$
$$\sin(\theta) = \frac{\frac{dz}{dr}}{\sqrt{1+\left(\frac{dz}{dr}\right)^2}}$$
$$\cos(\theta) = \frac{1}{\sqrt{1+\left(\frac{dz}{dr}\right)^2}}$$
$$\sin(\theta+d\theta) = \sin(\theta)\cos(d\theta) + \sin(d\theta)\cos(\theta) \approx \sin(\theta) + d\theta\cos(\theta)$$
$$\sin(\theta+d\theta) = \frac{\frac{dz}{dr}}{\sqrt{1+\left(\frac{dz}{dr}\right)^2}} + \frac{\frac{d^2z}{dr^2}dr}{\left[1+\left(\frac{dz}{dr}\right)^2\right]^{\frac{3}{2}}}$$

Inserts relations for θ and $d\theta$ into the equilibrium equation

$$0 = -Cr^2dz + Cz(r+dr)(r+dr)^2 - Cr^2z(r) + 2r\frac{\frac{dz}{dr}}{\sqrt{1+\left(\frac{dz}{dr}\right)^2}} \tag{A.10}$$

$$-2(r+dr)\left(\frac{\frac{dz}{dr}}{\sqrt{1+\left(\frac{dz}{dr}\right)^2}} + \frac{\frac{d^2z}{dr^2}dr}{\left[1+\left(\frac{dz}{dr}\right)^2\right]^{\frac{3}{2}}}\right) - 2C_prdr \tag{A.11}$$

Divides the equilibrium by dr

$$0 = -Cr^2\frac{dz}{dr} + \frac{Cz(r+dr)(r+dr)^2 - Cr^2z(r)}{dr} - 2\left(\frac{\frac{dz}{dr}}{\sqrt{1+\left(\frac{dz}{dr}\right)^2}} + \frac{\frac{d^2z}{dr^2}r}{\left[1+\left(\frac{dz}{dr}\right)^2\right]^{\frac{3}{2}}}\right) - 2C_pr \tag{A.12}$$

Definition of derivation

$$f'(x) = \lim_{h\to 0}\frac{f(x+h)-f(x)}{h} \tag{A.13}$$

Uses the definition of derivation in the equilibrium for the second term

$$0 = -Cr^2\frac{dz}{dr} + C\frac{d}{dr}(z(r)r^2) - 2\left(\frac{\frac{dz}{dr}}{\sqrt{1+\left(\frac{dz}{dr}\right)^2}} + \frac{\frac{d^2z}{dr^2}r}{\left[1+\left(\frac{dz}{dr}\right)^2\right]^{\frac{3}{2}}}\right) - 2C_pr \tag{A.14}$$

$$0 = -Cr^2\frac{dz}{dr} + C\left(\frac{dz}{dr}r^2 + 2rz(r)\right) - 2\left(\frac{\frac{dz}{dr}}{\sqrt{1+\left(\frac{dz}{dr}\right)^2}} + \frac{\frac{d^2z}{dr^2}r}{\left[1+\left(\frac{dz}{dr}\right)^2\right]^{\frac{3}{2}}}\right) - 2C_pr \tag{A.15}$$

$$0 = 2r(Cz(r) - C_p) - 2\left(\frac{\frac{dz}{dr}}{\sqrt{1+\left(\frac{dz}{dr}\right)^2}} + \frac{\frac{d^2z}{dr^2}r}{\left[1+\left(\frac{dz}{dr}\right)^2\right]^{\frac{3}{2}}}\right) \tag{A.16}$$

Divides by $2r$

$$0 = Cz(r) - C_p - \left(\frac{\frac{dz}{dr}}{r\sqrt{1 + \left(\frac{dz}{dr}\right)^2}} + \frac{\frac{d^2z}{dr^2}}{\left[1 + \left(\frac{dz}{dr}\right)^2\right]^{\frac{3}{2}}} \right) \tag{A.17}$$

Reinserts for $C = \frac{\rho g}{\sigma_{lg}}$ and $C_p = \frac{p_0}{\sigma_{lg}}$

$$p_0 - \rho g z(r) = -\sigma_{lg} \left(\frac{\frac{dz}{dr}}{r\sqrt{1 + \left(\frac{dz}{dr}\right)^2}} + \frac{\frac{d^2z}{dr^2}}{\left[1 + \left(\frac{dz}{dr}\right)^2\right]^{\frac{3}{2}}} \right) \tag{A.18}$$

Note that the equation should be

$$p_0 - \rho g(z(0) - z(r)) = -\sigma_{lg} \left(\frac{\frac{dz}{dr}}{r\sqrt{1 + \left(\frac{dz}{dr}\right)^2}} + \frac{\frac{d^2z}{dr^2}}{\left[1 + \left(\frac{dz}{dr}\right)^2\right]^{\frac{3}{2}}} \right) \tag{A.19}$$

Since the hydrostatic pressure is 0 at the top of the droplet center This is most likely due to an error in the definition of the hydrostatic pressure in the equation (A.5), and it should be

$$F_p(z) = \rho g(z(r) - z(0))\pi r^2 \tag{A.20}$$

This would likely give the right equation since $z(0)$ is constant, but there was limited time to correct the mistake.

To solve this numerically, the equation is solved for $\frac{d^2z}{dr^2}$:

$$\frac{\frac{d^2z}{dr^2}}{\left[1 + \left(\frac{dz}{dr}\right)^2\right]^{\frac{3}{2}}} = \frac{\rho g}{\sigma_{lg}}(z(r) - z(0)) - \frac{p_0}{\sigma_{lg}} - \frac{\frac{dz}{dr}}{r\sqrt{1 + \left(\frac{dz}{dr}\right)^2}} \tag{A.21}$$

$$\frac{d^2z}{dr^2} = \left[\frac{\rho g}{(\sigma_{lg}}(z(r) - z(0)) - \frac{p_0}{\sigma_{lg}})\sqrt{1 + \left(\frac{dz}{dr}\right)^2} - \frac{\frac{dz}{dr}}{r} \right] \left[1 + \left(\frac{dz}{dr}\right)^2\right] \tag{A.22}$$

A.2 Validation

Figure A.1 shows a geometry of a funnel with water starting at the top. This was also used for validation, but only for 2D since it did not always converge for 3D.

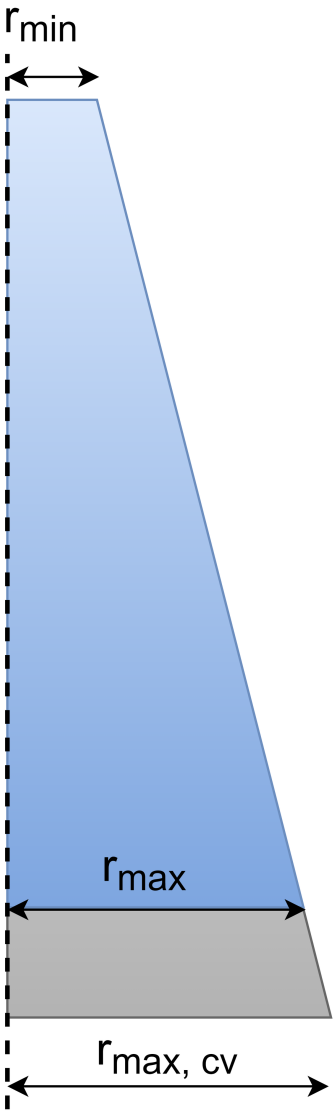

Figure A.1: The geometry of top funnel.

A.2.1 γ and χ parameter study

A parameter analysis was conducted to examine the effects of γ and χ for the Level-Set and Phase-Field methods, respectively. The study was performed using an axisymmetric cylinder with an initial volume of $1\,\mathrm{mm}^3$ and a wall contact angle, θ_W, of 70°.

Impact of γ: The parameter γ had a notable effect on diffusion, as depicted in Figure A.2. As γ increased, the rate of convergence also increased. A value of $1\,\mathrm{mm/s}$ for γ was selected to strike a balance between minimizing numerical diffusion and achieving a reasonable rate of convergence.

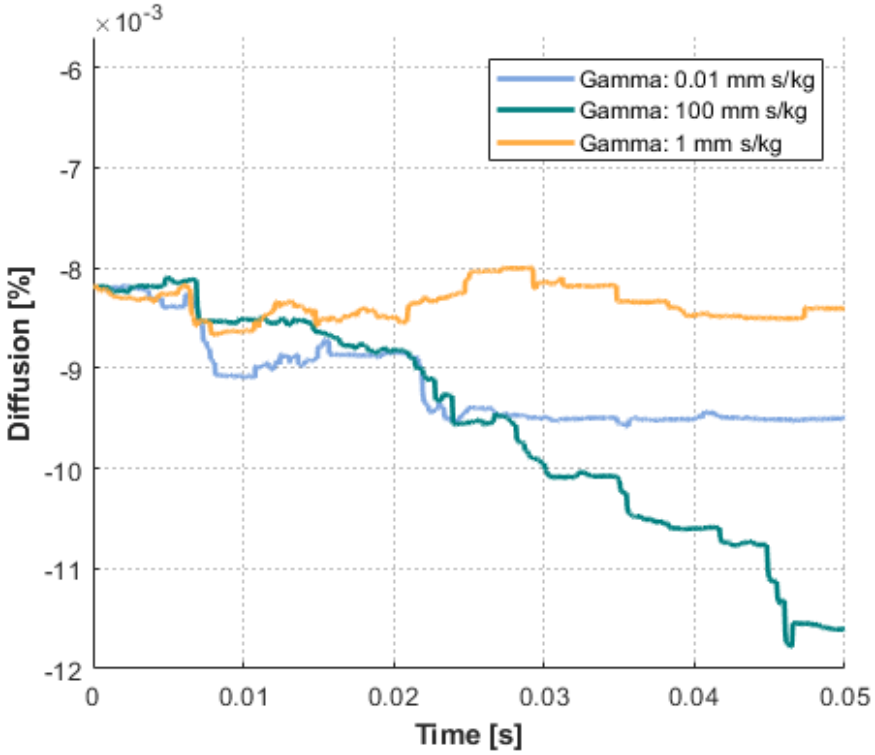

Figure A.2: The graph represents the percentage of water volume diffused over time in an axisymmetric cylinder with an initial volume of $1\,\mathrm{mm}^3$ and a wall contact angle of 70°. Some volume is always lost during phase initialization due to the coarseness of the meshes, preventing them from starting with the specified volume of water. Diffusion is calculated by integrating the volume fraction over all elements' surfaces and normalizing it by the initial volume.

Impact of χ: Contrarily, variations in the χ parameter did not yield any discernible differences, as demonstrated in Figure A.3. Therefore, a value of 1 mms/kg was chosen for χ.

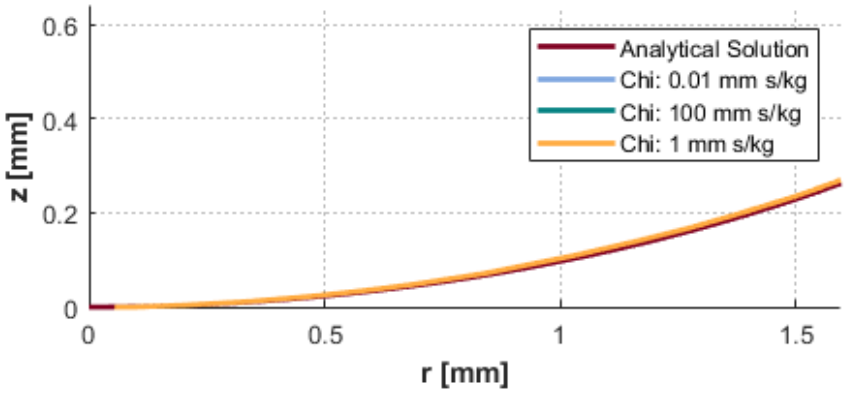

Figure A.3: The graph depicts the interface curve between the phases in an axisymmetric cylinder. The simulation utilized 1 mm^3 volume of water with a wall contact angle, θ_W, of 70°. The various curves represent different values of χ, showing that the choice of χ does not significantly affect the interface curve.

A.2.2 More diffusion plots

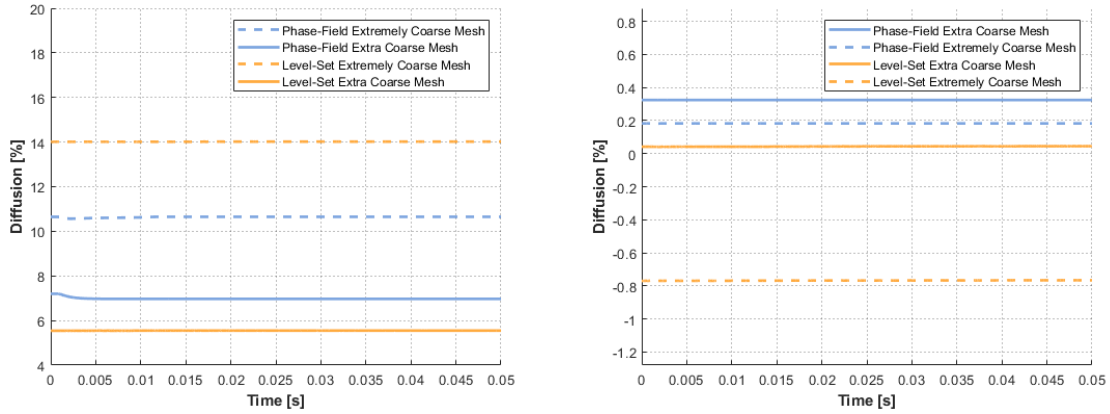

(a) (b)

Figure A.4: The percentage of the volume of water diffused over time for axisymmetric droplet (a) and funnel with water starting at the top (b). The simulations had an initial volume $1\,\mathrm{mm}^3$ and $\theta_W = 70°$. Some volume is always lost to the phase initialization since the meshes are too coarse to start with the given volume of water. The diffusion is calculated by surface integrating the volume fraction over all elements and dividing by the initial volume.

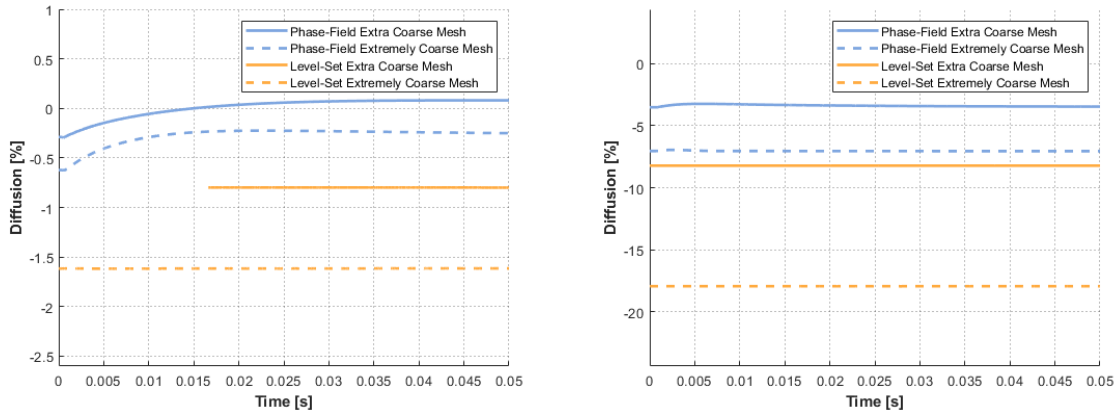

(a) (b)

Figure A.5: The percentage of the volume of water diffused over time for a funnel with water starting at the bottom. (a) is 2D axisymmetric, while (b) is a 3D simulation. The simulations had an initial volume $1\,\mathrm{mm}^3$ and $\theta_W = 70°$. Some volume is always lost to the phase initialization since the meshes are too coarse to start with the given volume of water. The diffusion is calculated by surface integrating the volume fraction over all elements and dividing by the initial volume. In (a) the initial data of all parameters of the "Level-Set Extremely Coarse Mesh" simulation were not saved by COMSOL, possibly due to too many iterations.

A.2.3 More surface curve plots

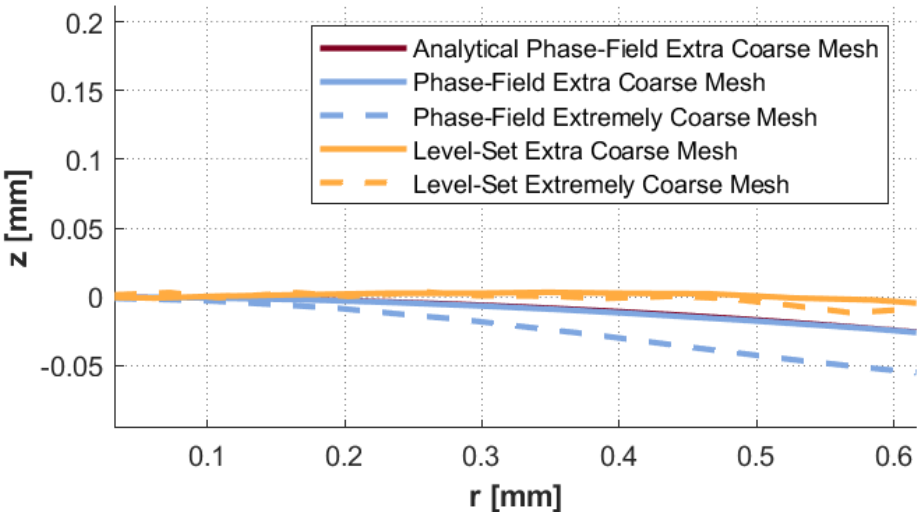

Figure A.6: The interface curve between the phases in an axisymmetric funnel with water at the top is shown in figure A.1. The simulation used $1\,\mathrm{mm}^3$ volume of water and $\theta_W = 70°$. The analytical is calculated by solving the axisymmetric version of the Young-Laplace equation 3.9 with the boundary condition $z'(r_{funnel}) = -\tan(90 - \theta_W - \alpha)$.

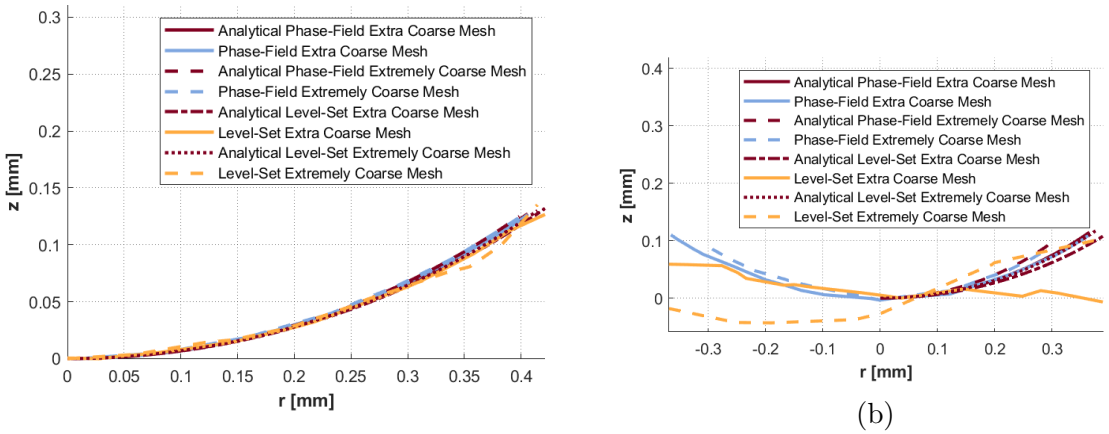

(a) (b)

Figure A.7: The interface curve between the phases in a funnel with water starting at the bottom. (a) is 2D axisymmetric, while (b) is a 3D simulation. The simulations had an initial volume $1\,\mathrm{mm}^3$ and $\theta_W = 70°$. The simulations used $1\,\mathrm{mm}^3$ volume of water and $\theta_W = 70°$. The analytical is calculated by solving the axisymmetric version of the Young-Laplace equation 3.9 with the boundary condition $z'(r_{funnel}) = \tan(90 - \theta_W + \alpha)$.

A.2.4 More pressure plots

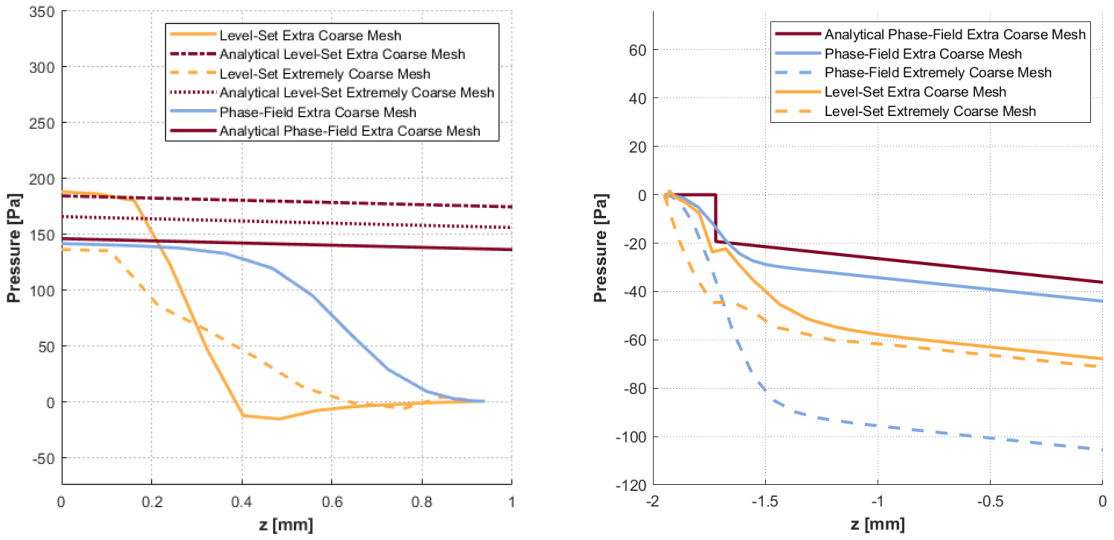

(a) (b)

Figure A.8: The pressure along the centerline for axisymmetric droplet (a) and funnel with water starting at the top (b). The simulations had an initial volume 1 mm^3 and $\theta_W = 70°$. The analytical pressure difference in the interface is calculated from the curvature.

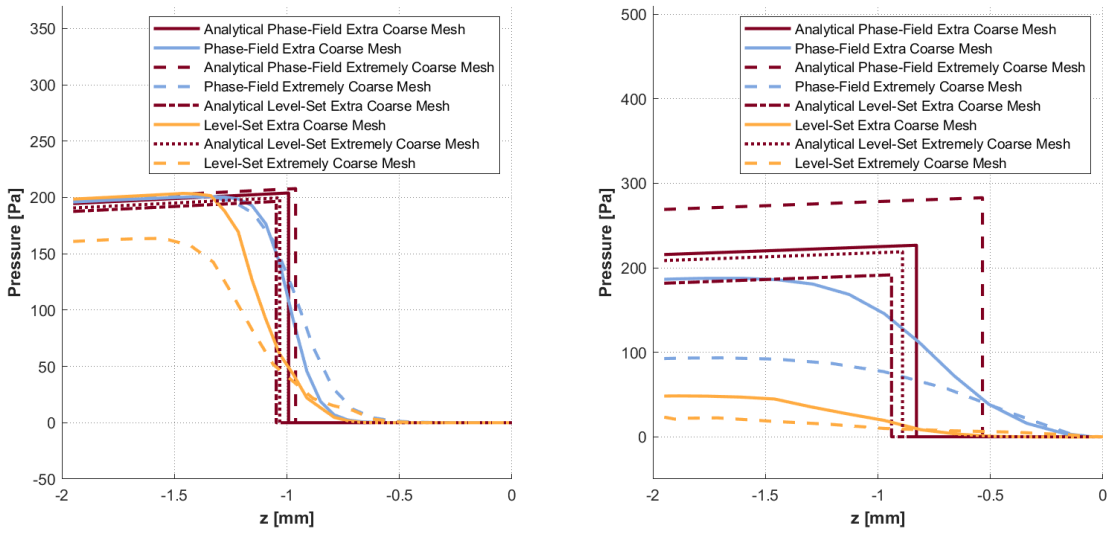

(a) (b)

Figure A.9: The pressure along the centerline for a funnel with water starting at the bottom. (a) is 2D axisymmetric, while (b) is a 3D simulation. The simulations had an initial volume 1 mm^3 and $\theta_W = 70°$. The simulations used 1 mm^3 volume of water and $\theta_W = 70°$. The analytical pressure difference in the interface is calculated from the curvature.

A.3 Flow Simulations

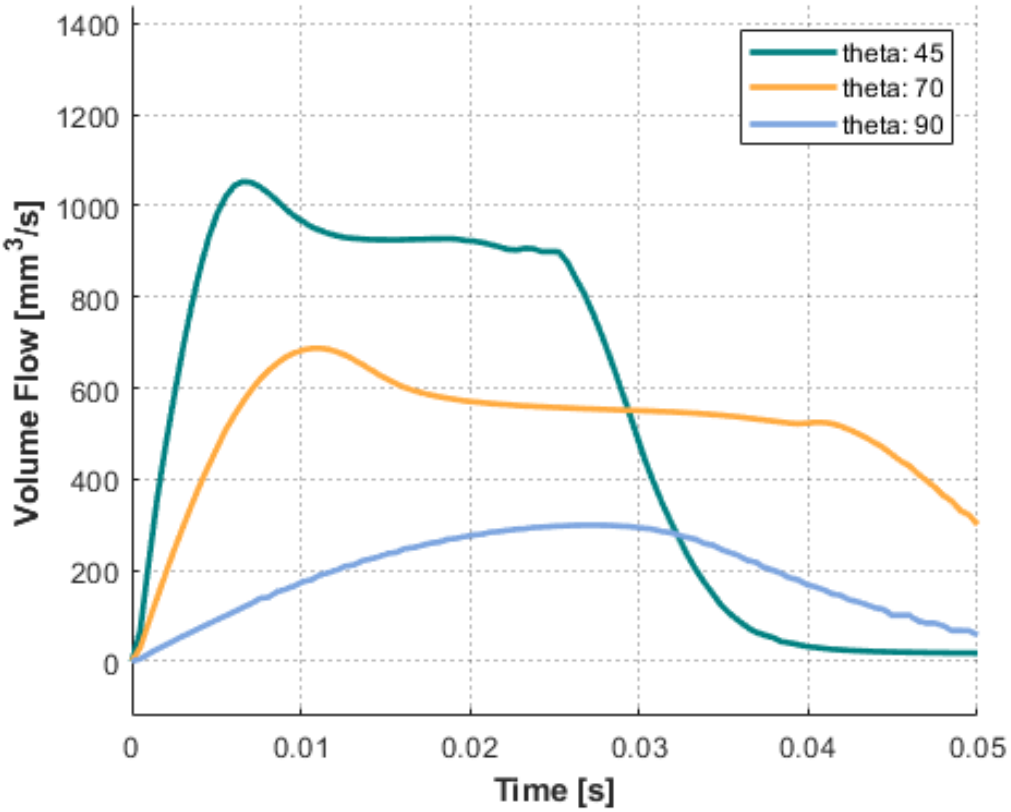

Figure A.10: The volumetric flow rate of the water in and out of the control volume for different contact angles and α. The depth is 1 mm, and no gravity is applied.

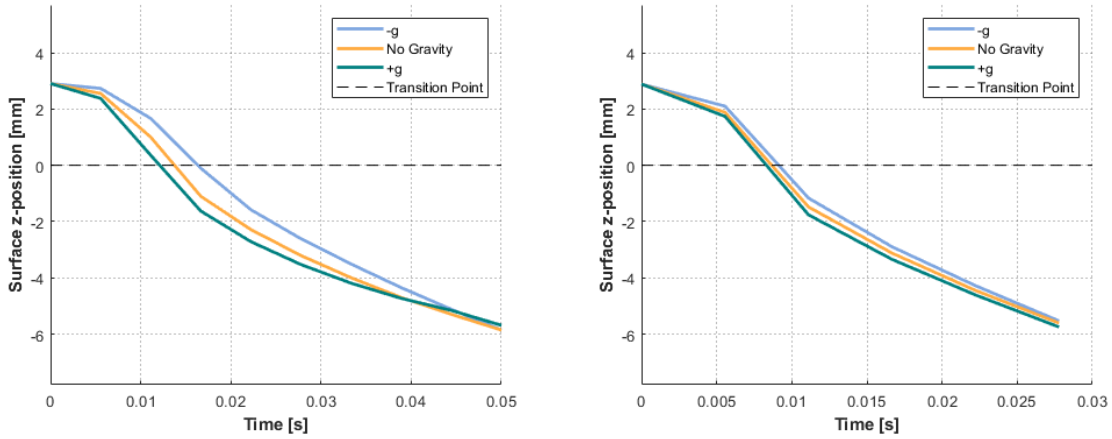

(a) (b)

Figure A.11: The phase interface in the centerline affected by gravity. The contact angle is 70° for (a) and 45° for (b). The depth is1 mm and $\alpha = 20°$. The phase interface surface is obtained by finding where the phase-field parameter (Φ) is 0 by interpolation.

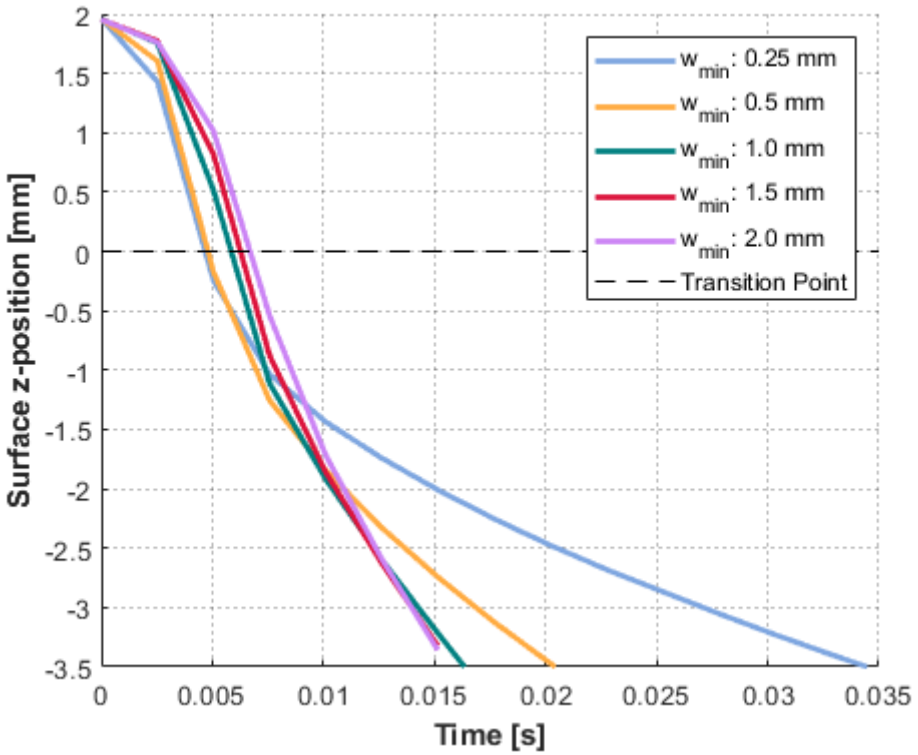

Figure A.12: The phase interface in the centerline for varying w_{min}. The depth is1 mm, the contact angle is 45°, and the gravity is pointing down. The phase interface surface is obtained by finding where the phase-field parameter (Φ) is 0 by interpolation.

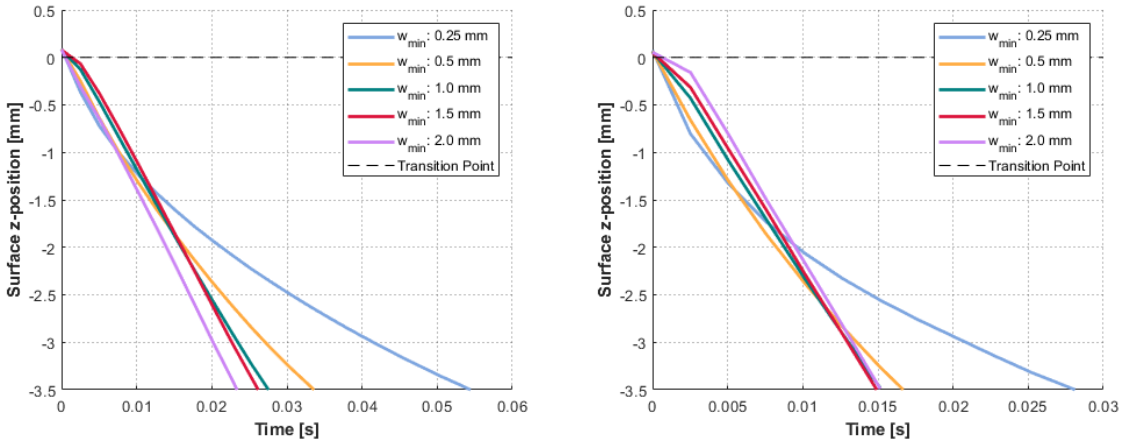

(a) (b)

Figure A.13: The phase interface in the centerline for varying w_{min} for a lower starting point. The contact angle is 70° for (a) and 45° for (b). The depth is1 mm, $\alpha = 20°$, and the gravity is pointing down with the flow. The phase interface surface is obtained by finding where the phase-field parameter (Φ) is 0 by interpolation.

B Scripts

B.1 Calculating and plotting hourglass concept

Hourglass_summarized.ipynb

```
import numpy as np
import matplotlib.pyplot as plt
from scipy import optimize as opt

# Definition of physical constants and input parameters
V = 20 * 10**(-9) # m^3
t = 1 * 10**(-3) # m
r = 1 * 10**(-3) # m
sigma_lg = 0.0728 # N/m
rho = 998.23 # kg/m^3
g = 9.81 # m/s^2

# Define given angles (alpha, beta, theta_W, theta_d) and convert to radians
alpha_deg = 10 # deg
alpha_rad = alpha_deg * np.pi / 180 # rad

beta_deg = 20 # deg
beta_rad = beta_deg * np.pi / 180 # rad

theta_y_deg = 60 #deg
theta_y_rad = theta_y_deg * np.pi / 180 # rad

theta_x_deg = 20 # deg
theta_x_rad = theta_x_deg * np.pi / 180 # rad

# Cylinder segment volume function
def cylvol(angle):
    return (np.pi - 2 * (theta_y_rad + angle) - np.sin(2 * (theta_y_rad + angle)))/(2 * (np.cos(theta_y_rad + angle))**2)

# Define function from equation set
def f(r1):
    r2 = np.sqrt((-(r1**2 - r**2)/(np.tan(alpha_rad)) + r**2/(np.tan(beta_rad)) + cylvol(alpha_rad) * r1**2 + V/t)/(1 / np.tan(beta_rad) - cylvol(beta_rad)))
    return - rho * g * V + 2 * t * sigma_lg * (r2 / r1 * np.cos(theta_y_rad + alpha_rad) - r1 / r2 * np.cos(theta_y_rad + beta_rad)) + 2 * t * sigma_lg * (r2 / r1 * np.cos(theta_y_rad + alpha_rad) - r1 / r2 * np.cos(theta_y_rad +
```

```
      ↪beta_rad) + (2 * np.cos(theta_x_rad) / t * (r2 - r1)))
34
35 r1 = np.linspace(r, 4 * 10**(-3), 500)
36
37 # Plot function f(r1)
38 plt.plot(r1, f(r1))
39 plt.xlabel('r1')
40 plt.ylabel('f(r1)')
41 plt.plot(r1, np.zeros(len(r1)), 'r--')
42 # Try to find intersection point where f(r1)=0 and plot it
43 try:
44     r1_intersect = opt.fsolve(f, 1 * 10**(-3))
45     plt.plot(r1_intersect, f(r1_intersect), 'ro')
46     plt.text(r1_intersect, f(r1_intersect), 'r1 = ' + str(
       ↪r1_intersect))
47 except:
48     print('No intersection point found')
49 plt.show()
50
51 # Define function which calculates r2 from r1
52 def find_r2(r1):
53     return np.sqrt((-(r1**2 - r**2)/(np.tan(alpha_rad)) + r**2/(
       ↪np.tan(beta_rad)) + (np.pi - 2 * (theta_y_rad + alpha_rad)
       ↪ - np.sin(2 * (theta_y_rad + alpha_rad)))/(2 * (np.cos(
       ↪theta_y_rad + alpha_rad))**2) * r1**2 + V/t)/(1 / np.tan(
       ↪beta_rad) - (np.pi - 2 * (theta_y_rad + beta_rad) - np.sin
       ↪(2 * (theta_y_rad + beta_rad)))/(2 * (np.cos(theta_y_rad +
       ↪ alpha_rad))**2)))
54
55 r2 = find_r2(r1_intersect)
56 print('r2 = ' + str(r2))
57
58 # Calculate height of liquid in converging and diverging part of
     ↪hourglass
59 h1 = (r1_intersect - r) / np.tan(alpha_rad)
60 h2 = (r2 - r) / np.tan(beta_rad)
61 h = h1 + h2
62
63 # Calculate radius of curvature of liquid surface in converging
     ↪and diverging part of hourglass
64 R1 = r1_intersect / np.cos(theta_y_rad + alpha_rad)
65 R2 = r2 / np.cos(theta_y_rad + beta_rad)
66
67 # plot hourglass
68 plt.figure()
69 plt.plot([r1_intersect, r], [h1, 0], color='#666666', linewidth
     ↪=3.0)
70 plt.plot([r2, r], [-h2, 0], color='#666666', linewidth=3.0)
71 plt.plot([-r1_intersect, -r], [h1, 0], color='#666666', linewidth
     ↪=3.0)
72 plt.plot([-r2, -r], [-h2, 0], color='#666666', linewidth=3.0)
```

```
plt.gca().set_aspect('equal', adjustable='box')
plt.gcf().set_size_inches(10, 10)

# plot liquid surface of in plane curvature

u1_vec = np.linspace(-1, 1, 100)
r1_vec = r1_intersect * u1_vec
plt.plot(r1_vec, -np.sqrt(R1**2 - r1_vec**2) + r1_intersect * np.tan(theta_y_rad + alpha_rad) + h1, color='#7EA6E0', linewidth=3.0)

u2_vec = np.linspace(-1, 1, 100)
r2_vec = r2 * u1_vec
plt.plot(r2_vec, np.sqrt(R2**2 - r2_vec**2) - r2 * np.tan(theta_y_rad + beta_rad) - h2, color='#7EA6E0', linewidth=3.0)

jump = r2 + 0.0005

plt.hlines(0, jump, jump + t, color='#666666', linestyles='solid', linewidth=3.0)
plt.vlines(jump, h1, -h2, color='#666666', linestyles='solid', linewidth=3.0)
plt.vlines(jump + t, h1, -h2, color='#666666', linestyles='solid', linewidth=3.0)

# Calculate and plot out of plane curvature
R3 = t/2 / np.cos(theta_x_rad)

u3_vec = np.linspace(-1, 1, 100)
r3_vec = t/2 * u3_vec + jump + t/2

plt.plot(r3_vec, -np.sqrt(R3**2 - (r3_vec - jump - t/2)**2) + t/2 * np.tan(theta_x_rad) + h1, color='#7EA6E0', linewidth=3.0)
plt.plot(r3_vec, np.sqrt(R3**2 - (r3_vec - jump - t/2)**2) - t/2 * np.tan(theta_x_rad) - h2, color='#7EA6E0', linewidth=3.0)

plt.xlabel('Width W and depth d [m]', fontsize=16)
plt.ylabel('Height h [m]', fontsize=16)

plt.tick_params(axis='both', which='major', labelsize=16)

plt.show()

# Print Ouput parameters

print( 'Volume = ' + str(V))
print('Thickness t = ' + str(t))
print('h1 = ' + str(h1))
print( 'h2 = ' + str(h2))
print( 'h = ' + str(h))
print( 'alpha_deg = ' + str(alpha_deg))
```

```
116 print( 'beta_deg = ' + str(beta_deg))
117 print( 'r1_intersect = ' + str(r1_intersect))
118 print( 'r2 = ' + str(r2))
119 print('r = ' + str(r))
120
121 print( 'W1 = ' + str(2*r1_intersect))
122 print( 'W2 = ' + str(2*r2))
123 print( 'W_min = ' + str(2*r))
124
125 volume_top = t* ((r1_intersect**2 - r**2) / np.tan(alpha_rad) - (
      ↪np.pi - 2 * (theta_y_rad + alpha_rad) - np.sin(2*(theta_y_rad+
      ↪alpha_rad))) * r1_intersect**2/(2*(np.cos(theta_y_rad+
      ↪alpha_rad))**2))
126
127 volume_bottom = t* ((r2**2 - r**2) / np.tan(beta_rad) - (np.pi -
      ↪2 * (theta_y_rad + beta_rad) - np.sin(2*(theta_y_rad+beta_rad)
      ↪)) * r2**2/(2*(np.cos(theta_y_rad+beta_rad))**2))
128
129 volume_total = volume_top + volume_bottom
130
131
132 frac = volume_top / volume_total
133 print('Volume fraction above transition point = ' + str(frac))
```

B.2 Calculcating the surface curve analytically

surface_curvature_theoretical.m

```
% This function calculates the surface curvature of a water
% surface as a function of the contact angle and maximum radius.
function [r, z, K] = surface_curvature_theoretical(theta, r_max)

% Define the radial mesh points
r_mesh = linspace(0.00001, r_max, 100);

% Define initial guess for the boundary value problem
solinit = bvpinit(r_mesh, @guess);

% Solve the boundary value problem using a collocation method
sol_curve = bvp4c(@bvp_fun, bc_fun(theta), solinit);

% Evaluate the solution at the mesh points
sol_z = deval(sol_curve, r_mesh);

% Adjust the solution so that z(r_max) = 0
sol_z(1,:) = sol_z(1, :) - sol_z(1, end);

% Define r and z based on the solution
r = r_mesh;
z = sol_z(1,:);

% Compute the first derivative of z with respect to r
dz_dr = sol_z(2,:);

% Compute the second derivative of z with respect to r
d2z_dr2 = diff(dz_dr) ./ diff(r);

% Compute the midpoints for second derivative
r_mid = (r(1:end-1) + r(2:end)) / 2;

K1 = -interp1(r, dz_dr, r_mid, 'linear', 'extrap') ./ (r_mid .*
  ↪sqrt(1 + interp1(r, dz_dr, r_mid, 'linear', 'extrap').^2));

K2 = -d2z_dr2 ./ (1 + interp1(r, dz_dr, r_mid, 'linear', 'extrap'
  ↪).^2).^(3/2);

% Compute the mean curvature
K = (K1 + K2)/2;

% Interpolate curvature values at original r positions
K = interp1(r_mid, K, r, 'linear', 'extrap');

end

% Define the differential equations for the boundary value
  ↪problem
```

```
function dydx = bvp_fun(x, y)
rho = 997e-9;         % Density of the liquid in g/mm^3
g = 9810;             % Gravitational acceleration in mm/s^2
sigma_lg = 7.28e-5;   % Surface tension coefficient in N/mm

C = rho * g / sigma_lg;

r = x;
z = y(1);
dzdr = y(2);

% Compute the second derivative of z with respect to r
d2zdr2 = (C * (r * dzdr + z) * sqrt(1 + dzdr^2) - dzdr/r) * (1 +
  ↪dzdr^2);

% Return the derivatives
dydx = [dzdr, d2zdr2];
end

% Define the boundary conditions function handle
function bc_handle = bc_fun(theta)

% Define the residual function for boundary conditions
function res = bc(ya, yb)
    left_neumann = ya(2);
    right_neumann = yb(2) - tan(deg2rad(theta));
    res = [left_neumann, right_neumann];
end

% Return the handle to the boundary conditions function
bc_handle = @bc;
end

% Define an initial guess for the solution
function y = guess(x)
y = [x, x^2];
end
```

B.3 Calculcating the pressure along the z-axis analytically

pressure_theoretical.m

```
% Computes the theoretical pressure along the z-axis based on
% the mean curvature provided as input from
% "surface_curvature_theoretical.m".
function p = pressure_theoretical(K_mean)
rho = 997;
g = 9.81;
sigma_lg = 0.0728;

function p = pressure(z)
    z_m = z/1000; % converting z from mm to m
    K_mean_m = K_mean*1000; % converting K_mean from 1/mm to 1/m

    p = -2*sigma_lg*K_mean_m - rho * g * z_m;
end

p = @pressure;
end
```

C Data Sheets

C.1 Hydrophilic film for EBC condensation

3M Science. Applied to Life.™

Medical Materials & Technologies

3M™ 9960 Diagnostic Microfluidic Hydrophilic Film

Product Description:
3M™ 9960 diagnostic hydrophilic film consists of a clear polyester film on a roll coated on two sides with a 3M hydrophilic technology. The hydrophilic treatment is the same on both sides of the film. The product is designed for use in health care medical devices such as test strip and lab-on-a-chip applications.

Features and Benefits:

- Hydrophilic
- Transparent
- Non-hemolytic
- Low Autofluorescence
- Non-toxic to mammalian cells
- No significant outgassing < 400 ºC
- Dimensionally stable
- Anti-fogging properties

Composition: 

6.8 ± 0.25 mils (0.17 ± 0.01 mm) Transparent polyester with 3M proprietary hydrophilic treatment, both sides

Product Properties:

Wet Index	Minimum 36
Light Transmission	91% at 700 nm; 85% at 400 nm (typical)
Heat Shrinkage	Maximum - 1.3% - MD & CD [150 °C for 15 minutes]
Break Strength (Tensile)	Minimum - 131.0 lb/in (59.4 kg/25.4 mm) (582.7 N/25.4 mm) - MD Minimum - 164.0 lb/in (74.4 kg/25.4 mm) (729.5 N/25.4 mm) - CD
Break Elongation	Minimum - 70% - MD; 47% - CD
Autofluorescence	Minimal at Emissions: 400-800 nm / Excitations: >400 nm

Roll Description:

Roll Length	Maximum 1600 yd (1463 m) ± 2%
Roll Width	Minimum 2 in (51 mm); Maximum 49 in (124.5 cm) ± 0.125 in (3.2 mm)
Splices per Roll	Maximum 1 every 500 yd (457 m); up to 4 per 1600 yd (1463 m)

Note: Core options are fiber or plastic 3-in (76 mm) and 6-in (152 mm) diameter.
Core material and diameter must be specified in special instructions of order set.

Recommended Storage Conditions & Shelf Life:

Product as supplied in original packaging will maintain stated properties for a period of 14 months from date of manufacture when stored at room temperature 68-77 ºF (20-25 ºC).

When not in use, keep product wrapped in moisture impervious barrier and avoid excessive heat and humidity.

Please see reverse side for important product, safety and warranty information.

Product and Safety Information: User is solely responsible for determining the suitability of 3M samples and products for the intended use including any necessary safety or toxicity assessment. 3M will provide Material Safety Data Sheets or equivalent and summary results of toxicity testing upon request. In every case before using any product in full scale production users should conduct their own tests to determine to their own satisfaction whether the product is of acceptable quality and is suitable for their particular purposes under their own operating conditions.
Notice: Nothing contained herein shall be construed to imply the nonexistence of any relevant patents or to constitute a permission, inducement or recommendations to practice any invention covered by any patent, without authority from the owners of this patent.

Warranty Information
All statements, technical information and recommendations herein are based on tests 3M believes to be reliable, but the accuracy or completeness thereof is not guaranteed. 3M warrants only that products will meet 3M's specifications at the time of shipment to the customer. 3M does not offer any other warranty and does not warrant the performance, safety or such other characteristics of products in combination with other materials. 3M specifically DOES NOT warrant products for any intended or unintended uses (whether or not foreseeable); for compatibility or suitability with other components or compatibility with any methods of manufacture or conversion. The foregoing warranty is made in lieu of all other warranties, expressed or implied, including the implied warranties of merchantability, fitness for a particular purpose and freedom from non-infringement.

Limitation of Remedies: If products are proven not to meet 3M's specifications, the sole and exclusive remedy available and 3M's only obligation shall be, at 3M's option, to replace such quantity of Products which are proven out of specification or to refund the purchase price paid for Products.

Limitations of Liabilities: The remedies provided herein are exclusive remedies against 3M for any alleged or actual nonconformance to specifications or defect or other failure in products or for 3M's performance of its supply obligations. Under no circumstances is 3M liable for any direct, indirect, incidental, special or consequential damages (including lost profits) in any way related to the product under any theory of law including, but not limited to, negligence and strict liability.

Ordering Information

To place an order, call our Customer Service at: 800-742-1994 (U.S.). For all orders outside the United States, please contact your local country representative or check out 3M.com/MedTechFindaRep for your region's contact information.

To have a sales representative contact you, to request samples or clinical and safety summaries, please contact us at 3M HELPLINE 800-228-3957 (U.S.) or check out 3M.com/MedTechContactUs for your region's contact information.

Visit our website: **www.3M.com/MedTech** for product and services information, news, events, new product highlights or to make a direct inquiry.

Medical Materials & Technologies
3M Center, Building 275-5W-05
St. Paul, MN 55144-1000 USA

Phone 1-800-228-3957
Web 3M.com/MedTech

Effective July 2018

C.2 Two sided adhesive film

Product Information Sheet
ARcare® 8939

Adhesives Research®

ARcare® 8939 is a white, polyester film coated on both sides with a medical pressure-sensitive adhesive. This double-faced tape is protected by a polyester release liner on both sides.

PRODUCT APPLICATIONS

The typical uses for this product are bonding, laminating and assembly of in-vitro diagnostic and related membrane-based immunoassay products where consistent product thickness is critical.

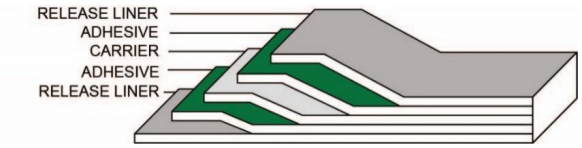

FEATURES AND BENEFITS

- Inert acrylic adhesive
- Easily die-cut
- Compatible with many assays
- Excellent conformability

Product Construction			
	Typical Values*		Description
Liner thickness	2.0 mil	50 µm	S/F polyester release liner
Adhesive thickness	1.0 mil	25 µm	AS-110, acrylic adhesive
Carrier	3.0 mil	76 µm	3 mil white polyester
Adhesive thickness	1.0 mil	25 µm	AS-110, acrylic adhesive
Liner thickness	2.0 mil	50 µm	S/F polyester release liner
Total thickness	5.0 mil	126 µm	(excluding liners)

*All stated values are nominal and should only be used as a guide for selection. They are not specifications.

SAFETY DATA

AS-110 is a medical grade adhesive. The adhesive passed cytotoxicity and primary skin irritation tests conducted by an independent laboratory. Additional safety information is available upon request.

Product Information Sheet
ARcare® 8939

Adhesives Research®

Technical Properties			
Attribute*	Typical Values*		Test Method*
Peel adhesion on stainless steel	50 oz/inch	14 N/25mm	90 degrees, 12 ipm, 5 min. dwell
Recommended storage of unconverted product	70°F ± 20°F 50% ± 20% RH	21°C ± 11°C 50% ± 20% RH	
Shelf life of unconverted product	Not to exceed two years from date of manufacture		

*All stated values are nominal and should only be used as a guide for selection. They are not specifications.

Note: The information contained on this data sheet is based upon test results of limited quantities of this material and may be modified by Adhesives Research following additional production experience and evaluation. This data should not be used in preparing specifications. Products identified as developmental may be subject to modification by Adhesives Research, Inc.

APPLICATION AND STORAGE OF PRESSURE-SENSITIVE ADHESIVE TAPES

Pressure-sensitive adhesive tapes function as a mechanical product; however, the adhesive itself is a chemical composition that can be sensitive to environmental conditions. A purchaser of pressure-sensitive adhesive products should be aware of the shelf life of each product and not purchase more than it can use before the expiration date. Shipping and storage conditions affect shelf life. The optimum storage temperature is 70 °F (21 °C). Cool, dry storage is recommended.

For best results…

1) The surfaces you wish to bond should be clean and free of oil, moisture and dust. If the surface temperature is below 40°F, it may be difficult to achieve a proper bond.
2) Do not use a pressure-sensitive adhesive product where it will be exposed to temperatures lower or higher than those designated for each product. Heat can destroy the effectiveness of the bond and extreme cold can cause the adhesive to harden and not adhere properly.
3) When the tape is applied, use firm hand or lamination pressure to achieve contact between the adhesive and the surface to which it is applied. Hand rollers or nip rollers may be needed for certain products or applications.

Consult your AR sales representative if you need additional information.

THIS IS NOT AN OFFER

This Product Information sheet ("PI Sheet") is not an offer to sell by Adhesives Research ("AR") and does not contain any binding warranties or terms of sale. While this PI Sheet does contain technical information and general warranty information, this PI Sheet is non-binding and is for information purposes only. If you wish to purchase the product set forth on this PI Sheet ("Product"), or have any questions regarding the warranty or other terms related to this Product, contact AR customer service or a sales representative and they will provide you with AR's terms of sale for the Product in the form of a Sales Order Acknowledgment. AR shall not be bound by any terms or information set forth in this PI Sheet.

DISCLAIMER OF WARRANTIES

AR's warranty on product is limited to the warranty set forth in the Sales Order Acknowledgment. **NOTHING SET FORTH IN THIS PRODUCT INFORMATION SHEET SHALL CONSTITUTE A WARRANTY OF ANY KIND AND EXCEPT AS SET FORTH IN THE SALES ORDER ACKNOWLEDGMENT. UNLESS OTHERWISE STATED IN A SALES ORDER ACKNOWLEDGMENT, AR EXPRESSLY DISCLAIMS ALL WARRANTIES, INCLUDING THE WARRANTIES OF MERCHANTABILITY OR FITNESS FOR A PARTICULAR PURPOSE.** No provisions, statements, diagrams, drawings or pictures contained in any product literature, price list, catalogue, purchase order, product data sheet, order acknowledgment, invoice, delivery ticket, or any other communication by AR, including information on AR's website or statements made by AR's employees or agents, constitute express warranties. Results of tests and recommendations included in communications of AR do not constitute express warranties. MANY FACTORS MAY AFFECT THE USE AND PERFORMANCE OF AN AR PRODUCT IN A PARTICULAR APPLICATION, INCLUDING, AMONG OTHERS, THE PRODUCT SELECTED FOR USE, THE CONDITIONS IN WHICH THE PRODUCT IS USED, THE TIME AND ENVIRONMENTAL CONDITIONS IN WHICH THE PRODUCT IS EXPECTED TO PERFORM, THE MATERIALS TO BE USED WITH THE PRODUCT, THE SURFACE PREPARATION OF THOSE MATERIALS, AND THE APPLICATION METHOD FOR THE PRODUCT; THEREFORE, PURCHASER ACCEPTS RESPONSIBILITY FOR DETERMINING WHETHER AR'S PRODUCT IS FIT FOR A PARTICULAR PURPOSE AND SUITABLE FOR PURCHASER'S METHOD OF APPLICATION. AR retains the right to modify or change its products if in AR's judgment it is advisable.

AR limits the purchaser's remedies in the event of a breach of any warranty. The purchaser's exclusive remedy and AR's obligations for a breach of any warranty shall be as set forth in the Sales Order Acknowledgment.

(Revised 16 October 2020)

North America – Headquarters
Adhesives Research, Inc.
400 Seaks Run Road
Glen Rock, PA 17327
Phone: +1 (717) 235-7979
Toll-free: +1 (800) 445-6240
Fax: +1 (717) 235-8320

Europe
Adhesives Research Ireland, Ltd.
Raheen Business Park
Raheen, Limerick
V94 VH22 Ireland
Phone: +353 61 300 300
Fax: +353 61 300 700

China
Adhesives Research China Co., Ltd.
Room 2710-2711, Building B
Far Glory International Square
No. 317 Xianxia Road
Shanghai, China 200051
Phone: +86 (21) 6150 4358
Fax: +86 21 6278 5576

Singapore
Adhesives Research PTE Ltd.
60 Paya Lebar Road
#04-04 Paya Lebar Square
Singapore 409051
Phone: +65 6774 9580
Fax: +65 6777 7261

C.3 One sided adhesive film

Product Information Sheet
ARcare® 8259

Adhesives Research®

ARcare® 8259 is a white, rigid plastic film coated on one side with a medical grade pressure-sensitive adhesive. The adhesive is protected by a clear polyester release liner.

PRODUCT APPLICATIONS

The typical uses for this product are bonding, laminating and assembly of in-vitro diagnostic and related membrane-based immunoassay products.

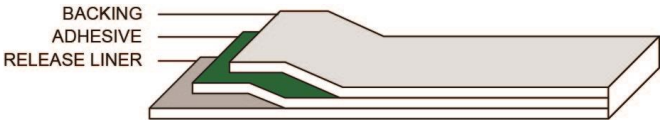

FEATURES AND BENEFITS

- Non-migratory, inert acrylic adhesive
- Easily die cut
- Tolerant to Gamma sterilization
- Allows lateral flow in membrane based devices
- Increased visibility
- Compatible with many assays

Product Construction			
	Typical Values*		Description
Backing thickness	5.0 mil	127 µm	White polyester film
Adhesive thickness	1.2 mil	30 µm	AS-110, acrylic adhesive
Liner thickness	2.0 mil	50 µm	Siliconized polyester release film
Total thickness	6.2 mil	157 µm	Excluding liners

*All stated values are nominal and should only be used as a guide for selection. They are not specifications.

SAFETY DATA

AS-110 is a medical grade adhesive. The adhesive passed cytotoxicity and primary skin irritation tests conducted by an independent laboratory. Additional safety information is available upon request.

Product Information Sheet
ARcare® 8259

Adhesives Research®

Technical Properties			
Attribute*	Typical Values*		Test Method*
Peel adhesion on stainless steel	100 oz/inch	28 N/25mm	180 degrees, 12 ipm, 5 min. dwell
Recommended storage of unconverted product	70°F ± 20°F 50% ± 20% RH	21°C ± 11°C 50% ± 20% RH	
Shelf life of unconverted product	Not to exceed two years from date of manufacture		

*All stated values are nominal and should only be used as a guide for selection. They are not specifications.

Note: The information contained on this data sheet is based upon test results of limited quantities of this material and may be modified by Adhesives Research following additional production experience and evaluation. This data should not be used in preparing specifications. Products identified as developmental may be subject to modification by Adhesives Research, Inc.

APPLICATION AND STORAGE OF PRESSURE-SENSITIVE ADHESIVE TAPES

Pressure-sensitive adhesive tapes function as a mechanical product; however, the adhesive itself is a chemical composition that can be sensitive to environmental conditions. A purchaser of pressure-sensitive adhesive products should be aware of the shelf life of each product and not purchase more than it can use before the expiration date. Shipping and storage conditions affect shelf life. The optimum storage temperature is 70 °F (21 °C). Cool, dry storage is recommended.

For best results…

1) The surfaces you wish to bond should be clean and free of oil, moisture and dust. If the surface temperature is below 40°F, it may be difficult to achieve a proper bond.
2) Do not use a pressure-sensitive adhesive product where it will be exposed to temperatures lower or higher than those designated for each product. Heat can destroy the effectiveness of the bond and extreme cold can cause the adhesive to harden and not adhere properly.
3) When the tape is applied, use firm hand or lamination pressure to achieve contact between the adhesive and the surface to which it is applied. Hand rollers or nip rollers may be needed for certain products or applications.

Consult your AR sales representative if you need additional information.

THIS IS NOT AN OFFER

This Product Information sheet ("PI Sheet") is not an offer to sell by Adhesives Research ("AR") and does not contain any binding warranties or terms of sale. While this PI Sheet does contain technical information and general warranty information, this PI Sheet is non-binding and is for information purposes only. If you wish to purchase the product set forth on this PI Sheet ("Product"), or have any questions regarding the warranty or other terms related to this Product, contact AR customer service or a sales representative and they will provide you with AR's terms of sale for the Product in the form of a Sales Order Acknowledgment. AR shall not be bound by any terms or information set forth in this PI Sheet.

DISCLAIMER OF WARRANTIES

AR's warranty on product is limited to the warranty set forth in the Sales Order Acknowledgment. **NOTHING SET FORTH IN THIS PRODUCT INFORMATION SHEET SHALL CONSTITUTE A WARRANTY OF ANY KIND AND EXCEPT AS SET FORTH IN THE SALES ORDER ACKNOWLEDGMENT. UNLESS OTHERWISE STATED IN A SALES ORDER ACKNOWLEDGMENT, AR EXPRESSLY DISCLAIMS ALL WARRANTIES, INCLUDING THE WARRANTIES OF MERCHANTABILITY OR FITNESS FOR A PARTICULAR PURPOSE.** No provisions, statements, diagrams, drawings or pictures contained in any product literature, price list, catalogue, purchase order, product data sheet, order acknowledgment, invoice, delivery ticket, or any other communication by AR, including information on AR's website or statements made by AR's employees or agents, constitute express warranties. Results of tests and recommendations included in communications of AR do not constitute express warranties. MANY FACTORS MAY AFFECT THE USE AND PERFORMANCE OF AN AR PRODUCT IN A PARTICULAR APPLICATION, INCLUDING, AMONG OTHERS, THE PRODUCT SELECTED FOR USE, THE CONDITIONS IN WHICH THE PRODUCT IS USED, THE TIME AND ENVIRONMENTAL CONDITIONS IN WHICH THE PRODUCT IS EXPECTED TO PERFORM, THE MATERIALS TO BE USED WITH THE PRODUCT, THE SURFACE PREPARATION OF THOSE MATERIALS, AND THE APPLICATION METHOD FOR THE PRODUCT; THEREFORE, PURCHASER ACCEPTS RESPONSIBILITY FOR DETERMINING WHETHER AR'S PRODUCT IS FIT FOR A PARTICULAR PURPOSE AND SUITABLE FOR PURCHASER'S METHOD OF APPLICATION. AR retains the right to modify or change its products if in AR's judgment it is advisable.

AR limits the purchaser's remedies in the event of a breach of any warranty. The purchaser's exclusive remedy and AR's obligations for a breach of any warranty shall be as set forth in the Sales Order Acknowledgment.

(Revised 16 May 2020)

North America – Headquarters
Adhesives Research, Inc.
400 Seaks Run Road
Glen Rock, PA 17327
Phone: +1 (717) 235-7979
Toll-free: +1 (800) 445-6240
Fax: +1 (717) 235-8320

Europe
Adhesives Research Ireland, Ltd.
Raheen Business Park
Raheen, Limerick
V94 VH22 Ireland
Phone: +353 61 300 300
Fax: +353 61 300 700

China
Adhesives Research China Co., Ltd.
Room 2710-2711, Building B
Far Glory International Square
No. 317 Xianxia Road
Shanghai, China 200051
Phone: +86 (21) 6150 4358
Fax: +86 21 6278 5576

Singapore
Adhesives Research PTE Ltd.
60 Paya Lebar Road
#04-04 Paya Lebar Square
Singapore 409051
Phone: +65 6774 9580
Fax: +65 6777 7261

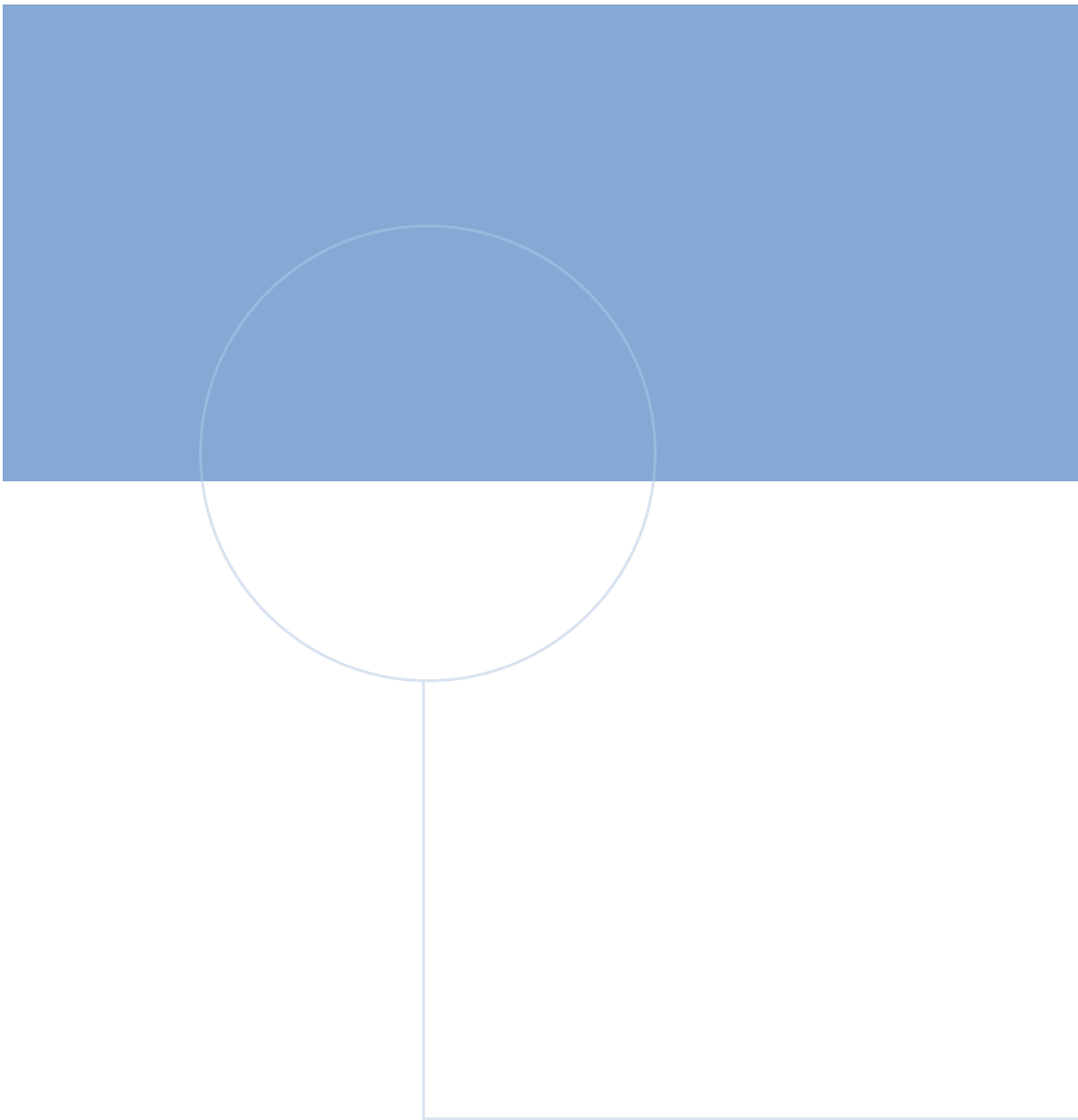

NTNU

Norwegian University of
Science and Technology